Novel Organic Heterostructures Enabled by Emulsion-Based, Resonant Infrared, Matrix-Assisted Pulsed Laser Evaporation (RIR-MAPLE)

by

Ryan Daniel McCormick

Department of Electrical and Computer Engineering
Duke University

Date: _____

Approved:

_____
Adrienne Stiff-Roberts, Supervisor

_____
April Brown

_____
Christopher Dwyer

_____
Jeffrey Glass

_____
Jie Liu

Dissertation submitted in partial fulfillment of
the requirements for the degree of Doctor of Philosophy
in the Department of Electrical and Computer Engineering
in the Graduate School of Duke University
2014

Abstract

Novel Organic Heterostructures Enabled by Emulsion-Based, Resonant Infrared, Matrix-Assisted Pulsed Laser Evaporation (RIR-MAPLE)

by

Ryan Daniel McCormick

Department of Electrical and Computer Engineering
Duke University

Date: _____

Approved:

_____
Adrienne Stiff-Roberts, Supervisor

_____
April Brown

_____
Christopher Dwyer

_____
Jeffrey Glass

_____
Jie Liu

An abstract of a dissertation submitted in partial fulfillment of
the requirements for the degree of Doctor of Philosophy
in the Department of Electrical and Computer Engineering
in the Graduate School of Duke University
2014

Abstract

An explosion in the growth of organic materials used for optoelectronic devices is linked to the promise that they have demonstrated in several ways: workable carrier mobilities, ease of processing, design flexibility to tailor their optical and electrical characteristics, structural flexibility, and fabrication scalability. However, challenges remain before they are ready for prime time. Deposition of these materials into ordered thin films requires that they be cast from solutions of organic solvents. Drawbacks of solution-casting include the difficulty of producing layered films without utilizing orthogonal solvents (or even with orthogonal solvents), the difficulty in controlling domain sizes in films of mixed materials, and the lack of parameter options used to control the final properties of thin films. Emulsion-based, resonant infrared, matrix-assisted pulsed laser evaporation (RIR-MAPLE) is a thin film deposition technique that is demonstrated to provide solutions to these problems.

This work presents fundamental research into the RIR-MAPLE process. An investigation of the molecular weight of deposited materials demonstrates that emulsion-based RIR-MAPLE is capable of depositing polymers with their native molecular weights intact, unlike other laser deposition techniques. The ability to deposit multilayer films with clearly defined interfaces is also demonstrated by cross-sectional transmission electron microscopy imaging of a layered polymer/quantum dot nanocomposite film. In addition, trade-offs related to the presence of surfactant in the target, required to stabilize the emulsion, are articulated and investigated by

x-ray diffraction, electrical, optical, and surface characterization techniques. These studies show that, generally speaking, the structural, optical and electrical properties are not significantly affected by the affected by the presence of surfactant, provided that the concentration within the target is sufficiently low. Importantly, the in-plane mobility of RIR-MAPLE devices, determined by organic field effect transistor (OFET) characterization, rivals that of spin-cast devices produced under similar conditions.

This work also presents results of emulsion-based RIR-MAPLE deposition applied to optical coatings (gradient-refractive index antireflection coating based on porous, multilayer films) and optoelectronic devices (organic photovoltaics based on the polymer, P3HT, and small molecule, $PC_{61}BM$, bulk heterojunction system). The optical coating demonstrates that RIR-MAPLE is capable of producing nanoscale domain sizes in mixed polymer blends that allow a film to function as an effective medium relevant to devices in the visible spectrum. Moreover, bulk heterojunction organic photovoltaic (OPV) devices that require nanoscale domains to function effectively are achieved by co-deposition of P3HT and $PC_{61}BM$, achieving a power conversion efficiency of 1.0%, which is a record for MAPLE-deposited devices.

Results of these studies illuminate unique capabilities of the RIR-MAPLE process. Multilayer films are readily fabricated to create true bilayer OPV structures. Additionally, true gradient thin films are created by varying the ratio of two materials, including two-polymer films and a film consisting of a polymer and a small molecule, over the course of a single deposition.

This dissertation is dedicated to my young son, Oscar, and to my wife, Julie, who both indulged me while I returned after 7 years in the workforce to graduate school for 5 years to get a PhD. I thank you for your support and your patience. I love you. It is also dedicated to all of the people who have encouraged me throughout my life to explore and maintain a healthy curiosity, including my teachers, relatives, friends, and colleagues. I hope that I am able to pass such a gift on to my son the way it was given to me.

Contents

Abstract **iv**

List of Tables **x**

List of Figures **xii**

Acknowledgments **xx**

1 Resonant Infrared, Matrix-Assisted Pulsed Laser Evaporation (RIR-MAPLE) **1**

1.1 Organic Thin Film Deposition by MAPLE 3

1.2 Emulsion-Based Resonant Infrared, Matrix-Assisted Pulsed Laser Evaporation 4

2 Enabling Capabilities Demonstrated for Emulsion-Based, RIR-MAPLE Deposition **8**

2.1 Polymer Deposition without Reduction of Molecular Weight 8

2.1.1 RIR-MAPLE Deposition 10

2.1.2 Gel Permeation Chromatography Measurements 10

2.1.3 ^{1}H NMR Spectroscopy and FTIR Spectroscopy 17

2.2 Polymer-Based Multilayer Heterostructures 22

2.2.1 RIR-MAPLE Deposition 23

2.2.2 Cross-Sectional Transmission Electron Microscopy 27

2.3 Conclusions 29

3 Trade-offs of Emulsion-Based, RIR-MAPLE: Surfactant Effects 31

3.1 Presence of Emulsion Target Surfactant in P3HT Thin Films 32

3.2 Effect of Target Surfactant on P3HT Thin Film Structure 36

3.3 Effect of Target Surfactant on P3HT Thin Film Mobility 44

3.4 Effect of Target Surfactant on P3HT Thin Film Conjugation Length and Crystalline Aggregates 50

3.5 Effect of Target Surfactant on P3HT Thin Film Surface Morphology . 54

3.6 Conclusions 58

4 Gradient Refractive Index Anti-Reflection Optical Coatings Deposited by RIR-MAPLE 59

4.1 RIR-MAPLE Thin Film Growth and Characterization 61

4.2 Nanoscale Phase Domains in Homopolymer Blends 63

4.3 Optical Effective Media Using Homopolymer Blends 70

4.4 Gradient Refractive Index Anti-Reflection Coating 79

4.5 Conclusions 83

5 Organic Photovoltaics by Emulsion-Based RIR-MAPLE 87

5.1 RIR-MAPLE Growth of OPV Active Regions and Device Characterization 89

5.2 Bulk Heterojunction P3HT:PCBM Ratio Study 91

5.3 Optimizing the P3HT:PCBM Ratio in the Bulk Heterojunction Structure 99

5.4 Device Structure Study 102

5.5 Conclusions 108

6 Future Work 110

A Processing and Characterization Conditions 114

B Hansen Solubility Parameters 127

C RIR-MAPLE Parameter Study of P3HT 131

Bibliography **134**

Biography **144**

List of Tables

2.1 Molecular weight of polymers deposited by laser ablation 11

2.2 Polydispersity Index of polymers deposited by laser ablation 16

3.1 GIWAXS peak q and d values of RIR-MAPLE P3HT films. The values in this table summarize the data in Figure 3.6 and Figure 3.7. 43

3.2 IP to OOP (010)/(100) ratio, indicating the relative number of π-stacked, ordered polymer chains oriented IP versus the relative OOP quantity. 44

3.3 Spano absorbance parameters extracted from nonlinear, least-squares fit to UV-visible absorbance data of P3HT thin films deposited by RIR-MAPLE. 52

3.4 Deposition parameters for thin RIR-MAPLE films of P3HT. Sample number is indicated by #1 or #2. 54

4.1 The RMS surface roughness, R_q, normalized by the film thickness for the three PS:PMMA polymer ratios both before and after a 3 minute glacial acetic acid wash. In general, the roughness increases after the acid wash due to the formation of pores left by the PMMA component removal. 65

4.2 Dispersive RI Sellmeier coefficients of porous PS films. The C_i values represent UV absorption peaks of bulk PS. The B_i values are determined by a least squares fit to the measured RI data (400-800 nm). . 72

5.1 OPV metrics for the P3HT:PCBM BHJ ratio study. 92

5.2 Peak ratios measured from 1D GIWAXS data in Figure 5.7. The 1:3 and 1:2 P3HT:PCBM devices had no (010) peak from which to calculate a ratio. 96

5.3 Spano absorbance analysis fit parameters for RIR-MAPLE BHJ P3HT:PCBM films. 98

5.4 OPV metrics for the P3HT:PCBM BHJ ratio study near 1:1. 99

5.5 Peak ratios measured from 1D GIWAXS data in Figure 5.12. 102

5.6 Spano absorbance analysis of the P3HT:PCBM ratios near 1:1. 102

5.7 OPV metrics for different device structures. 104

5.8 Peak ratios measured from 1D GIWAXS data in Figure 5.17. 107

5.9 Spano absorbance analysis of the different OPV structures. 108

B.1 Hansen solubility parameters and radii for the polymers and small molecules used in this work. 128

B.2 Hansen solubility parameters for solvents used in this work. 128

C.1 P3HT films deposited by varying 8 RIR-MAPLE parameters at random within predefined parameter ranges. Samples 1-8. 132

C.2 P3HT films deposited by varying 8 RIR-MAPLE parameters at random within predefined parameter ranges. Samples 9-15. 133

List of Figures

1.1 Schematic of the RIR-MAPLE process. 5

2.1 Molecular weight of polymers before and after deposition by the stated deposition technique. All RIR-MAPLE data were generated by the author. 12

2.2 GPC measurements of the native MEH-PPV polymer and the resulting distributions after RIR-MAPLE deposition. The log-scale plot emphasizes the reduction in the largest molecular weights after deposition. The inset shows the peak values on a linear scale. These distributions are representative of repeated GPC measurements. . . . 15

2.3 Proton NMR spectra of PMMA of molecular weight (a) 10 kDa, and (b) 100 kDa. The solvent peak at $\delta = 7.26$ ppm is denoted by *. The water peak at $\delta = 1.56$ ppm is denoted by #. 17

2.4 Proton NMR spectra of native P3HT polymer and RIR-MAPLE deposited samples. The solvent peak at $\delta = 7.26$ ppm is denoted by *. The water peak at $\delta = 1.56$ ppm is denoted by #. 18

2.5 FTIR spectra of P3HT before and after RIR-MAPLE deposition. . . 19

2.6 Proton NMR spectra of native MEH-PPV and of MEH-PPV after RIR-MAPLE deposition. The solvent peak is denoted by *. 20

2.7 FTIR spectra of MEH-PPV. There is no difference between the native polymer and the RIR-MAPLE deposited polymer. 21

2.8 TEM images of RIR-MAPLE-deposited nanocomposite taken in the x-y plane as defined above. (a,b) Simultaneous MAPLE deposition. (c,d) Sequential MAPLE deposition. 23

2.9 Schematic of XTEM sample showing average as-grown layer thicknesses. 24

2.10 XTEM sample deposited by RIR-MAPLE. The glass substrate is at the top right. The uniform ITO bar is 168 nm thick. The white areas are tears between the layers due to the FIB sample preparation. Three measurements of the total RIR-MAPLE-deposited thickness are taken across the sample at locations of minimal tearing. The Pt thickness is also indicated. See the text for analysis. 25

2.11 Zoom of second XTEM sample. Black bar at upper right is the ITO layer atop the glass substrate. The sequential layer consists of the four light and dark striations of 137 nm thickness. There is a polymer buffer layer of 98 nm thickness, then the 129-nm-thick simultaneous polymer layer. A slow-growth polymer layer of 129-nm thickness is followed by a fast-growth 211-nm-thick layer. The bottom left shows the metallic cap of Au/Pd and Pt. 26

3.1 X-ray diffraction plots of RIR-MAPLE deposited P3HT films with 0.30 wt% and 0.01 wt% added sodium dodecyl sulfate (SDS) surfactant. For comparison, films without P3HT were deposited using the identical preparation and deposition parameters. It is clear that the peaks are due to the surfactant alone. 33

3.2 XRD results of P3HT films grown by RIR-MAPLE while varying the quantity of added SDS surfactant. In the lower 2θ range (left), the 0.1 wt% SDS film exhibited the same surfactant peaks identified in Figure 3.1. Additional peaks appeared in the higher 2θ range (right) of the 0.1 wt% SDS film and were reproduced in the 0.01 wt% SDS film. The 0.001 wt% SDS film showed no evidence of the surfactant. . 34

3.3 2D GIWAXS measurements of a representative RIR-MAPLE-deposited P3HT thin film (top) compared with drop-cast (bottom, left) and spin-cast (bottom, right) P3HT thin films. RIR-MAPLE parameters are: 7 cm TS distance; with SDS; annealed at 140 °C for 30 minutes. . . . 38

3.4 Comparison of one representative RIR-MAPLE sample with solution-cast films. (a) IP and (b) OOP GIWAXS measurements of P3HT films integrated from the IP or vertical angle $\pm 20^{\circ}$ and normalized to the (010) peak. 39

3.5 2D GIWAXS images of P3HT films fabricated by RIR-MAPLE at 7 cm TS distance. Effects of SDS surfactant and thermal annealing at 140 °C for 30 minutes are shown. 40

3.6 IP GIWAXS measurements of P3HT films integrated from IP angle +20° and normalized to the (010) peak. a) The effects of target-substrate distance and annealing are shown. b) The effects of surfactant added to the RIR-MAPLE emulsion and of annealing are shown. 41

3.7 OOP GIWAXS measurements of P3HT films integrated from the vertical angle ±20° and normalized to the (010) peak. a) The effects of target-substrate distance and annealing are shown. b) The effects of surfactant added to the RIR-MAPLE emulsion and of annealing are shown. 42

3.8 OFET device (l) schematic and (r) measurement of RIR-MAPLE-deposited P3HT films. The photo shows actual devices where each row represents a different channel length (top to bottom): 25 μm, 50 μm, 75 μm, and 100 μm. Each set of Au contacts represents the source and drain. The single contact in the lower part of the image is the gate contact. 45

3.9 Output and transfer curves of the highest mobility RIR-MAPLE OFET as deposited: 7 cm TS distance; with SDS. 46

3.10 Output and transfer curves of the highest mobility RIR-MAPLE OFET after annealing at 140 C for 30 minutes in N^2 glove box: 7 cm TS distance; with SDS. 47

3.11 In-plane (IP) mobility comparison of 5 single RIR-MAPLE-deposited P3HT OFET devices with 4 single spin-cast devices exposed to similar environmental conditions. 48

3.12 Summary of the hole mobilities calculated from RIR-MAPLE deposited OFET devices in comparison with spin-cast devices. The vertical bars indicated one standard deviation above and below the mean value after averaging the mobility values across all viable devices on a 16-device substrate. 49

3.13 Spano absorbance analysis of RIR-MAPLE-deposited P3HT thin film with deposition parameters: 7 cm TS distance, with SDS, and device 1. 51

3.14 AFM measurements of thin P3HT films deposited at fast deposition rate (4 cm TS distance) showing the effect of the absence or presence of SDS surfactant. The top row shows 2 different constant-parameter depositions without SDS. The bottom row shows 2 different constant-parameter depositions with SDS. 56

3.15 AFM measurements of thin P3HT films deposited at slow deposition rate (7 cm TS distance) showing the effect of the absence or presence of SDS surfactant. The top row shows 2 different constant-parameter depositions without SDS. The bottom row shows 2 different constant-parameter depositions with SDS. 57

4.1 TEM image of RIR-MAPLE grown PS:PMMA 1:1 film that has been exposed to RuO_4 vapor for 90 minutes. The PS component absorbs the vapor and is stained; the PMMA is unaffected. PS domains are less than 100 nm. 64

4.2 AFM phase images of as-grown PS:PMMA film after 3 minute acetic acid wash. Polymer ratios are (left) 1:3, (middle) 1:1, and (right) 3:1 PS:PMMA. 66

4.3 AFM phase images of PS:PMMA films after annealing at 100 °C and then a 3 minute acetic acid wash. Polymer ratios are (left) 1:3, (middle) 1:1, and (right) 3:1 PS:PMMA. 66

4.4 AFM phase images of PS:PMMA films after annealing at 120 °C and then a 3 minute acetic acid wash. Polymer ratios are (left) 1:3, (middle) 1:1, and (right) 3:1 PS:PMMA. 66

4.5 AFM phase images of PS:PMMA films after annealing at 140 °C and then a 3 minute acetic acid wash. Polymer ratios are (left) 1:3, (middle) 1:1, and (right) 3:1 PS:PMMA. 67

4.6 SEM images of as-deposited blended PS:PMMA 1:1 v/v films deposited by RIR-MAPLE show no evidence of porosity prior to removal of the PMMA component via acetic acid. 69

4.7 SEM images of porous polystyrene films: (a) 25% porosity, (b) 50% porosity, (c) 75% porosity. 69

4.8 Refractive index spectra of porous polystyrene films as measured by spectroscopic ellipsometry. Experimental data points are shown relative to bulk polystyrene (black line); Sellmeier fits to the experimental RI data are represented as solid lines. Fitting coefficients are given in the supplemental materials. 71

4.9 Calculated reflectivity spectra of porous polystyrene thin films (50% porosity by volume). (a) Film thickness effects for three different incident wavelengths (400 nm, 600 nm, 800 nm). (b) Spectral effects for three film thicknesses (50 nm, 100 nm, and 150 nm). 74

4.10 (a) Comparison of measured and fit (Methods A and B) reflectivity spectra for 50% porous polystyrene film. The red curve represents Method A, which results in an RI spectrum with anomalous dispersion that is non-physical (see Figure 4b). The green curve represents Method B, which is the true physical representation of the film. (b) Non-physical refractive index spectra that resulting from fitting the measured reflectivity using Method A. The corresponding porosities trend in the wrong direction with respect to the RI value. Also, the RI shape demonstrates anomalous dispersion, yet normal dispersion is observed in the measured ellipsometry data. 75

4.11 Comparison of measured and fit (Methods A and B) reflectivity spectra for 25% (left) and 75% (right) porous polystyrene films. Method A is non-physical. Method B is the true physical representation of the film. 76

4.12 Measured reflectivity spectra (using integrating sphere) of the RIR-MAPLE-deposited porous polystyrene films (i.e. after PMMA removal). Markers depict experimental data relative to the Si substrate (black line); solid lines represent the Fresnel transfer matrix model fit to the measured data using Method B. 77

4.13 (left) Schematic of the gradient RIR-MAPLE film; (right) Linear distribution of the refractive index that results from grading the PS:PMMA ratio. 79

4.14 Fresnel theory calculations of reflectance of a 1 μm thick film with a linearly graded refractive index between a polycarbonate substrate (n = 1.58) and air (n = 1.00). Calculations are included for normal incidence (0°) and 60° relative to normal for three different thicknesses of constant RI slices. 80

4.15 SEM images of the surface of the two GRIN films fabricated by RIR-MAPLE. The top row shows no porosity after deposition. The bottom row shows the porous PS structure at the film surface after porogen removal. The first column represents GRIN sample 1 with 10-nm slices. The second column represents GRIN sample 2 with 20-nm slices. 82

4.16 Optical R/T/A analysis using an integrating sphere of the bare polycarbonate (PC) substrate and the two RIR-MAPLE fabricated GRIN films. GRIN film 1 contained 100 slices of 10 nm thickness where each slice contained a constant RI ratio. GRIN film 2 contained 50 slices of 20 nm thickness at constant RI ratio in each slice. Reflectance is improved by both GRIN film design. Only design 1 improved transmission through the substrate. Both designs increased the absorbance and scattering across the spectrum. GRIN design 1 is shown in the bottom right image in a black holder to minimize contact with the film. 86

5.1 Energy band diagram of P3HT:PCBM photovoltaic device showing LUMO and HOMO values in eV relative to the vacuum level. The P3HT absorbs photons that create excitons, which are then split at the P3HT/PCBM interface into free carriers. Electrons are collected at the Al cathode; and, holes are collected at the ITO anode. 88

5.2 Measured UV-Vis absorbance of PCBM and P3HT, normalized to the peak value, plotted against the AM 1.5G solar spectrum [1]. 90

5.3 Average photocurrent density versus applied bias for each of the five RIR-MAPLE target volume ratios: 1:3, 1:2, 1:1, 2:1, and 3:1. Each curve is the average of six different 9 mm^2 devices. 92

5.4 JV response of a bilayer device to an irradiance of 0.75-2.25 suns in 0.25-sun increments, demonstrating the proportionality of the current to irradiance. 93

5.5 (a) Measured external quantum efficiency and (b) UV-visible absorbance for five RIR-MAPLE target volume ratios of P3HT:PCBM OPVs 1:3, 1:2, 1:1, 2:1, 3:1. 94

5.6 2D GIWAXS images of films made of the following RIR-MAPLE P3HT:PCBM target ratios: (a) 1:3; (b) 1:2; (c) 1:1; (d) 2:1; (e) 3:1. For comparison, a PCBM-only film deposited by RIR-MAPLE is shown in (f). 95

5.7 1D GIWAXS data from Figure 5.6 integrated along the (a) IP and (b) OOP directions and normalized to the PCBM peak near q = 1.30 $Å^{-1}$ to accentuate the P3HT peaks. 95

5.8 (a) OPV and PCBM-only absorbance data are shown for a 1:1 P3HT:PCBM RIR-MAPLE target ratio. The data are locally smoothed and then the PCBM-only data are scaled to the OPV PCBM peak to be subtracted. (b) The resulting P3HT contribution is shown with the Spano theory overlaid, which determines the crystalline aggregates in the P3HT bulk. The remainder of the spectrum accounts for disordered chains in the amorphous regions. 98

5.9 Average JV characteristics of the 2nd ratio study to determine the true optimum RIR-MAPLE target ratio of P3HT:PCBM in a BJH OPV device. Each curve is the average of six different 9 mm^2 devices. The work was motivated by knowledge of the optimum ratio of P3HT:PCBM in spin-cast films, which is slightly larger than unity. . 99

5.10 (a) EQE and (b) absorbance for the three ratios near 1:1 P3HT:PCBM RIR-MAPLE target volume ratio: 0.7:1, 1:1, 1:0.7. 100

5.11 2D GIWAXS images of the following RIR-MAPLE target ratios of P3HT:PCBM: (a) 0.7:1; (b) 1:1; (c) 1:0.7. 101

5.12 1D GIWAXS data integrated along the a) IP and b) OOP directions from the data in Figure 5.11. The data have been normalized to the main PCBM peak near q = 1.30 $Å^{-1}$ to accentuate the P3HT peak differences. 101

5.13 Schematic of the three OPV structures fabricated by RIR-MAPLE: a bulk heterojunction, a bilayer, and a gradient layered film. 104

5.14 Best performance of each device structure deposited by RIR-MAPLE: bulk heterojunction at the optimum target volume ratio of 0.7:1 P3HT:PCBM, a bilayer of equal thickness P3HT and PCBM layers, and a gradient layered film. Each curve is an average of 6 different 9 mm^2 devices. . 105

5.15 (a) EQE and (b) absorbance of the highest performing device of each structure type. 106

5.16 2D GIWAXS images of the highest PCE device of each structure type: (a) BHJ (0.7:1); (b) Bilayer; (c) Gradient. 106

5.17 1D GIWAXS data integrated along the a) IP and b) OOP directions for the highest PCE devices of each type in the study. 107

A.1 SEM images of the FIB milling process (l to r): (a) Sample surface coated with AuPd and Pt bar. (b) Top view of sample after coarse milling. (c) An oblique view of milled sample shows the vertical slice; the polymer (dark) and glass (light) substrate layers are distinguishable. (d) Total sample thickness measures 9.31 μm. 116

A.2 Raw image of a GIWAXS 2D scattering plot on the left, which is transformed to a plot of azimuthal angle vs. q (momentum transfer) via SAXSgui software (SAXSLab). The OOP direction is located at 180°; the IP direction is located at 90° and 270°. The horizontal bars in the raw image represent boundaries between the active regions of the x-ray detector. 119

A.3 (left) OOP area of integration; (center) 1st IP area of integration; (right) 2nd IP area of integration. The two IP integrations are averaged where they overlap, while the data are discarded in the dropout regions. 119

A.4 Patterned ITO glass substrate seated in the cathode deposition mask. The six ITO strips are clearly visible against the square active region deposited by RIR-MAPLE. The two cathode strips can be seen as the vertical openings beneath the substrate that each overlaps three ITO anodes. There is another ITO strip that runs the length of the substrate at the bottom and acts to connect the deposited cathodes together. 120

B.1 Solubility determination of a polymer in a mixture of two solvents. A linear combination of the Hansen solubility parameters of the two solvents plotted versus the volume fraction of solvent 2 in a mixture with solvent 1 are used to determine the RED values (values at/below 1 indicate likely miscibility). The symbols indicate the values used for the majority of the films in this work. 130

Acknowledgments

PhD work is never the work of one person alone. There are many that had a hand in producing the volume before you. First, I would like to thank my advisor, Dr. Adrienne Stiff-Roberts for her support and flexibility, which allowed me to work on projects of mutual interest. She wisely provides a lot of rope with which you can either build something great or hang yourself with, and yet always finds the time to help when needed. Luckily, I am the type that strives to build something great.

I am grateful to my colleagues at Duke who helped train me, collaborated on projects, ran samples, provided constructive criticism, and shared a few laughs and stories: Ryan Pate, Kevin Lantz, Yushin Park, Wangyao Ge, Ayo Atewologun, Yuankai Liu, and other folks who helped out in many ways. I would be remiss if I did not thank the folks in the Shared Materials Instrumentation Facility (SMIF) at Duke who assisted with the large amount of expensive equipment required to produce this work: Mark Walters, Kirk Bryson, Michelle Gignac, Jay Dalton, and Jimmy Thostenson.

Our collaborators at UT, Arlington, and at ORNL also deserve many thanks. Weidong Zhou and Arvinder Chadha provided solid support with the optical theory behind the GRIN-AR films in addition to fully characterizing the R/T/A values of numerous polystyrene films. Eric Cline and Xiaofeng Meng were instrumental in producing a workable GRIN-AR coating with their materials fabrication and sample processing skills.

The esteemed folks in the Nanomaterials Synthesis and Functional Assembly group in the Center for Nanophase Materials Sciences at Oak Ridge National Laboratory were extremely helpful and supportive of our laser-deposited organic photovoltaic devices, providing much expertise in fabrication and characterization techniques, as well as fruitful discussions of results: Kai Xiao, David Geohegan, Ming Shao, Ilia Ivanov, Chris Rouleau, and also Andrew Payzant for his help with setting up and learning the GIWAXS technique.

Finally, I would like to thank my committee for their feedback, support, and generous donation of time. Constructive criticism is often misguidedly feared as a sign of failure, but it is vital if one is to improve, and I thank them for not pulling punches, yet landing them gently. RM

1

Resonant Infrared, Matrix-Assisted Pulsed Laser Evaporation (RIR-MAPLE)

The quantity of targeted applications requiring organic thin films has grown rapidly in the past decade. The demand for controlled deposition of the wide array of new materials and structures currently being designed will continue to increase. The few deposition techniques that exist can generally be consolidated into two categories: thermal evaporation and solution casting. Small molecules have been deposited by both techniques, but polymers can only be solution-cast into thin films from an organic solvent solution using methods such as drop-casting [2], spin-casting [3], ink-jet printing [4], Langmuir-Blodgett processes [5], and electrospraying [6]. Moreover, the fabrication of heterostructures and blends is limited to thermal evaporation due to the limitations of solution-casting. Heterostructures created by solution-casting require orthogonal solvents for successive layers so as to avoid dissolution of the previously deposited layers. Additionally, interfaces between materials may degrade due to the practical requirements of changing processes between materials, for instance, creating a bilayer of a solution-cast polymer and a thermally-evaporated small molecule.

Blends of polymers via solution-casting are driven by the thermodynamics of the mixture and primarily result in films in which there is little control over the nanoscale domain size and overall morphology of the film. The level of control exerted over the evaporation of the solvent during film formation is one of the few options available to the designer. A potential solution to these problems is a promising technique, related to pulsed laser deposition, called Matrix-Assisted Pulsed Laser Evaporation (MAPLE) in which a polymer solution is flash-frozen under vacuum into a solid target, upon which laser energy evaporates the frozen solvent, and the polymer is deposited onto a substrate [7].

MAPLE has many attractive capabilities that may overcome the problems inherent in solution-casting. The availability of many control parameters allows for tuning of the film morphology. Multilayer heterostructures, regardless of the compatibility of the solubility of the materials, are straightforward to achieve. Blended films with control over material composition and nanoscale morphology are readily fabricated. As a practical matter, the MAPLE technique can provide deposition of multiple materials, either simultaneously or sequentially, without having to alternate processes. Moreover, MAPLE can still deposit a wide range of materials including polymers, small molecules, and inorganic quantum dots, among others. The technique is versatile and has been used for applications including gas sensors [8], biosensors [7], micron-scale patterning of biomaterials and polymers [9], nanoparticle synthesis [10], and optoelectronics. The Stiff-Roberts group pioneered a variant of the MAPLE technique called emulsion-based, resonant infrared MAPLE (RIR-MAPLE), which was first demonstrated in 2008 and will be the technique used throughout this work [11]. This chapter reviews the history of the MAPLE technique, describes the MAPLE process, and reviews the past development of the emulsion-based, RIR-MAPLE deposition technique.

1.1 Organic Thin Film Deposition by MAPLE

The MAPLE technique was first demonstrated in 1999 at the Naval Research Laboratory as a gentler alternative to pulsed laser deposition (PLD) techniques, which tended to degrade the organic materials during deposition [12]. Studies followed in 2002 in which the effects of MAPLE on the deposited materials appeared to be degrading the native polymer [13, 14]. It was found that photochemical reactions between the laser pulse and the solvent affected the deposited polymer. For example, the UV laser light (ArF laser, $\lambda = 193$ nm) photodissociated the solvent chloroform ($CHCl_3$) to produce Cl^- free radicals that degraded the polymer during deposition [13]. At the same wavelength, water, used as a solvent, showed no indication of photodissociation, resulting in better films. The polymers of interest also tended to absorb in the visible to ultraviolet region, making direct photodegradation a concern.

Therefore, a different strategy was reported by Bubb, et al. [15], and Toftmann, et al., in 2004 [16], which utilized infrared lasers to ablate the solvent by targeting the vibrational bond stretches, such as the hydroxyl O-H bond, and thereby separate the absorption spectrum of the solvent from that of the polymer. Thus, a distinction was made between different excitation wavelengths used in MAPLE: ultraviolet excitation, usually $\lambda = 193$ nm, as above, or $\lambda = 248$ nm from a KrF excimer laser, deemed ultraviolet MAPLE (UV-MAPLE); and, infrared excitation that is resonant with particular chemical bond stretches within the liquid solvent, which has been dubbed resonant-infrared MAPLE (RIR-MAPLE) [17–19].

Emulsion-based RIR-MAPLE further decouples the absorption of the laser energy from the guest material and its solvent by targeting resonant absorption in water in order to promote gentle deposition. Emulsion-based RIR-MAPLE is a promising deposition technology for the fabrication of polymer-based optoelectronic devices for two primary reasons: i) the ability to control and tune many aspects of nanoscale

morphology; and, ii) the ability to deposit multilayered films or heterostructures regardless of the constituent material solubility [11, 20–23]. These two important features motivate the remainder of this work.

1.2 Emulsion-Based Resonant Infrared, Matrix-Assisted Pulsed Laser Evaporation

The unique emulsion-based RIR-MAPLE approach, developed by the Stiff-Roberts group, uses a 2-Hz, table-top, pulsed Er:YAG laser (90 μs pulse length) with a fixed emission wavelength at 2.94 μm that is resonant with hydroxyl (O-H) bonds [11, 20–24]. By creating target emulsions of the desired guest material and corresponding solvent with water, emulsion-based RIR-MAPLE deposition of a variety of polymers, nanoparticles, and hybrid organic/inorganic nanocomposites have been demonstrated. The novelty of the emulsion-based RIR-MAPLE approach, compared to alternative MAPLE implementations [7, 12–16, 25, 26], is that the ideal growth regime, i.e., strong laser absorption by the host matrix and little to no laser absorption by the guest material, can be achieved for almost any polymer, even though most polymers of interest and many compatible solvents do not resonantly absorb the Er:YAG laser energy at 2.94 μm. This challenge is overcome due to the target emulsion in which a secondary solvent and deionized water, both rich in O-H bonds that are resonant with the Er:YAG laser energy, are added to the polymer solution.

In the emulsion-based MAPLE deposition process (Figure 1.1), the prepared polymer solution or emulsion, called the matrix, is flash frozen in a target cup that has been cooled to -196 °C (77 K) by liquid nitrogen. The purpose of the flash freezing process is to solidify the matrix before it is able to separate. The target and substrate are located in a vacuum chamber for two primary reasons. First, environmental conditions are better controlled. Second, in order to avoid liquid contamination of the deposited film, a lower environmental pressure allows the target material to

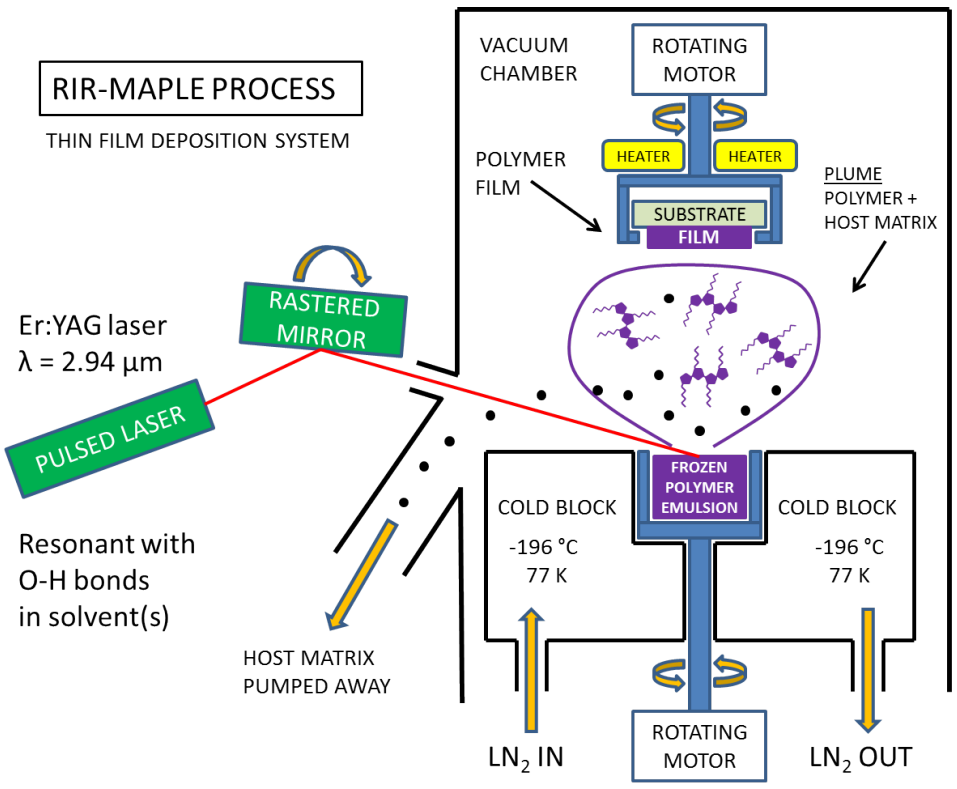

FIGURE 1.1: Schematic of the RIR-MAPLE process.

sublimate so that the vaporous solvent can be pumped away by the vacuum system. In the vacuum chamber, the substrate is located facing the target and rotates at a constant rate (usually 10-15 RPM) during a deposition. The pulsed laser rasters radially across the target, which rotates at a constant rate (usually 3-4 RPM), in a pattern that ensures that the target is ablated evenly. The vaporous host matrix (solvents and water) is pumped away by the vacuum system, leaving the polymer to be uniformly deposited onto the substrate.

The RIR-MAPLE target composition is crucial to control of polymer thin film characteristics. Polymers deposited by solution casting consist of the polymer dissolved in a solvent. Because the MAPLE target is flash frozen and exposed to low pressures, the target must be prepared so as to minimize spontaneous sublimation of the solvent needed to ablate the polymer. Moreover, the laser energy targets the hy-

droxyl bond stretch, so the target must contain a large proportion of hydroxyl-dense solvents to maximize the vaporization of the target material. Conversely, films that have a large amount of liquid-phase solvent deposition due to poor solvent vaporization tend to have improved performance when the film has been annealed at elevated temperature because the remaining trapped solvent escapes from the film, effectively reorienting the polymer chains and relaxing conformational defects. Because of the high absorption coefficient of water in the infrared, it makes a valuable addition to the mixture. An investigation of the effects of the solvent-to-water ratio within the flash-frozen target on the resulting RIR-MAPLE-deposited films has shown that there is an optimal window in which the ratio of ejected material in the vaporous and liquid phases contributes to improved surface morphology and the dependent optical properties [23]. Three important aspects were considered: the polymer must be soluble in the solvent; the solvent must not sublimate, or dry out the target, prior to laser-ablated deposition; and all solvents must possess a high density of hydroxyl bonds for efficient absorption of the laser energy. Rather than relying on one solvent, like toluene with good solubility characteristics, but a high vapor pressure, two solvents were used. For example, toluene could be used to dissolve the polymer, and then phenol, with one fifth the vapor pressure of toluene, could be added to slow down the natural sublimation process at low pressure. In addition, due to the high density of hydroxyl bonds and large absorption coefficient, water was added to complete an emulsion. Two conclusions were reached: water-rich targets had larger absorption coefficients, on the order of $\alpha = 1000$ cm^{-1}, which led to shallower absorption depths, vapor-rich plumes, and smooth films; and, films with higher phenol content had smaller absorption coefficients, on the order of $\alpha = 10$ cm^{-1}, which led to deeper absorption, liquid-rich plumes, and rougher films that were significantly repaired upon annealing due the excess trapped solvent in the film.

The important point is that process parameters have a large effect on the re-

sulting polymer films. This and other studies have motivated a full characterization of the RIR-MAPLE process to determine if there is any correlation between one or more RIR-MAPLE process inputs and one or more film-trait outputs. A summary of achievements to date was published in 2011 [20] that highlights superior hole mobility and interchain interactions in the polymer poly[2-methoxy-5-(2-ethyl-hexyloxy)-p-phenylene-vinylene] (MEH-PPV), controllable surface and internal morphologies, and multilayered deposition. These traits are difficult, if not impossible, to achieve simultaneously using solution processing methods, but that RIR-MAPLE can readily accomplish.

2

Enabling Capabilities Demonstrated for Emulsion-Based, RIR-MAPLE Deposition

We now present work that addresses unresolved questions of basic material properties of emulsion-based RIR-MAPLE films. Previous work in our group has focused on understanding the impact of growth parameters, such as target-to-substrate distance, target composition, and post-deposition annealing, on the deposited film surface roughness [11, 23]. Two additional questions related to the construction of thin films by RIR-MAPLE have been investigated in this work. The first is whether RIR-MAPLE deposition affects the molecular weight of the polymer that is being deposited. The second is whether the capability for multilayer heterostructures of nanocomposite and polymer films can be proven with characterization of the cross-sectional morphology.

2.1 Polymer Deposition without Reduction of Molecular Weight

The molecular weight of a conjugated polymer plays a central role in the optoelectronic properties of thin films. Properties such as absorption, carrier mobility, charge

transport, and device efficiency are sensitive to chromophore length and polymer chain-packing morphology, which in turn depend on the preparation conditions and the molecular weight of the polymer [27]. For example, it has been demonstrated that larger molecular weight poly(3-hexylthiophene) (P3HT) films lead to larger carrier mobilities and red-shifted absorption spectra in organic field-effect transistors [28, 29] and organic photovoltaic solar cells [30] compared with lower molecular weight samples. Organic light-emitting diodes have shown increased electroluminescence intensities and better spectral stability at higher molecular weights [31]. The larger molecular weight improves charge transport by packing the chains more closely, which increases π-π orbital interactions, and by linking otherwise isolated crystalline domains for better hopping transport. Therefore, it is important that the use of a given deposition technique does not structurally degrade the polymer. A variety of pulsed laser deposition and MAPLE techniques have yielded polymer films for which the chemical integrity remains intact, as characterized by proton nuclear magnetic resonance (^{1}H NMR) and Fourier transform infrared (FTIR) spectroscopies. However, gel permeation chromatography (GPC) measurement of the structural integrity of the polymers often finds a reduction in molecular weight after deposition [13, 14, 32–34].

In this section, the effects of the emulsion-based RIR-MAPLE thin film deposition technique on polymer molecular weight are presented. Poly(methyl methacrylate) (PMMA) is included in the study as a standard reference due to the availability of sharply peaked size distributions over a wide range of molecular weights. A unique aspect of this work is that the molecular weight for polymers that are important for optoelectronic devices are characterized by GPC measurement: P3HT, which is widely used in organic photovoltaics and organic transistors; and, MEH-PPV, which has been an important polymer in the development of organic light-emitting diodes and organic photovoltaics. The molecular weight of each polymer is deter-

mined by GPC both before and after deposition by emulsion-based RIR-MAPLE. A survey of the literature yielded several published values of the molecular weight of laser-deposited polymer films. These results are compiled for comparison with the present work. Complementary characterizations by ^{1}H NMR spectroscopy and FTIR spectroscopy provide information on the chemical integrity of the polymers.

2.1.1 RIR-MAPLE Deposition

All samples were deposited by emulsion-based RIR-MAPLE onto soda-lime glass slides, except for the FTIR samples, which were deposited onto undoped silicon. The RIR-MAPLE parameters were standardized across depositions to the following values: a target-to-substrate distance of 70 mm; an ambient chamber pressure of 10 μTorr; and, a substrate temperature of 4 °C. The targets consisted of emulsions of multiple solvents, in contrast with traditional solution casting, which generally uses a single solvent. PMMA was prepared as a 1 wt% solution in trichloroethylene (TCE) as the primary solvent, to which benzyl alcohol (BnOH) was added as a secondary solvent. Deionized (DI) water was then added in a 2:1 water:solution weight ratio to complete the emulsion. The P3HT emulsion target was prepared using the same polymer/solvent/DI water ratios, with TCE as the primary solvent and phenol as the secondary solvent. Finally, MEH-PPV was prepared using the same ratios, with toluene as the primary solvent and phenol as the secondary solvent.

2.1.2 Gel Permeation Chromatography Measurements

GPC measurements provide information on the size distribution of observed particles, and are sensitive to a number of parameters. The use of light scattering to determine molecular weight is best suited to spherical particles. As the particle shape deviates from a sphere, as it does with linear polymers, there will be an error introduced into the measurement [35]. It is well-known that molecular weight

Table 2.1: Molecular weight of polymers deposited by PLD, UV-MAPLE and RIR-MAPLE. Values from this work are averages of multiple samples. M_w % Change indicates the change in M_w after deposition relative to the native polymer. (*M_n–number-averaged molecular weight).

Author	Polymer	Solvent	Method	Laser λ (nm)	Native M_w (kDa)	Deposited M_w (kDa)	M_w % Change
Bubb [33]	PLGA	–	RIR-PLD	2940	8.495	3.125	63.2
Bubb [33]	PLGA	–	RIR-PLD	3400	8.495	3.470	59.2
Mercado [51]	PLGA	–	UV-PLD	248	99	8	91.9
Mercado [51]	PLGA	Chloroform	UV-MAPLE	248	99	26	73.7
Bubb [32]	PEG	DI Water	UV-MAPLE	193	1.397	1.325	5.2
Bubb [32]	PEG	Chloroform	UV-MAPLE	193	1.397	1.077	22.9
Fitz-Gerald [52]	[Ru(bpy $PMMA_2)_3$]–$(PF_6)_2$	Dimethoxyethane	UV-MAPLE	248	*33.0	*9–12	68.2
Sellinger [53]	PMMA	Toluene	UV-MAPLE	248	13.9	12.8	7.9
McCormick	PMMA	TCE/BnOH/H_2O	RIR-MAPLE	2940	9.57	11.2	3.3
McCormick	PMMA	TCE/BnOH/H_2O	RIR-MAPLE	2940	109.4	117.0	6.9
McCormick	PMMA	TCE/BnOH/H_2O	RIR-MAPLE	2940	367.2	354.2	3.5
McCormick	P3HT	TCE/Phenol/H_2O	RIR-MAPLE	2940	42.5	45.3	6.6
McCormick	MEH-PPV	Toluene/Phenol/H_2O	RIR-MAPLE	2940	266.9	133.7	49.9

measurements of rigid backbone polymers, taken on a GPC system that has been calibrated with polystyrene standards, tend to overestimate the true weight-averaged molecular weight (M_w) values.

However, relative measurements, such as those reported here, minimize such biases due to the identical offset introduced throughout a data set. Similarly, reported values of the refractive index increment dn/dc of a given polymer tend to be inconsistent. Because the increment affects different samples of the same material equally, any systematic error present is eliminated with a relative comparison. Thus, the change in molecular weight, denoted "M_w % Change," from the RIR-MAPLE deposited polymer relative to the native polymer is reported. A positive value indicates an increase in M_w after deposition, while a negative value indicates a decrease. The measured molecular weight values, both from existing literature and the current work, are presented in Table 2.1 and shown in Figure 2.1. The diagonal line separates the materials into post-process degradation or polymerization. A symbol on or near the line indicates no change in the molecular weight after the cited deposition

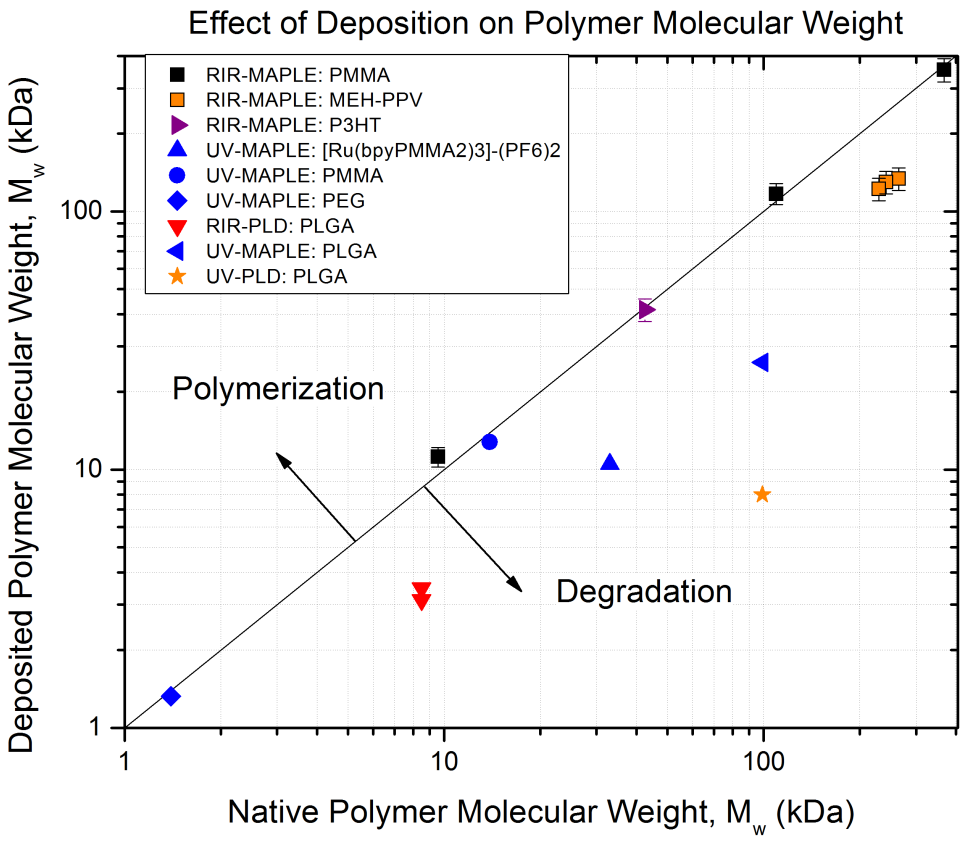

FIGURE 2.1: Molecular weight of polymers before and after deposition by the stated deposition technique. All RIR-MAPLE data were generated by the author.

process.

Bubb et al., used RIR-PLD to deposit the copolymer poly(lactide-co-glycolide) (PLGA) for a drug delivery coating application [14]. GPC measurements indicated the molecular weight of the polymer was less than half that of the native polymer. Mercado et al., explicitly compared thin films of PLGA deposited by UV-PLD and UV-MAPLE [32]. A molecular weight distribution analysis via GPC revealed significant differences between the native and deposited polymers for both deposition techniques. Bubb et al., also used UV-MAPLE depositions of polyethylene glycol (PEG) to establish that the solvent plays an important role in determining the level of structural degradation, with DI water yielding less structural degrada-

tion of the polymer compared to chloroform [13]. It was concluded that chloroform yielded chemically reactive chloride species during deposition that were responsible for structural degradation of the polymer, while water did not photodissociate into reactive species and did not generate structural changes in the polymer to the same extent. Fitz-Gerald et al., reported on the UV-MAPLE deposition of a Ruthenium-based PMMA polymeric metal complex [33]. A low-M_w peak in the size distribution indicated partial cleavage of the PMMA chains.

Sellinger et al., looked at a nanocomposite of carbon nanotubes embedded within a PMMA matrix [34]. GPC analysis revealed a molecular weight reduction of the PMMA, most likely due to the polymer absorption of UV light. From this existing work, a few trends can be observed. The PLD films all exhibited significant M_w degradation regardless of laser wavelength, which is to be expected because the target consists of solid polymer, which must absorb the laser energy to desorb material for deposition. The UV-MAPLE films also exhibited degradation compared with the native polymer. Total degradation of the UV-MAPLE process may be due both to direct light absorption by the polymer and to chemical degradation of the polymer from highly reactive species created via photodissociation of the solvent [13]. Overall, it is clear that RIR- and UV-PLD techniques cause significant structural degradation of the deposited polymer. Likewise, UV-MAPLE results in a global reduction of molecular weight, although the extent of the molecular weight degradation can be minimized.

In contrast, the emulsion-based RIR-MAPLE depositions in Table 2.1 show the least amount of structural degradation because the solvent emulsion is responsible for the majority of the IR laser light absorption at the hydroxyl bond stretch; the polymer absorbs very poorly in this wavelength regime. The PMMA polymer provides a good example of this fundamental difference as it can be compared directly to other laser deposition techniques represented in Table 2.1. Three different

PMMA molecular weights, M_w = 10 kDa, 100 kDa, and 350 kDa, were chosen to span a range representative of polymers. Wyatt Technology reports a ±5% system error for the molecular weight measurement, which encompasses the light scattering and refractive index measurements. The weight-averaged molecular weights, M_w, of the 10 kDa and 100 kDa PMMA samples demonstrate an increase in the molecular weight that deviates from the native values by less than or slightly more than, respectively, the reported system error. The 350 kDa PMMA sample demonstrated a molecular weight reduction of 3.5%, which is within the system error. Therefore, the GPC distributions of the PMMA standards reflect a negligible change of the RIR-MAPLE-deposited material from the native polymer. These results also demonstrate that emulsion-based RIR-MAPLE does not have an inherent molecular weight limit, within the 10-350 kDa range, to prevent a polymer from being deposited intact. It is important to note that the PEG sample in Table 2.1 that was deposited by UV-MAPLE and had a 5.2% decrease in M_w [13], used DI water as the target solvent. The RIR-MAPLE emulsion technique features DI water as a major portion of the target matrix.

In the case of P3HT, the RIR-MAPLE-deposited sample increased in molecular weight compared with the native sample. Sigma-Aldrich reported the native polymer molecular weight as M_w = 42.5 kDa, which corresponds to a 6.6% increase for the RIR-MAPLE-deposited samples, as shown in Table 2.1. While it is well-known that P3HT cross-linking is the preferred mechanism (as opposed to chain scission) in the presence of air and UV or visible light [36], it is unlikely that cross-linking would occur to such a degree given that the polymer samples were kept in light-shielded cases under vacuum. Such significant cross-linking would lead to a loss of solubility, which was not observed.

Only MEH-PPV exhibited structural degradation after RIR-MAPLE deposition, with a consistent halving of the weight-averaged molecular weight. Figure 2.2 shows

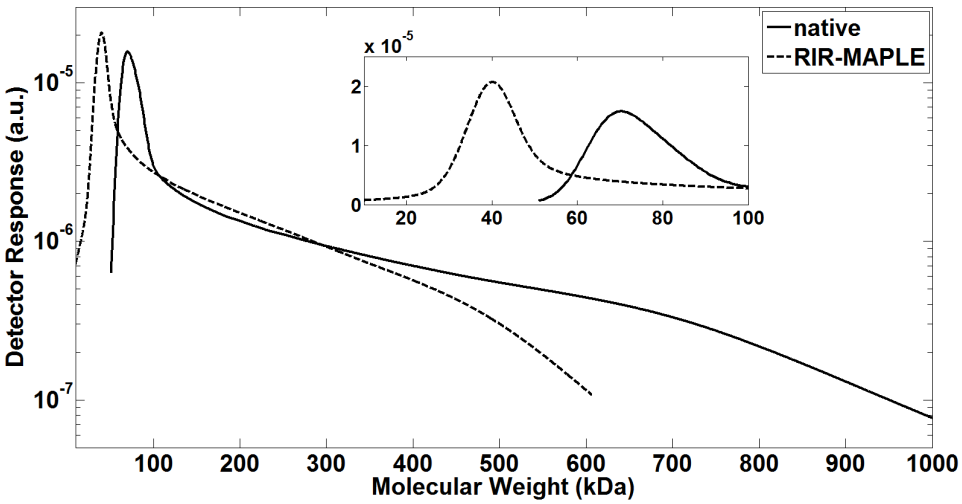

FIGURE 2.2: GPC measurements of the native MEH-PPV polymer and the resulting distributions after RIR-MAPLE deposition. The log-scale plot emphasizes the reduction in the largest molecular weights after deposition. The inset shows the peak values on a linear scale. These distributions are representative of repeated GPC measurements.

the GPC traces of single representative MEH-PPV samples before and after deposition by emulsion-based RIR-MAPLE. Because the distribution is skewed, the data are plotted on a log-scale plot to emphasize the higher molecular weight tails. The inset clearly shows a shift of the peak value from 70 kDa to 40 kDa in the RIR-MAPLE deposited sample. Furthermore, it is evident from the high molecular weight tails that there is a reduction of the highest molecular weights present in the two samples: the native sample has molecular weights up to 1 MDa, while the sample after RIR-MAPLE deposition has maximum molecular weight values of 600 kDa. Analysis of PMMA with nominal M_w = 350 kDa, which is roughly 100 kDa larger than the MEH-PPV native polymer, showed that there was no change in the PMMA molecular weight after RIR-MAPLE deposition. Therefore, even if an upper limit to the deposition capabilities of RIR-MAPLE does exist with respect to the molecular weight, MEH-PPV should be well below that limit. In fact, Figure 2.2 shows that the MEH-PPV sample after deposition by RIR-MAPLE has molecular

Table 2.2: Polydispersity index (PDI) of polymers deposited by PLD, UV-MAPLE and RIR-MAPLE. (*PDI not reported.)

Author	Polymer	Solvent	Method	Laser λ (nm)	Native PDI	Deposited PDI
Bubb [33]	PLGA	–	RIR-PLD	2940	1.22	3.05
Bubb [33]	PLGA	–	RIR-PLD	3400	1.22	2.63
Mercado [51]	PLGA	–	UV-PLD	248	1.73	2.70
Mercado [51]	PLGA	Chloroform	UV-MAPLE	248	1.73	2.00
Bubb [32]	PEG	DI Water	UV-MAPLE	193	1.02	1.06
Bubb [32]	PEG	Chloroform	UV-MAPLE	193	1.02	1.07
Fitz-Gerald [52]	[Ru(bpy $PMMA_2)_3$]–$(PF_6)_2$	Dimethoxyethane	UV-MAPLE	248	*	*
Sellinger [53]	PMMA	Toluene	UV-MAPLE	248	1.71	1.53
McCormick	PMMA	TCE/BnOH/H_2O	RIR-MAPLE	2940	1.12	1.04
McCormick	PMMA	TCE/BnOH/H_2O	RIR-MAPLE	2940	1.15	1.19
McCormick	PMMA	TCE/BnOH/H_2O	RIR-MAPLE	2940	1.45	1.59
McCormick	P3HT	TCE/Phenol/H_2O	RIR-MAPLE	2940	2.20	2.04
McCormick	MEH-PPV	Toluene/Phenol/H_2O	RIR-MAPLE	2940	2.29	2.18

weight values as high as 600 kDa.

At this point, it is also helpful to consider the polydispersity index (PDI) for the polymers described in Table 2.1. The PDI is defined as the ratio of the weight-averaged to the number-averaged molecular weights (M_w/M_n), and it provides an indication of how uniformly the molecular weight is distributed in a polymer sample, with a value of unity marking a monodisperse, narrow, highly-peaked size distribution. As the PDI increases past unity, the size distribution becomes less uniform, broader, and less peaked. Table 2.2 reports the PDI of the polymers described in Table 2.1. The RIR- and UV-PLD samples showed an increase of 57-150% of the native PDI, signifying a large increase in the number of different molecular weight values after deposition. In contrast, both UV-MAPLE and RIR-MAPLE have much smaller changes in PDI. The UV-MAPLE technique had PDI changes after deposition ranging from an 11% decrease to a 16% increase compared to the native PDI. The PDI of RIR-MAPLE-deposited polymers ranged from a 7% decrease to a 10% increase compared to the native PDI. Therefore, even if the GPC size distribution shifts to

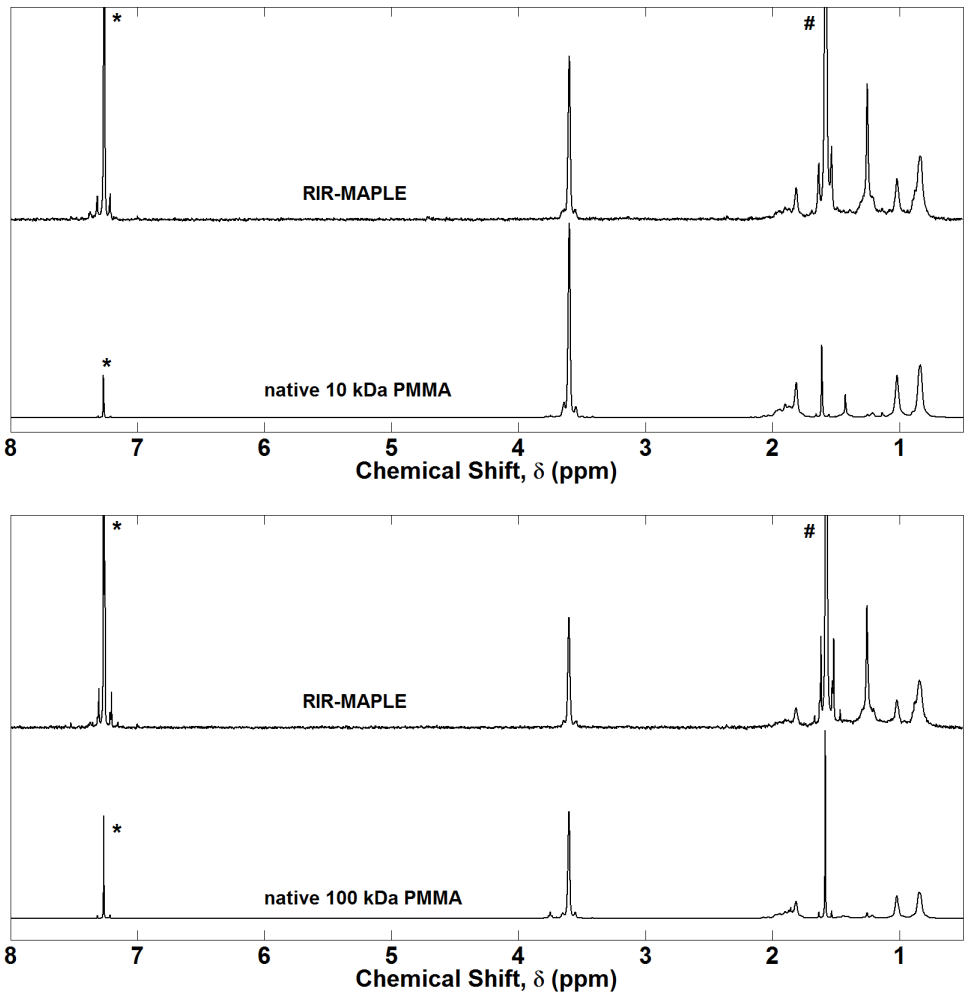

FIGURE 2.3: Proton NMR spectra of PMMA of molecular weight (a) 10 kDa, and (b) 100 kDa. The solvent peak at $\delta = 7.26$ ppm is denoted by *. The water peak at $\delta = 1.56$ ppm is denoted by #.

a different M_w value after deposition using MAPLE techniques, the distribution of the molecular weight values remains relatively constant.

2.1.3 ^{1}H NMR Spectroscopy and FTIR Spectroscopy

In order to determine if the observed change in molecular weight for MEH-PPV results from RIR-MAPLE deposition alone, or from a separate mechanism, such as chain scission, ^{1}H NMR and FTIR spectra were measured for PMMA, P3HT,

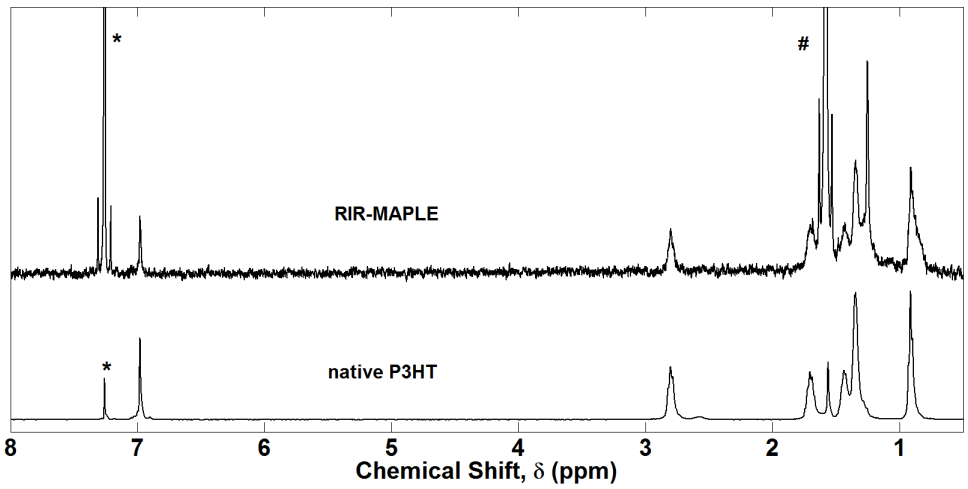

FIGURE 2.4: Proton NMR spectra of native P3HT polymer and RIR-MAPLE deposited samples. The solvent peak at $\delta = 7.26$ ppm is denoted by *. The water peak at $\delta = 1.56$ ppm is denoted by #.

and MEH-PPV before and after deposition by emulsion-based RIR-MAPLE. The ^{1}H NMR spectra of PMMA confirm the GPC results by reporting no change before and after RIR-MAPLE deposition, as shown in Figure 2.3. FTIR spectra are not reported for the PMMA samples due to the definitive and uneventful results of the other characterizations. The PMMA results represent a baseline for the other polymers applicable to optoelectronic devices by demonstrating that the RIR-MAPLE technique is capable of thin film deposition with little to no change in the native polymer within the wide range of 10–350 kDa.

The P3HT ^{1}H NMR spectra, shown in Figure 2.4, were slightly more complex. There was a small reduction in the thiophene proton peak near $\delta = 7$ ppm and changes in the amplitude, but not position, of the alkyl side group peaks. Integration of the α-carbon proton peaks in the region $\delta = 3.0$–2.5 ppm yielded a regioregularity of 92% [37], which agrees with the manufacturer specification of >90% regioregularity. The primary difference before and after RIR-MAPLE deposition is the sharp increase in the CH_2 peak at $\delta = 1.26$ ppm, which could indicate that the side chain

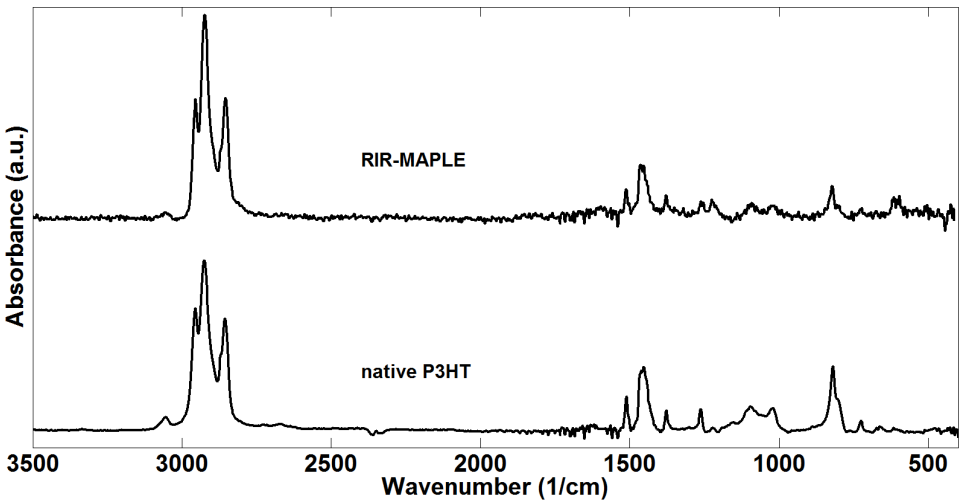

FIGURE 2.5: FTIR spectra of P3HT before and after RIR-MAPLE deposition.

has been shortened from six to five alkyl units. This shortening is not great enough to lead to an appreciable difference in solubility; moreover, a solubility difference was not observed. The P3HT FTIR spectra in Figure 2.5 contain the requisite peaks both before and after RIR-MAPLE with no significant differences. Following Chen et al., the observed peaks are assigned as [38]: the aromatic C–H stretch near 3057 cm^{-1}; the aliphatic C–H stretches at 2954, 2925 and 2856 cm^{-1}; the ring stretches at 1510 and 1454 cm^{-1}; the methyl deformation at 1377 cm^{-1}; the out-of-plain aromatic stretches at 820 cm^{-1}; and, the methyl rocking stretch at 725 cm^{-1}.

The MEH-PPV ^{1}H NMR spectra, shown in Figure 2.6, contain marked differences before and after RIR-MAPLE deposition. The aliphatic solvent chloroform-d ($CDCl_3$), which tends to dissolve the alkyl side chains better than the aromatic backbone, was used for sample preparation [39]. MEH-PPV is a well-studied polymer with a ^{1}H NMR spectrum that has been extensively catalogued [40–42]. There are three regions of interest in the MEH-PPV spectrum: the downfield aromatic groups (δ = 7.55–7.45 ppm, ArH) and vinyl double bonds of the backbone (δ = 7.23–7.12 ppm, vinyl HC=CH); the midfield alkoxy groups (δ = 3.95, 3.92 ppm, OCH_2, OCH_3); and

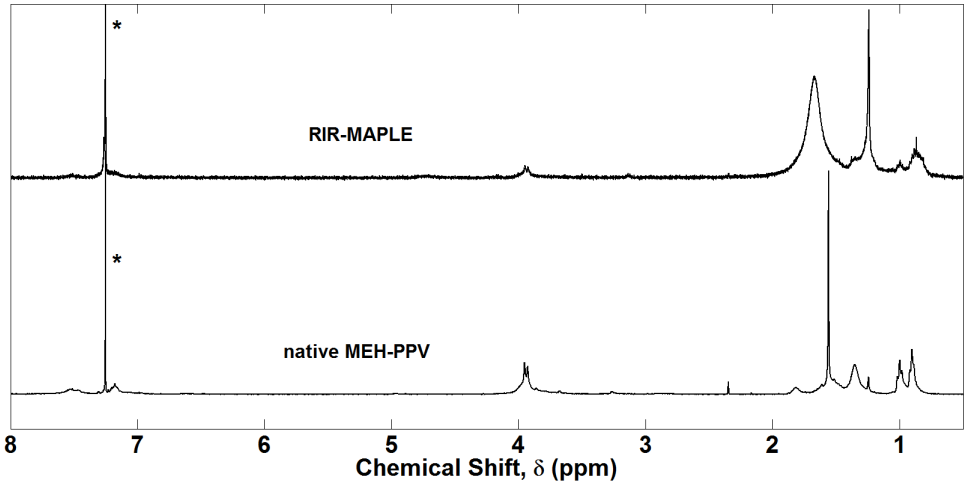

FIGURE 2.6: Proton NMR spectra of native MEH-PPV and of MEH-PPV after RIR-MAPLE deposition. The solvent peak is denoted by *.

finally, the upfield alkyl side chains (δ = 1.81, 1.65, 1.60, 1.55, 1.35, 1.24 ppm, CH, CH_2), (1.02, 0.99, 0.97; 0.92, 0.90, 0.88 ppm, CH_3). The aromatic peaks remained constant in both location and magnitude, indicating that the benzene ring in the polymer backbone remained intact. The vinyl double bond peaks decreased after RIR-MAPLE, indicating a decrease in the number of these bonds, which supports the chain scission seen in the molecular weight distributions. The side chain peaks were dramatically different before and after RIR-MAPLE. The peaks corresponding to the CH and CH_2 groups in the δ = 1.88–1.40 ppm region broadened significantly, and resulted in a complete loss of structure. If chemical degradation had occurred, the broad peak would be an indicator of a multitude of different alkyl products [43]. However, as demonstrated by the FTIR spectra to follow, such chemical degradation does not occur. The CH_2 peak at δ = 1.35 ppm remained constant, while there was an increase in the CH_2 peak at δ = 1.24 ppm. The methyl groups in the δ = 1.02–0.88 ppm region were intact, but the grouping at δ = 0.92–0.88 ppm exhibited a broadening to δ = 0.92–0.81 ppm. All of these changes in the ^{1}H NMR spectra demonstrate substantial modification of the side chains after deposition by

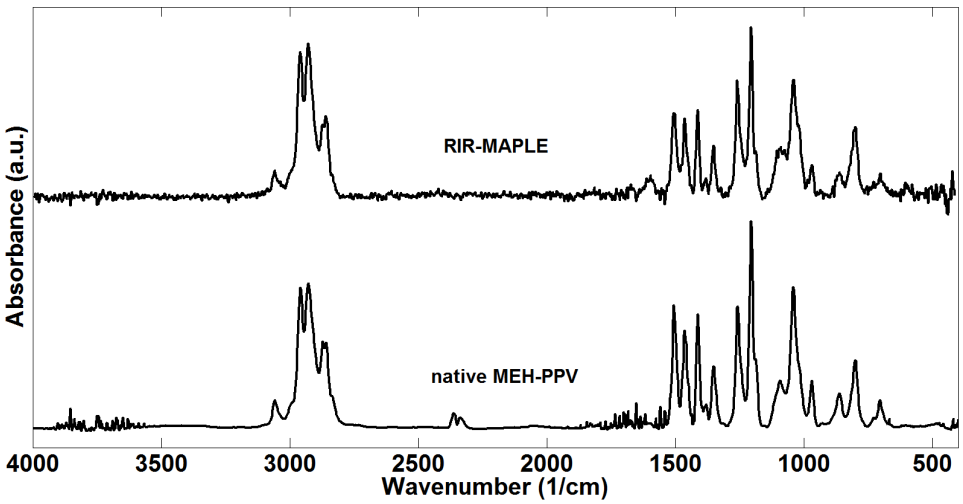

FIGURE 2.7: FTIR spectra of MEH-PPV. There is no difference between the native polymer and the RIR-MAPLE deposited polymer.

emulsion-based RIR-MAPLE. The solubility of the polymer would be impacted if the side chain modification is severe or leads to complete removal. Yet, the MEH-PPV solubility was not significantly changed after RIR-MAPLE because dissolution of the polymers for ^{1}H NMR and GPC analysis was still possible. However, substantial modification of the side chains could potentially lead to changes in the morphology of the deposited film due to altered interchain interactions and chain stacking, which would affect device properties such as carrier mobility and efficient exciton dissociation.

Figure 2.7 shows the FTIR spectra for MEH-PPV. The peak assignments follow Ram et al. [40]: 3058 cm^{-1} is the CH vinyl bond stretch; 2958 cm^{-1} is the CH_3 alkyl stretch; 2928 cm^{-1} is the CH alkyl stretch; 2858 and 2872 are the CH_2 alkyl stretch; 1600, 1506, 1464 and 1413 cm^{-1} are various phenyl stretches; 1351 cm^{-1} is the CH_2 alkyl deformation; 1259 and 1205 cm^{-1} are the phenyl oxygen stretches; 1041 cm^{-1} is the alkyl oxygen stretch; and 969 cm^{-1} is the vinyl CH wag. From these FTIR spectra, there appears to be no change in the chemical bonds of MEH-PPV due to RIR-MAPLE. The FTIR and ^{1}H NMR results are not contradictory. Because ^{1}H

NMR probes chemical bonds and their local magnetic environment, it is possible to demonstrate no change in the specific bonds present via FTIR and also to find differences in the ^{1}H NMR spectra due to structural changes in the polymer.

Therefore, polymers deposited by emulsion-based RIR-MAPLE can be expected to contain the same molecular weight and no chemical degradation as the native polymer material.

2.2 Polymer-Based Multilayer Heterostructures

As discussed in Chapter 1, multilayer heterostructures that include polymers are difficult to achieve using solution-casting methods. For example, if orthogonal solvents are not available for the desired materials, other exotic techniques are required to approximate a layered heterostructure. One such technique involves creating each layer separately on its own substrate, then removing the film from the substrate by floating it off the substrate onto the surface of a water bath, and finally, carefully placing the floating film onto the first layer that has been deposited onto the final device substrate [44]. In this section, multilayer structures of nanocomposites and/or polymer films are demonstrated to be straightforward to achieve with emulsion-based RIR-MAPLE.

The Stiff-Roberts group has previously investigated the planar colloidal quantum dot (CQD) distributions within nanocomposite films deposited using two different RIR-MAPLE target composition methods [22]: sequential deposition, where the polymer emulsion and the CQD in solution were each separately flash frozen adjacent to one another yet composed a single target; and, simultaneous deposition, where the RIR-MAPLE target was composed of a mixture of the polymer emulsion and the CQD in solution. Planar TEM images were taken for both configurations in the x-y plane, as shown in Figure 2.8.

It is clear from Figure 2.8 that simultaneous deposition results in much greater

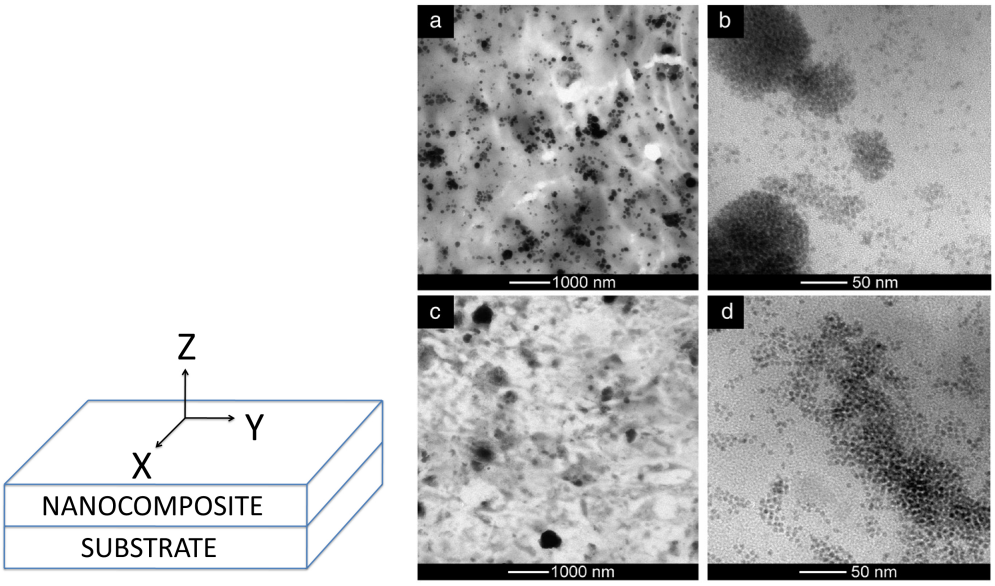

FIGURE 2.8: TEM images of RIR-MAPLE-deposited nanocomposite taken in the x-y plane as defined above. (a,b) Simultaneous MAPLE deposition. (c,d) Sequential MAPLE deposition.

CQD clumping. The images of sequential deposition show a much more dispersed distribution of CQD within the polymer. However, this is a two-dimensional (2D) result that says nothing of the CQD distribution in the vertical z-direction. To probe the distribution along this direction, focused ion beam (FIB) milling is used to section a slice of material out of a film to be imaged by cross-sectional transmission electron microscopy (XTEM). Therefore, the goal of this work was not only to investigate and determine the as-deposited vertical distribution of CdSe colloidal quantum dots within a polymer matrix, but also to demonstrate that high-quality multilayer structures can be grown by RIR-MAPLE in a straightforward manner.

2.2.1 RIR-MAPLE Deposition

The nanocomposite/polymer multilayer nanocomposite structure shown in Figure 2.9 was grown for this experiment. The nanocomposite layers were composed of 40% CQD and 60% MEH-PPV polymer, and the entire structure was deposited onto an

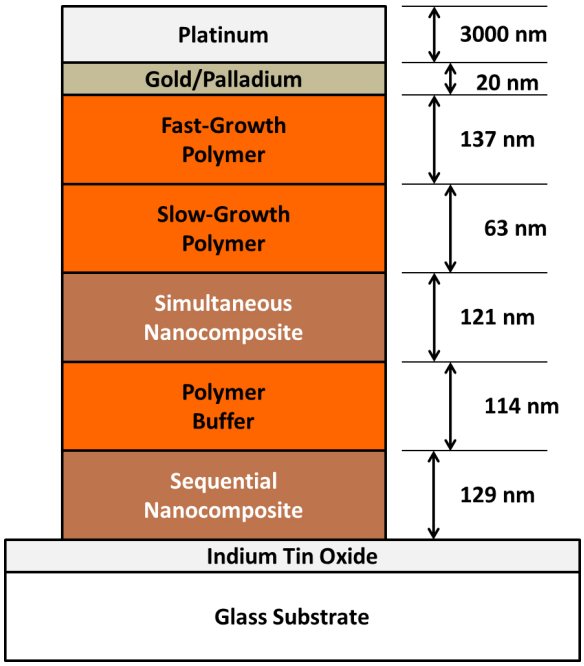

FIGURE 2.9: Schematic of XTEM sample showing average as-grown layer thicknesses.

indium-tin-oxide-coated (ITO) glass substrate. The substrate was at room temperature during all depositions.

The sequential nanocomposite was deposited for a total of 9.75 hours, in two sessions of 5.75 hours and 4.00 hours, with average growth rates of 10.4 nm/hr and 18.0 nm/hr, respectively, and an overall rate for the layer of 13.3 nm/hr. Atop the nanocomposite, a polymer-only buffer layer of MEH-PPV was deposited at a rate of 16.3 nm/hr. The simultaneous nanocomposite was deposited at an average rate of 15.1 nm/hr. The slow-growth polymer layer was grown at a rate of 15.6 nm/hr. The first four layers described were all grown at the maximum target-substrate (TS) distance of 7 cm. By decreasing the TS distance to 4 cm, the fast-growth polymer layer was deposited at an average rate of 34.4 nm/hr, which is 2.2 times the slow rate. The deposition rates were determined by measurement of the layer thicknesses from the cross-sectional image. It should be noted that measurements were taken across the

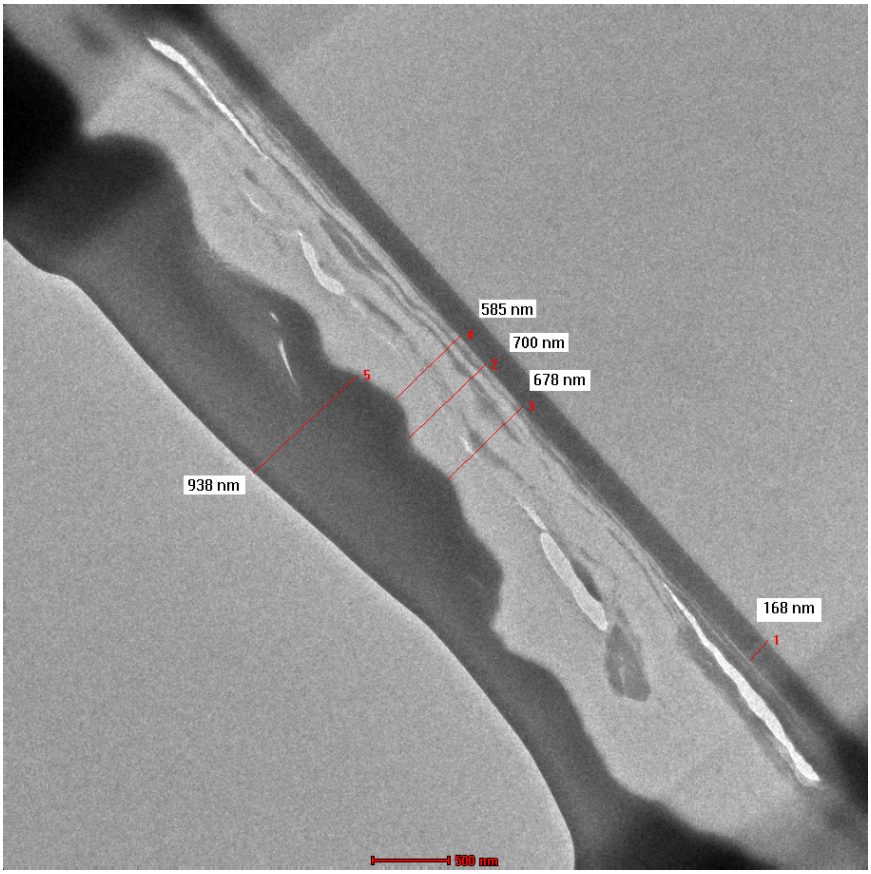

FIGURE 2.10: XTEM sample deposited by RIR-MAPLE. The glass substrate is at the top right. The uniform ITO bar is 168 nm thick. The white areas are tears between the layers due to the FIB sample preparation. Three measurements of the total RIR-MAPLE-deposited thickness are taken across the sample at locations of minimal tearing. The Pt thickness is also indicated. See the text for analysis.

region of the sample where there was no separation or tearing of the layers, which is seen below in both Figure 2.10 and Figure 2.11. The two target compositions, sequential and simultaneous, were differentiated by incorporating polymer-separated layers from each target composition. The ITO-coated glass substrate prevented charging of the sample during the FIB milling process.

Preparation of the nanocomposite sample for FIB milling requires sputter-coating the sample with 20 nm of Au/Pd, and then organometallic deposition of Pt atop the Au/Pd. It was unclear whether the metallic coating process was damaging the

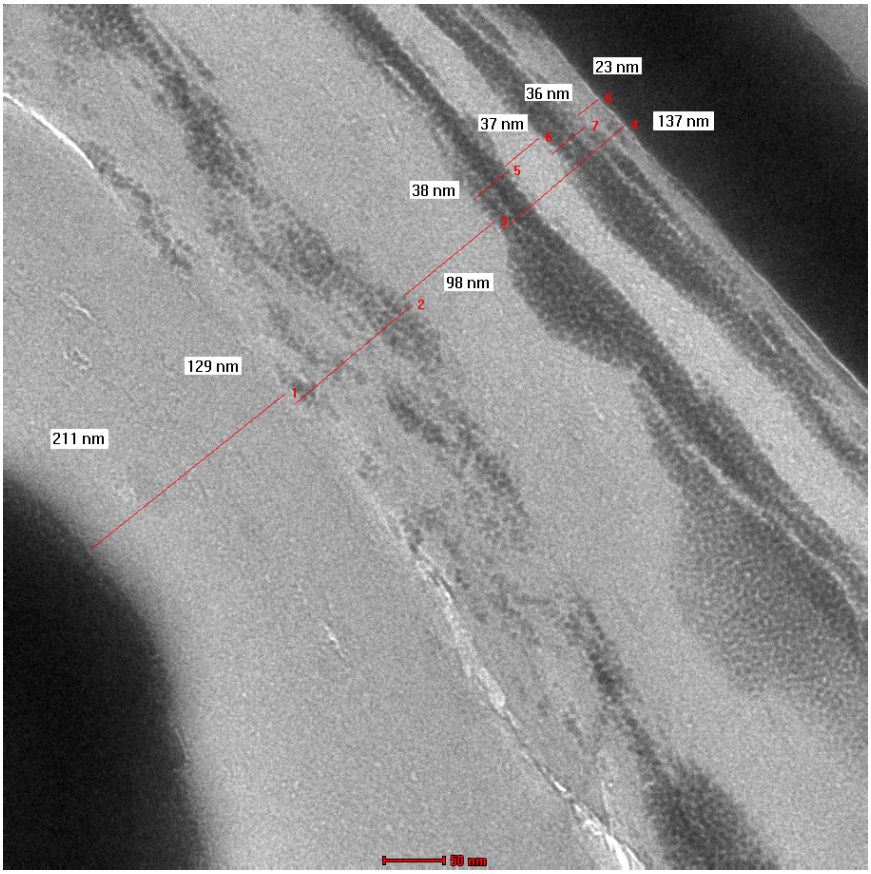

FIGURE 2.11: Zoom of second XTEM sample. Black bar at upper right is the ITO layer atop the glass substrate. The sequential layer consists of the four light and dark striations of 137 nm thickness. There is a polymer buffer layer of 98 nm thickness, then the 129-nm-thick simultaneous polymer layer. A slow-growth polymer layer of 129-nm thickness is followed by a fast-growth 211-nm-thick layer. The bottom left shows the metallic cap of Au/Pd and Pt.

nanocomposite layer, so the nanocomposite was separated from the metallic coating by a buffer layer of pure MEH-PPV polymer. The buffer layer was split into two separate layers, a slow-growth layer and a fast-growth layer, so that a comparison between the effects of the two deposition rates of the polymer could be accomplished with little extra effort (see schematic in Figure 2.9). The purpose of the separate layers was to examine the difference in morphology, with the expectation that the slow-growth layer would have far fewer crystallite domain inclusions. Crystallites are domains

that exhibit short-range crystal-like order, yet are not amorphous. Large crystallite domain formation generally occurs at higher growth rates due to the growth time scale being faster than the polymer needs to order itself in the bulk.

2.2.2 Cross-Sectional Transmission Electron Microscopy

The structure and thicknesses of the layers of the XTEM sample are shown in Figure 2.10. Three things are evident: the metallic layer on the lower left shares an uneven interface with the fast-growth polymer buffer layer; the white areas indicate that the film has separated at the boundaries between the RIR-MAPLE-grown layers; and, the layer consisting of the RIR-MAPLE-grown layers and the metallic deposition has a constant thickness. The constant thickness of the layer can be explained by the FIB milling required to disconnect the lift-out stylus from the sample. The uneven interface could occur from either the metallic sputtering, resulting in local heating and reflowing of the polymer layer or the film separating during the lift-out process, which would locally change the thickness of the RIR-MAPLE-deposited layers. The film separation could also occur during the lift-out process. RIR-MAPLE has been shown to produce smooth films of even coverage with these materials at similar thicknesses, so it is unlikely that the layer discontinuities are due to the deposition process. Despite such challenges with the FIB preparation of a cross-sectional sample, these XTEM images clearly demonstrate that emulsion-based RIR-MAPLE is capable of depositing multilayer films of nanocomposites and polymers that all have the same solubility properties. The separate RIR-MAPLE-deposited layers are analyzed using a magnified XTEM image that shows the sharp interfaces between different films of the multilayer structure. In addition, this image can help elucidate differences in CQD nanocomposite distribution in the z-direction for sequential and simultaneous deposition.

As seen in Figure 2.11, the sequential deposition resulted in four striations of

polymer and CQD alone. This layer was grown in two separate sessions, which explains the two separate layers of CQD and polymer observed for the sequential nanocomposite deposition. However, the two RIR-MAPLE sessions were completed with identical settings and target recipe, but the second session produced a growth rate almost twice that of the first session when calculated from the average layer thicknesses and deposition times. The separate polymer and CQD striations discontinuously run the length of the sample, indicating that they may be globally present. It is clear in the planar TEM image of Figure 2.8 that there is still agglomeration of the CQD within the sequential sample, but on a smaller length scale than the simultaneous deposition. Because of the 2D nature of Figure 2.11, it is possible that the layering effect is due to local seeding of the separate materials along the surface of the substrate during the initial growth. Although the macroscopic effect of hours of deposition shows a mixed layer, locally, CQDs tend to attract CQDs and polymer attracts polymer due to the difference in the solubilities. it is possible that the layering effect is due to local seeding of the separate materials along the surface of the substrate during the initial growth. Although the macroscopic effect of hours of deposition shows a mixed layer, locally, CQDs tend to attract CQDs and polymer attracts polymer due to the difference in the solubilities. Combined, these effects would produce a patchwork of both single-phase and combined-phase domains that would influence the subsequently deposited layers.

The striations of Figure 2.11 could then be a cross-section of interleaved single-phase domains. Such interleaving would be advantageous for a photovoltaic device where the goal is to maximize the current by maximizing dissociation of photogenerated excitons. Further study of this issue is warranted to resolve the complete cause of CQD distribution within the polymer matrix in the vertical z-direction.

Within the simultaneous layer, the CQD are more unevenly dispersed within the polymer, and there is no sign of the uniphase layering of the sequential deposition. In

Figure 2.10, it is especially clear that there is a much larger agglomerated structure of CQDs near the bottom of the image with very few CQDs along the layer, which reinforces the findings of Figure 2.8. The simultaneous method is thus inferior to the sequential method for well-distributed two phase systems. The sequential method removes any unknown thermodynamic interactions between the two materials while collocated in the simultaneous target that may cause an uneven distribution of the materials throughout the target.

Comparison of the slow-growth and fast-growth polymer-only layers in Figure 2.11 reveals oval-shaped domains and other darker-colored inclusions within the fast-growth layer that are absent in the slow-growth layer. Because optoelectronic devices benefit from a smooth, uniform morphology of the material within the film, the slow-growth layer would be the optimal choice for device fabrication.

2.3 Conclusions

The results of this chapter have answered two fundamental questions about the capabilities of emulsion-based RIR-MAPLE deposition; namely, whether the technique can maintain the molecular weight of deposited polymeric films, and whether the technique can deposit multilayer films of materials with similar solubility characteristics while maintaining sharp interfaces. In each case, emulsion-based RIR-MAPLE has been demonstrated to have distinct advantages.

First, polymers deposited by this technique can be expected to have the same molecular weight and no chemical degradation as the native polymer material. Specifically, PMMA, P3HT and MEH-PPV were characterized both before and after RIR-MAPLE deposition by GPC, ^{1}H NMR and FTIR to determine if RIR-MAPLE had an effect on the molecular weight. Three molecular weights of a PMMA standard spanned the range M_w = 10-350 kDa and showed no decrease in molecular weight after RIR-MAPLE deposition. If RIR-MAPLE has an inherent limit to the molecular

weight that can be deposited without degradation, it is outside of the range defined by the PMMA depositions. P3HT also showed no change in molecular weight. In contrast, MEH-PPV experienced a halving of the molecular weight after RIR-MAPLE deposition. There is no evidence for photo-oxidative degradation of MEH-PPV, indicating that the observed effects are due to the RIR-MAPLE deposition. However, PLD, which has an M_w degradation range of 50-90%, and UV-MAPLE, which has a degradation range of 5-74%, causes more damage to deposited polymers. Therefore, this work establishes that, of the laser deposition techniques, emulsion-based RIR-MAPLE has the least effect on the molecular weight of the deposited polymers. Moreover, the RIR-MAPLE process does not fundamentally alter the polymer in the resultant films, giving confidence that a range of materials can be expected to perform as intended after they are deposited.

Second, emulsion-based RIR-MAPLE can deposit multilayer films of materials with similar solubility and maintain distinct layers with sharp interfaces. This capability was demonstrated by evaluating XTEM images of a nanocomposite/polymer multilayer film comprising MEH-PPV polymer and CdSe CQDs. In addition, this investigation revealed very different CQD distributions within polymer matrices in the z-direction for sequential versus simultaneous deposition of nanocomposites. The sequential deposition technique was shown to be preferable for blended films that require intimate mixing of the constituent materials.

These discoveries inform the emulsion-based RIR-MAPLE deposition used to enable important applications, namely gradient refractive index anti-reflection coatings (Chapter 4) and organic photovoltaic solar cell (Chapter 5). In each case, polymeric films with specific material properties tied to molecular weight are required. In addition, for each case, blended film morphology and layered structures are key to enabling the novel heterostructures that have been investigated.

3

Trade-offs of Emulsion-Based, RIR-MAPLE: Surfactant Effects

This chapter presents research performed to quantify the effects of the surfactant used in the emulsion-based, RIR-MAPLE process. Addition of a surfactant to the solvent/water mixture reduces the surface energy difference between the two materials and allows the surface area between them to increase [45]. Thus, a surfactant is required to allow the oil-like regions of solvent to mix thoroughly with the water regions to produce the smallest possible domains within the emulsion that is frozen into the laser target. The quality of the target emulsion directly affects the quality of the resulting thin film. A better mixed emulsion tends to give smoother and more contiguous films. Conversely, surfactants can act as insulating or trap-producing materials within optoelectronic devices that degrade the overall performance [46]. Therefore, an investigation of the effects of the surfactant on the characteristics of polymer thin films deposited by RIR-MAPLE was undertaken. The polymer poly(3-hexylthiophene) (P3HT), which is germane to optoelectronic devices such as organic photovoltaics (OPV), organic field effect transistors (OFET), and organic light emitting diodes (OLED), was chosen as the organic thin film deposition material for

investigation. The target emulsion surfactant used in this investigation was sodium dodecyl sulfate (SDS).

First, specular x-ray diffraction (XRD) measurements are presented that have identified a quantity of surfactant that balances the competing concepts of providing a meta-stable emulsion and of allowing a minimum amount to be incorporated into the deposited film. Thin P3HT films were then deposited, and the in-plane structure was characterized via grazing-incidence, wide angle x-ray scattering (GIWAXS) to examine the structure of films that include or omit surfactant. The effects of varying additional RIR-MAPLE parameters, such as deposition rate and thermal annealing, were also examined. Coupled with this study were in-plane hole mobility measurements as determined from organic field effect transistors (OFET). An analysis of the UV-visible absorbance transitions via a theoretical treatment developed by Frank Spano [47] allows structural order to be inferred. Finally, atomic force microscopy (AFM) images provide insight into the electrical and optical characterization results.

3.1 Presence of Emulsion Target Surfactant in P3HT Thin Films

RIR-MAPLE has a very large parameter space that can impact the growth of polymeric thin films, including target parameters and RIR-MAPLE process parameters. The target parameters include: P3HT polymer weight percent in its primary solvent; secondary solvent to primary solvent mass ratio; water to secondary solvent mass ratio; and, surfactant weight percent dissolved in the water to emulsify the solvent/water mixture. The process parameters include: laser fluence; in-situ substrate temperature; target to substrate distance; and chamber pressure.

In the course of identifying the best deposition parameters for P3HT thin films, an RIR-MAPLE deposition regime very different from those described previously was attempted: 0.30 wt% SDS surfactant, 2 wt% P3HT in primary solvent; 7:1 secondary:primary solvent mass ratio; 7.5:1 water:secondary solvent mass ratio; 220 °C

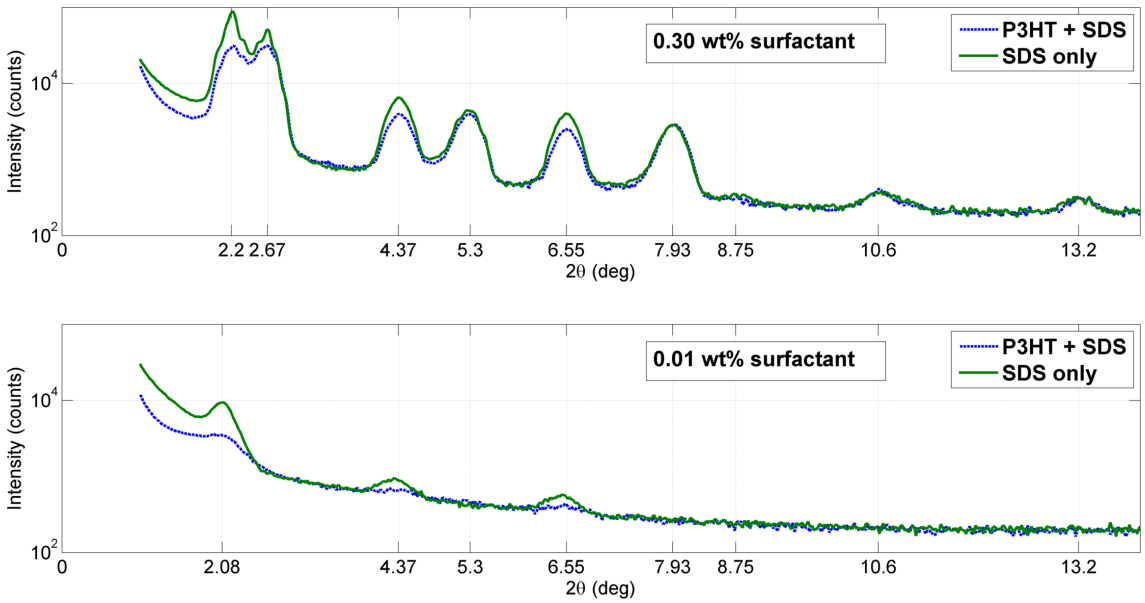

FIGURE 3.1: X-ray diffraction plots of RIR-MAPLE deposited P3HT films with 0.30 wt% and 0.01 wt% added sodium dodecyl sulfate (SDS) surfactant. For comparison, films without P3HT were deposited using the identical preparation and deposition parameters. It is clear that the peaks are due to the surfactant alone.

in situ substrate temperature; 4 cm target-substrate distance; and 1 mTorr chamber pressure. The primary solvent was trichloroethylene, and the secondary solvent was phenol. While several of these deposition parameters vary significantly from the standard growth regime, the very large surfactant content is atypical. In fact, after deposition of the film, the white color revealed that it was composed primarily of the SDS surfactant and not P3HT, which usually produces a purple film. XRD measurements were conducted on the surfactant-rich film in order to determine characteristic peaks that could be used to identify the presence of SDS in polymer thin films deposited by RIR-MAPLE. The measured XRD 2θ plot has nine peaks (Figure 3.1) whereas a typical P3HT film produces 1-3 peaks, depending on thickness and processing conditions. Another film was deposited in which all RIR-MAPLE parameters were repeated, except the surfactant quantity was reduced to 0.01 wt%. The resulting film appeared purple, indicating that the majority of the film was P3HT,

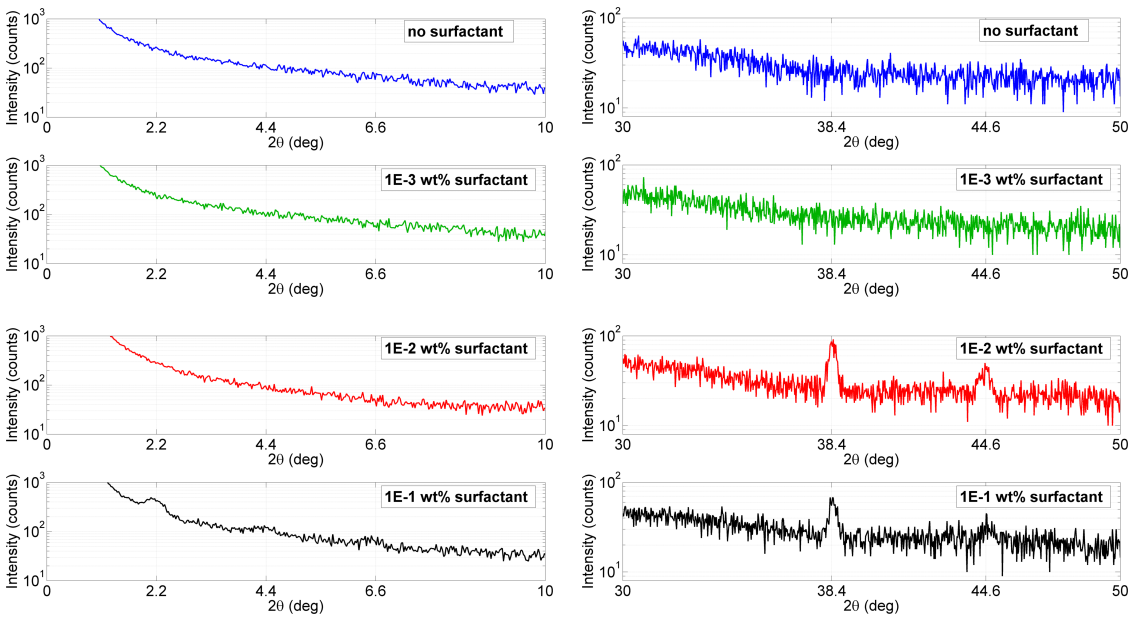

FIGURE 3.2: XRD results of P3HT films grown by RIR-MAPLE while varying the quantity of added SDS surfactant. In the lower 2θ range (left), the 0.1 wt% SDS film exhibited the same surfactant peaks identified in Figure 3.1. Additional peaks appeared in the higher 2θ range (right) of the 0.1 wt% SDS film and were reproduced in the 0.01 wt% SDS film. The 0.001 wt% SDS film showed no evidence of the surfactant.

and the XRD 2θ spectrum revealed three peaks. Both growth recipes were then repeated, except the P3HT was excluded. The results, shown in Figure 3.1, were almost identical to the films that included P3HT, which is evidence that the surfactant was superseding any P3HT crystalline structure that may have been present.

This initial XRD analysis provided the catalyst to investigate the effect of surfactant on RIR-MAPLE films more carefully. An important issue that must be resolved is to determine the optimum surfactant quantity that will produce an emulsion stable enough to remain mixed until frozen (i.e. meta-stable) in the RIR-MAPLE target, yet is small enough in quantity to minimize any negative effects the surfactant may have on final device performance for optoelectronic applications.

Therefore, the XRD study was repeated with the following RIR-MAPLE deposi-

tion parameters that are more typical for P3HT deposition: 1 wt% P3HT in primary solvent; 2:1 secondary:primary solvent mass ratio; 2:1 water:secondary solvent mass ratio; 20 °C in situ substrate temperature; 7 cm target-substrate distance; 10 μTorr chamber pressure. The primary solvent was ortho-dichlorobenzene (oDCB), and the secondary solvent was benzyl alcohol. This growth recipe was used to deposit four different samples, with the only difference being the amount of SDS surfactant added to the emulsion: no surfactant, 1E-3 wt%, 1E-2 wt%, and 1E-1 wt%. The XRD results are shown in Figure 3.2. The 1E-1 wt% SDS film exhibited the same signature peaks of the surfactant in the lower 2θ range that were observed in Figure 3.1. Additionally, peaks were found in the higher 2θ range that were not present in Figure 3.1, most likely due to the vastly different process and target parameters used for those depositions. These peaks in the higher 2θ range were also evident in the 1E-2 wt% surfactant film.

However, the 2θ trace for the 1E-3 wt% surfactant film was featureless in both the higher and lower 2θ ranges, similar to the film with no surfactant, indicating that there was not enough surfactant material in this film to form regularly spaced structures. As a result of this study, 1E-3 wt% surfactant in the target emulsion was identified as sufficient to maintain an emulsion stable enough to be frozen intact, yet insufficient to be observed by XRD in P3HT thin films This study highlights a significant balancing act with RIR-MAPLE target preparation: a well-mixed RIR-MAPLE target, which requires more surfactant, provides better thin film outcomes; however, at higher concentrations, the surfactant is transferred to the substrate in quantities that can alter the polymeric materials characteristics. For optoelectronic films that are heavily dependent on the characteristics of unadulterated materials for charge conduction, in particular, the presence of surfactant in the film could pose a major challenge. Therefore, the remaining studies determine the impact of this minimal surfactant concentration in the emulsion target on various characteristics of

P3HT.

3.2 Effect of Target Surfactant on P3HT Thin Film Structure

The structural and molecular characteristics of P3HT are well documented [48–50]. This polymer has been shown to have an anisotropic structure that can be defined by three crystallographic axes [50]. The a-axis is parallel to the aliphatic side chains; the b-axis is normal to the plane defined by the thiophene backbone, and the c-axis is parallel to the thiophene backbone. These directions can also be defined using traditional (hkl) crystallographic nomenclature: the a-axis is along the (h00) direction; the b-axis is along the (0k0) direction; and the c-axis is along the (00l) direction. For solution-based deposition of P3HT, the typical film morphology comprises the (010)-axis (or π-stacking) along the lateral, in-plane (IP) direction of the substrate and the (100)-axis (or lamellar stacking of the side chains) in the vertical, out-of-plane (OOP) direction of the substrate. The (001)-axis of the conjugated backbone is oriented parallel to the plane of the substrate. In the case of P3HT thin films deposited by emulsion-based RIR-MAPLE, the polymer structure was not known. Therefore, the purpose of this study was two-fold: to determine the polymer orientation and crystallinity of P3HT thin films deposited by RIR-MAPLE in comparison to typical spin-cast films and to determine the impact of the target emulsion surfactant on the P3HT thin film structure.

Different RIR-MAPLE deposition regimes were investigated by varying the following growth parameters: addition or omission of SDS surfactant in the emulsion; target-to-substrate (TS) distance; and, post-deposition heat treatment. The TS distance was set at either 4 cm or 7 cm, which corresponds to fast and slow deposition rates, respectively. In terms of heat treatment, samples were analyzed either as-deposited (AsDep) or post-deposition, vacuum-annealed (Ann) at 140 °C for 30 minutes.

The RIR-MAPLE emulsion target preparation was conducted as follows. All materials were prepared in organic solvents, but only half of the samples included surfactant to stabilize the water emulsion. P3HT was acquired from Sigma-Aldrich and used as received. The purity was listed as 99.995% based on trace metals analysis, and the number-averaged molecular weight was M_n = 70.52 kDa, with PDI = 1.7, which gives M_w = 119.9 kDa; and, the reported regioregularity was ⩾98%. The P3HT was dissolved in oDCB at a concentration of 0.5 wt%. The oDCB solution was then mixed with phenol in a 2:1 oDCB:phenol volume ratio. The two-solvent solution was visually verified to have no P3HT solute remaining undissolved before it was emulsified by adding deionized water. For each deposition, the emulsion vials were manually shaken and then placed in an ultrasonic water bath to disperse any agglomerated material prior to insertion in the target cup.

Materials characterization was accomplished by GIWAXS, which provides structural information about polymer orientation and crystallinity. Data were taken on two laboratory machines: an Anton Paar SAXSess system at Oak Ridge National Laboratory; and, a SAXSLab Ganesha system at Duke University. The GIWAXS technique involves irradiating the films in a reflection configuration at grazing incidence with a Cu-K_α x-ray point source and collecting the scattering profile on a two dimensional detector. The grazing angle was chosen to be 0.20°, which is larger than the critical angle for P3HT (0.14°) [51], but smaller than the critical angle of the silicon substrate (0.22°) [52]. Scattering angles less than the critical angle result in total external reflection, so only the P3HT film is probed to the exclusion of the silicon substrate.

GIWAXS structural studies of solution-cast P3HT films have demonstrated that without substrate surface treatment, polymer chain self-organization is dominated by the (100) orientation in the OOP direction [49]. The evidence presented herein shows that this is not the case with RIR-MAPLE films. Examples of RIR-MAPLE,

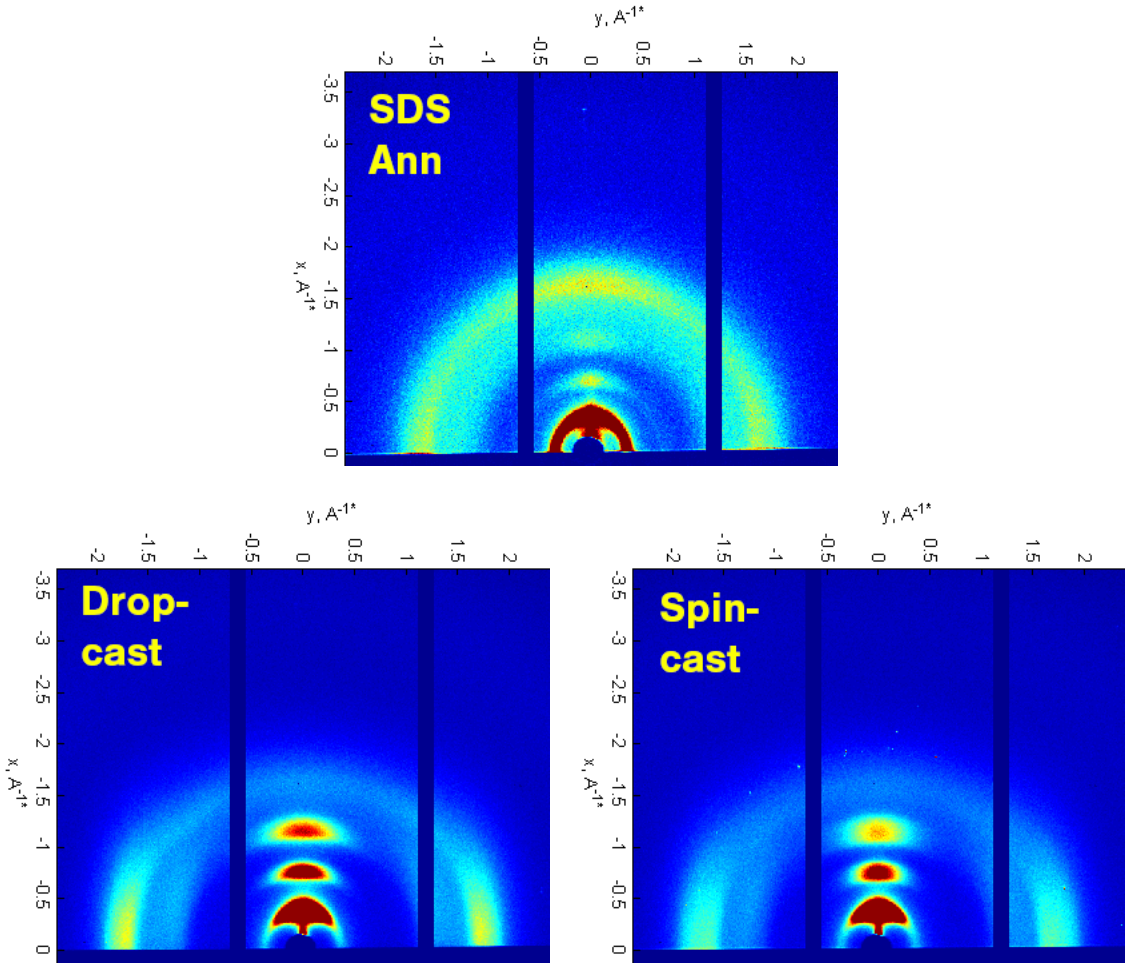

FIGURE 3.3: 2D GIWAXS measurements of a representative RIR-MAPLE-deposited P3HT thin film (top) compared with drop-cast (bottom, left) and spin-cast (bottom, right) P3HT thin films. RIR-MAPLE parameters are: 7 cm TS distance; with SDS; annealed at 140 °C for 30 minutes.

spin-cast, and drop-cast two-dimensional GIWAXS images are shown in Figure 3.3. Figure 3.4 shows the one-dimensional (1D) integration along the IP and OOP directions of the raw two-dimensional (2D) GIWAXS plots for an RIR-MAPLE-deposited P3HT film and compares the GIWAXS spectra to those for solution-cast films. For all GIWAXS data, the 1D integration was performed over the IP angles, 90°+20° and 270°-20°, and over the vertical angle, 180°±20°, for the OOP spectra.

The 2D GIWAXS plots are shown in Figure 3.5 and the 1D integration along

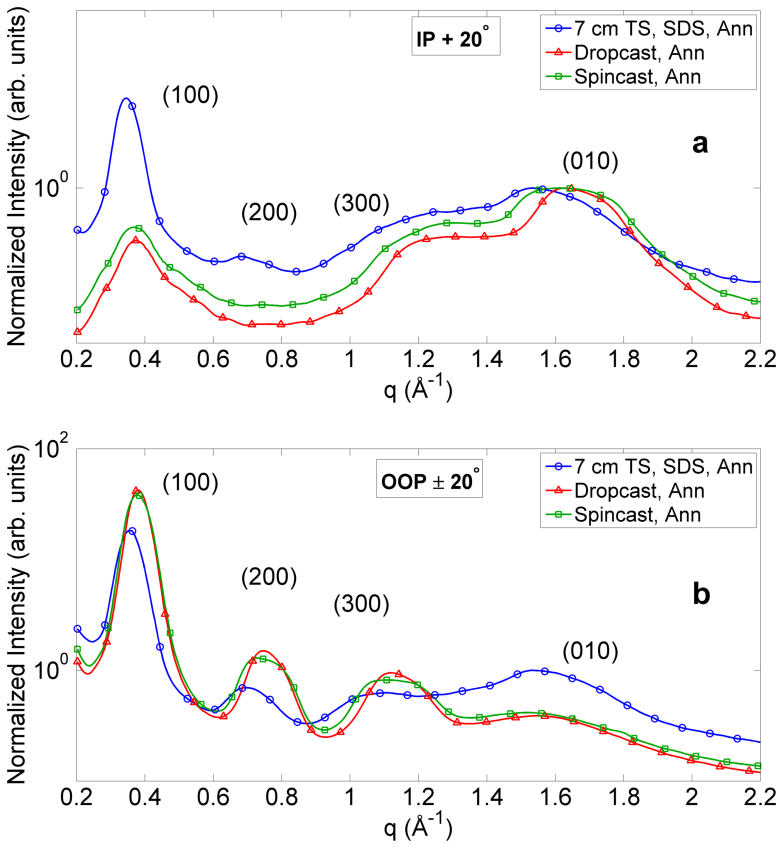

FIGURE 3.4: Comparison of one representative RIR-MAPLE sample with solution-cast films. (a) IP and (b) OOP GIWAXS measurements of P3HT films integrated from the IP or vertical angle $\pm 20^{\circ}$ and normalized to the (010) peak.

the IP and OOP directions of the 2D GIWAXS plots, are shown in Figure 3.6 and Figure 3.7, respectively, for RIR-MAPLE-deposited P3HT films with different parameters, showing the effects of varying the TS distance, the heat treatment, and addition of surfactant. The 1D plots have been normalized to the (010) peak again to account for the difference in scattering intensity between the 4-cm and 7-cm TS distance films that occurred because of the film thickness variations that resulted from constant deposition duration.

For a more detailed analysis of the data, the (010) peak values from all 1D GIWAXS spectra are summarized in Table 3.1; the peak-fitting program Fityk [53]

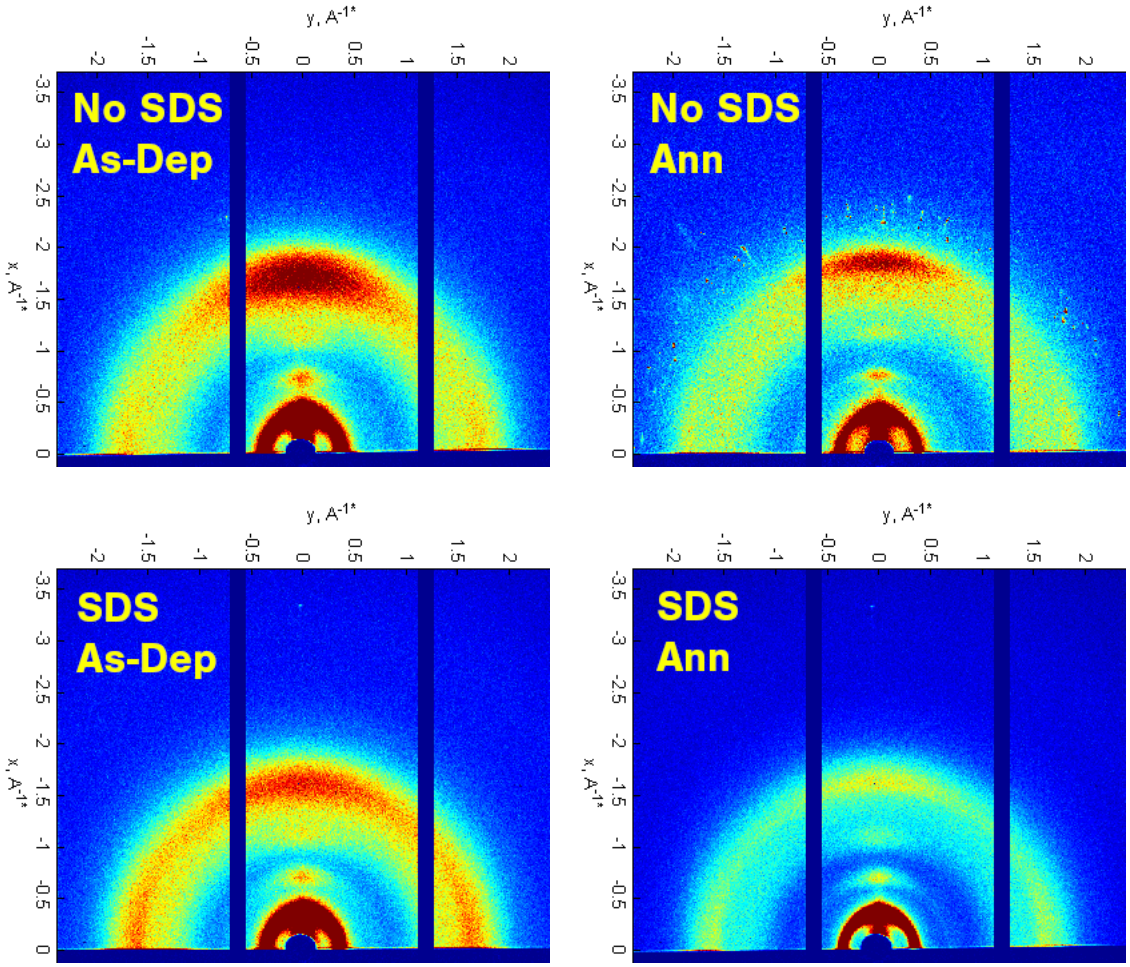

FIGURE 3.5: 2D GIWAXS images of P3HT films fabricated by RIR-MAPLE at 7 cm TS distance. Effects of SDS surfactant and thermal annealing at 140 °C for 30 minutes are shown.

was used to extract the peak parameters by fitting Gaussian curves to the data. The (010) peak is considered explicitly because it is expected to impact charge conduction more than the (100) peak. The trends in d-spacing and FWHM line width for the (010) peak can also be analyzed in terms of an ordered coherence length, or crystallite domain size, D, which is calculated by the Scherrer equation [54]:

$$D = \frac{0.9\lambda}{\Delta\theta \cos\theta_{peak}} \tag{3.1}$$

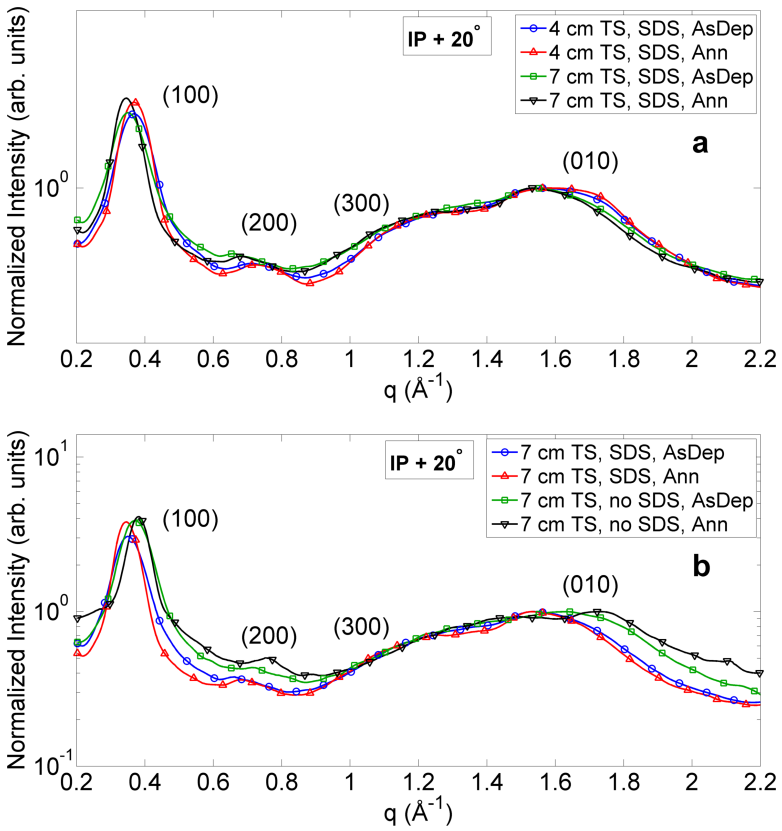

FIGURE 3.6: IP GIWAXS measurements of P3HT films integrated from IP angle +20° and normalized to the (010) peak. a) The effects of target-substrate distance and annealing are shown. b) The effects of surfactant added to the RIR-MAPLE emulsion and of annealing are shown.

where $\lambda = 1.540598$ Å is the wavelength of CuK$_\alpha$ x-ray radiation, $\Delta\theta$ is the FWHM of the peak in radians, and θ_{peak} is the value of the Bragg peak in radians. The ordered domain size, D, for the (010) peak represents an average interchain coherence length across regions with ordered polymer chains that are perpendicular to the polymer backbone axis, but do not include the conjugation length along the polymer backbone. This interchain coherence length represents the average breadth or spatial extent of an ordered region of multiple polymer chains. A larger interchain coherence length in a given direction should correlate with better crystallinity and higher hole mobility [55].

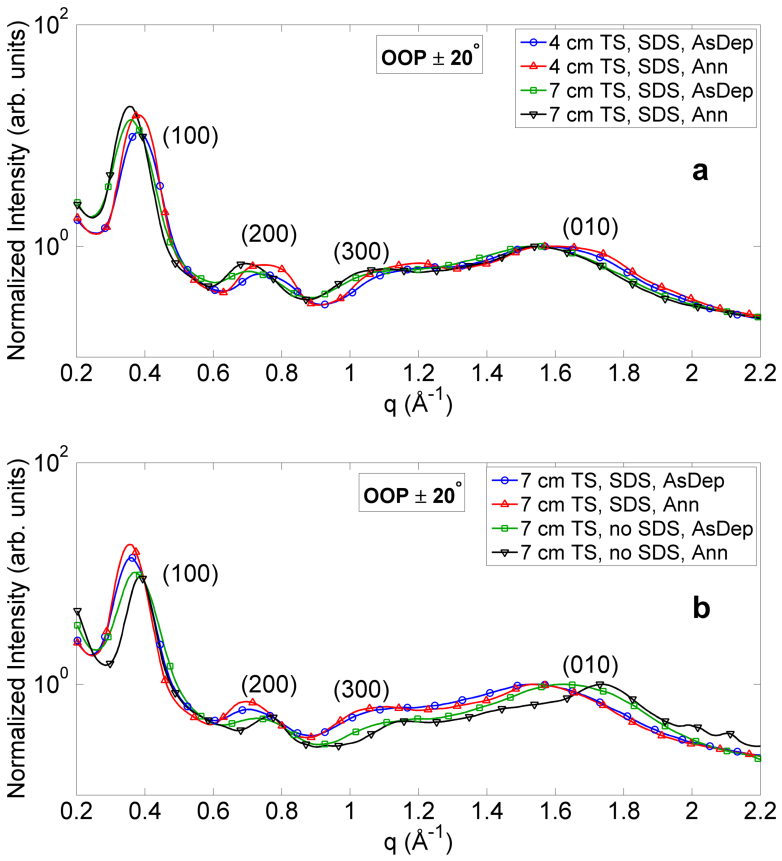

FIGURE 3.7: OOP GIWAXS measurements of P3HT films integrated from the vertical angle $\pm 20^{\circ}$ and normalized to the (010) peak. a) The effects of target-substrate distance and annealing are shown. b) The effects of surfactant added to the RIR-MAPLE emulsion and of annealing are shown.

Several trends can be observed from the data in Table 3.1. First, we look only at the in-plane data. It is clear that there is an order of magnitude larger ratio of π-stacked, (010)-axis polymers to side-chain-stacked, (100)-axis polymers in the solution-cast films relative to RIR-MAPLE films just by looking at the (010)/(100) amplitude ratio. Within the RIR-MAPLE sample set, the films containing SDS have a larger (010)/(100) amplitude ratio, indicating a larger quantity of π-stacked polymers to facilitate hole transport. However, those same films possess a larger d-spacing, indicating the presence of the surfactant molecules. The interchain coherence lengths of the RIR-MAPLE samples are slightly lower on average than the

Table 3.1: GIWAXS peak q and d values of RIR-MAPLE P3HT films. The values in this table summarize the data in Figure 3.6 and Figure 3.7.

Deposition Technique	IP/ OOP	TS Dist (cm)	Heat Treat-ment	SDS Status	(010)/ (100) Amp.	(010) q ($Å^{-1}$)	(010) FWHM ($Å^{-1}$)	(010) d-spacing (Å)	Interchain Coherence Length (Å)
RIR-MAPLE	IP	4	As-Dep	SDS	0.284	1.586	0.448	3.96	25.72
RIR-MAPLE	IP	4	Ann	SDS	0.237	1.603	0.430	3.92	26.81
RIR-MAPLE	IP	7	As-Dep	SDS	0.283	1.569	0.431	4.00	26.73
RIR-MAPLE	IP	7	Ann	SDS	0.214	1.567	0.394	4.01	29.24
RIR-MAPLE	IP	7	As-Dep	no SDS	0.197	1.654	0.436	3.80	27.08
RIR-MAPLE	IP	7	Ann	no SDS	0.127	1.758	0.302	3.57	69.32
Drop-cast	IP	-	Ann	-	2.615	1.658	0.357	3.79	32.38
Spin-cast	IP	-	Ann	-	2.255	1.632	0.413	3.85	27.93
RIR-MAPLE	OOP	4	As-Dep	SDS	0.075	1.577	0.461	3.98	24.98
RIR-MAPLE	OOP	4	Ann	SDS	0.050	1.604	0.441	3.92	26.17
RIR-MAPLE	OOP	7	As-Dep	SDS	0.059	1.537	0.492	4.09	23.42
RIR-MAPLE	OOP	7	Ann	SDS	0.042	1.558	0.406	4.03	28.38
RIR-MAPLE	OOP	7	As-Dep	no SDS	0.089	1.698	0.339	3.70	34.09
RIR-MAPLE	OOP	7	Ann	no SDS	0.044	1.746	0.150	3.60	76.98
Drop-cast	OOP	-	Ann	-	0.017	1.537	0.506	4.09	22.75
Spin-cast	OOP	-	Ann	-	0.015	1.539	0.546	4.08	21.08

solution-cast values, but are of comparable order.

Comparison of the out-of-plane data is equally interesting. The (010)/(100) trend has reversed: the RIR-MAPLE films have 3-6 times as many OOP (010)-oriented polymers as the solution-cast films do, relative to the OOP (100)-oriented polymers. The interchain coherence length of the (010)-oriented polymers is larger than in the solution-cast films, but still of the same order of magnitude. The SDS-inclusive RIR-MAPLE films still exhibit larger d-spacings than the films without SDS, consistent with the IP data.

Therefore, based on the d-spacing data in Table 3.1, the presence of surfactant in the P3HT thin films is observed, even with the minimal 1E-3 wt% of SDS. For the IP direction, the data show a weak correlation between the presence of surfactant and the (010)/(100) amplitude ratio (higher with surfactant). For the OOP direction, the

Table 3.2: IP to OOP (010)/(100) ratio, indicating the relative number of π-stacked, ordered polymer chains oriented IP versus the relative OOP quantity.

Deposition Technique	TS Dist. (cm)	Heat Treatment	SDS Status	**IP/OOP (010)/(100) Amplitude Ratio**
RIR-MAPLE	4	As-Dep	SDS	**3.79**
RIR-MAPLE	4	Ann	SDS	**4.74**
RIR-MAPLE	7	As-Dep	SDS	**4.80**
RIR-MAPLE	7	Ann	SDS	**5.10**
RIR-MAPLE	7	As-Dep	no SDS	**2.21**
RIR-MAPLE	7	Ann	no SDS	**2.89**
Drop-cast	-	Ann	-	**154**
Spin-cast	-	Ann	-	**150**

data show a weak correlation between the presence of surfactant and the interchain coherence length (smaller with surfactant).

Perhaps a more useful figure of merit is the ratio of the in-plane to out-of-plane relative quantity of ordered (010) polymer chains (i.e. relative to the quantity of (100)-oriented chains in the same direction). The data, presented in Table 3.2, clearly demonstrate that the RIR-MAPLE films are more isotropic in nature compared with the solution-cast films. The largest relative quantity of in-plane, (010)-ordered polymer chains in the RIR-MAPLE films is obtained for the slowly-deposited, 7-cm-TS distance P3HT films that included surfactant. The data from this GIWAXS analysis will be useful in comparison with the IP hole mobility measurements described in the next section.

3.3 Effect of Target Surfactant on P3HT Thin Film Mobility

Delocalization of the π-electrons along the P3HT conjugated backbone allows for charge transport in the (00l) direction, and the mobility is highest in this case [55], especially where the backbone conjugation is uninterrupted. Delocalized charge also exists among the overlapping π-orbitals in the (0k0) direction due to stacking of

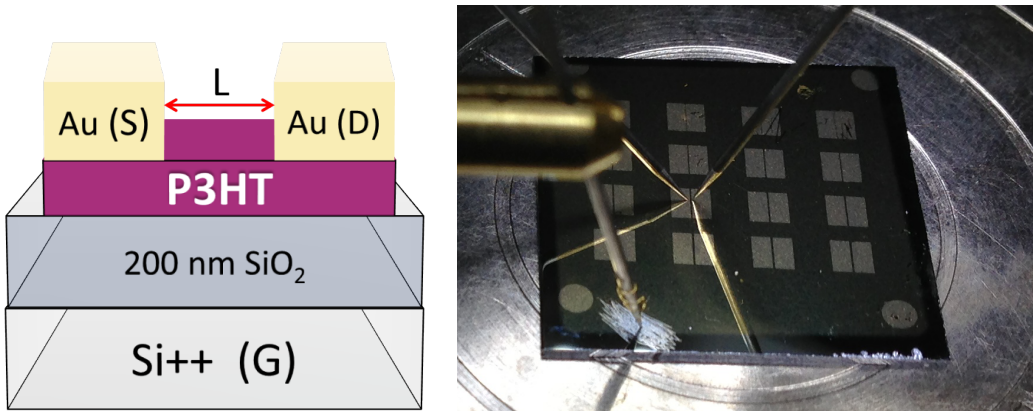

FIGURE 3.8: OFET device (l) schematic and (r) measurement of RIR-MAPLE-deposited P3HT films. The photo shows actual devices where each row represents a different channel length (top to bottom): 25 μm, 50 μm, 75 μm, and 100 μm. Each set of Au contacts represents the source and drain. The single contact in the lower part of the image is the gate contact.

thiophene backbones from adjacent polymer chains (π-stacking). Because transport requires additional energy to allow the charge to hop between adjacent conjugated backbones, the charge mobility in the (0k0) direction is lower than in the (00l) direction [55]. Charge mobility is lowest in the (h00) direction because the saturated aliphatic side chains, which are present to promote solubility, are insulating compared with the conjugated backbone. Therefore, the orientation of polymer chain stacking in a P3HT thin film is directly related to its performance in an optoelectronic device. The goal of this study was to explore charge transport in thin films of P3HT that were deposited by RIR-MAPLE in order to determine how it compares to typical spin-cast films and to determine the impact of the emulsion target surfactant.

In-plane hole mobility was determined by fabricating and characterizing OFETs. Devices were fabricated on heavily p-doped Si with 200 nm thermally grown oxide. The active material is P3HT deposited by RIR-MAPLE to a thickness of 20-40 nm. Top contacts were 45-50 nm of Au, thermally evaporated onto the P3HT film through a shadow mask at ORNL to yield four devices, each with one of the following channel

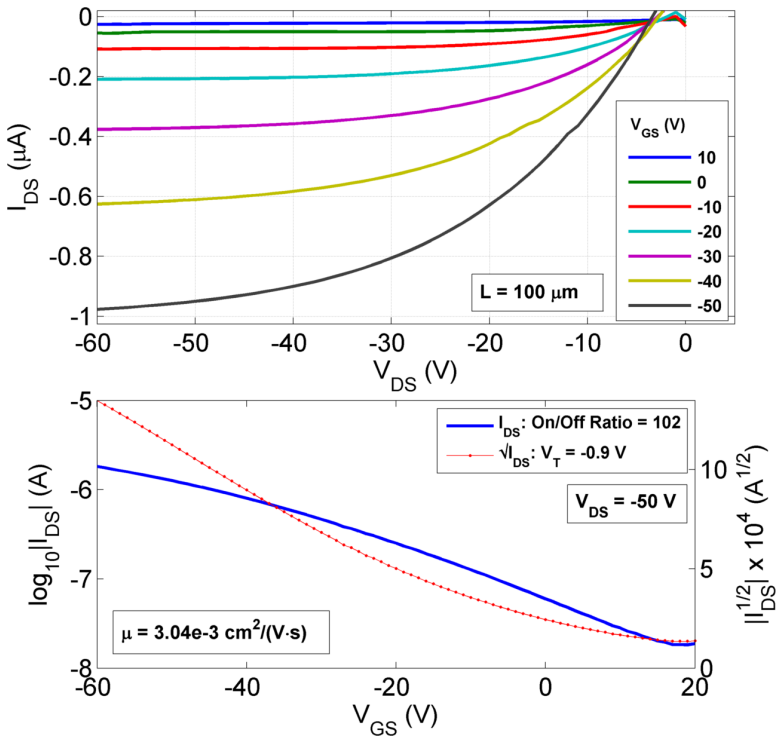

FIGURE 3.9: Output and transfer curves of the highest mobility RIR-MAPLE OFET as deposited: 7 cm TS distance; with SDS.

lengths: 25, 50, 75, or 100 μm (see Figure 3.8). All devices had a channel width of 2 mm. Devices were measured in atmosphere with a Keithley SCS 4200 probe station at ORNL, followed by annealing on a hot plate at 140 °C for 30 minutes in a nitrogen atmosphere glove box, then remeasured.

The OFET technique measures the IP drift mobility along the substrate/P3HT interface [56]. For transfer curve measurements, the drain-source voltage (V_{DS}) was held constant at -50 V, while the gate-source voltage (V_{GS}) was ramped from 20 V to -60 V. For output curve measurements, V_{GS} was stepped between 10 V and -50 V in increments of -10 V; for each V_{GS} value, the drain-source voltage was scanned from V_{DS} = 0 to V_{DS} = -60 V in 1 V increments.

The output and transfer curves for the highest mobility OFET deposited by RIR-MAPLE are shown in Figure 3.9 and Figure 3.10. By fitting a line to the linear region

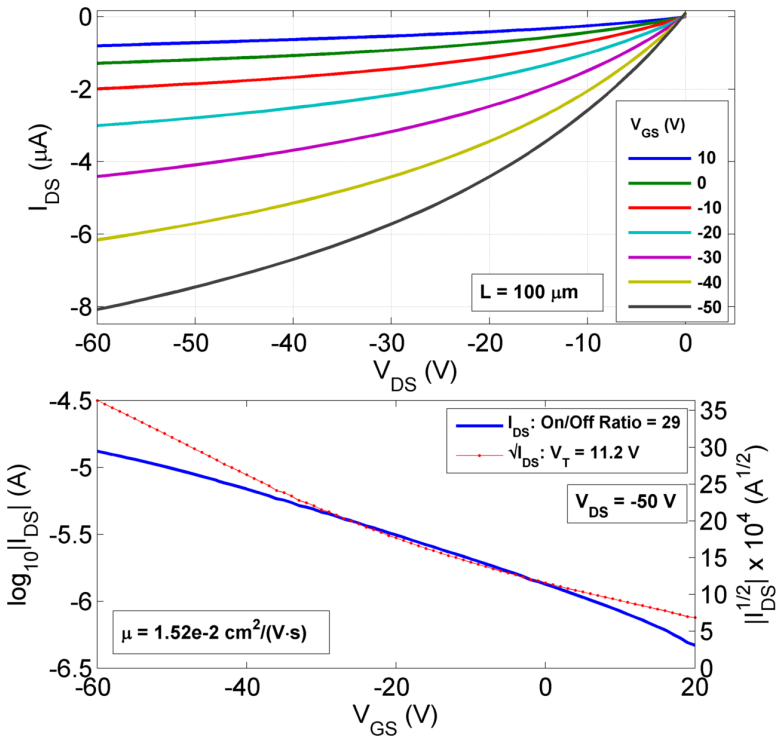

FIGURE 3.10: Output and transfer curves of the highest mobility RIR-MAPLE OFET after annealing at 140 C for 30 minutes in N^2 glove box: 7 cm TS distance; with SDS.

of the square root of the drain current in the transfer curve and interpolating back to zero current, the threshold voltage could be determined. During measurement of the transfer curves, VDS was held constant at -50 V, which is in the saturation regime and can be determined by inspection of the output plots. Therefore, the mobility of each film was calculated using the equation for the saturation regime [57]:

$$\mu = \frac{2L}{WC'_{ox}}\left(\frac{d\sqrt{I_D}}{dV_{GS}}\right)^2 \tag{3.2}$$

where L is the channel length, it W is the channel width (2 mm), V_{DS} is the source-drain voltage, and C'_{ox} is the oxide capacitance given by the ratio of the oxide dielectric constant, $\varepsilon_{ox} = \varepsilon_r\varepsilon_0 = 3.9\varepsilon_0$, to the oxide thickness, $t_{ox} = 200$ nm.

The highest RIR-MAPLE in-plane mobilities are shown in Figure 3.11 in com-

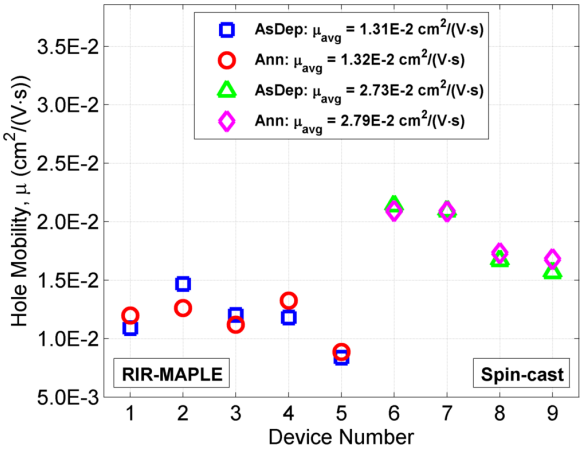

FIGURE 3.11: In-plane (IP) mobility comparison of 5 single RIR-MAPLE-deposited P3HT OFET devices with 4 single spin-cast devices exposed to similar environmental conditions.

parison with spin-cast devices that were prepared, stored, and tested in conditions identical to the RIR-MAPLE devices. Typical hole mobility values of solution-cast P3HT films reported in literature are on the order of 1E-1 cm^2/Vs for IP mobility [56]. The spin-cast films created for this study were exposed to the same environmental conditions as the RIR-MAPLE samples. In addition, the spin-cast devices were created in air, rather than inside a nitrogen-filled glove box where the oxygen and water content are more tightly controlled. The result is that the spin-cast films show a lower mobility of 2E-2 – 3E-2 cm^2/Vs. The highest mobilities were achieved with the RIR-MAPLE films deposited at the slowest rates (i.e. 7 cm TS distance) and contain 1E-3 wt% SDS surfactant in the DI water. The RIR-MAPLE films have a mobility range of 1E-4 – 1E-2 cm^2/Vs. Spin-cast devices do not require an emulsion for deposition, and therefore do not contain surfactant. The fact that the RIR-MAPLE devices exhibit mobilities within a factor of 2 of the spin-cast devices fabricated under identical conditions is evidence that the surfactant plays a minimal role in lateral charge transport at the P3HT/substrate interface. Additional gains in mobility may be possible by reducing exposure of the devices to atmosphere by

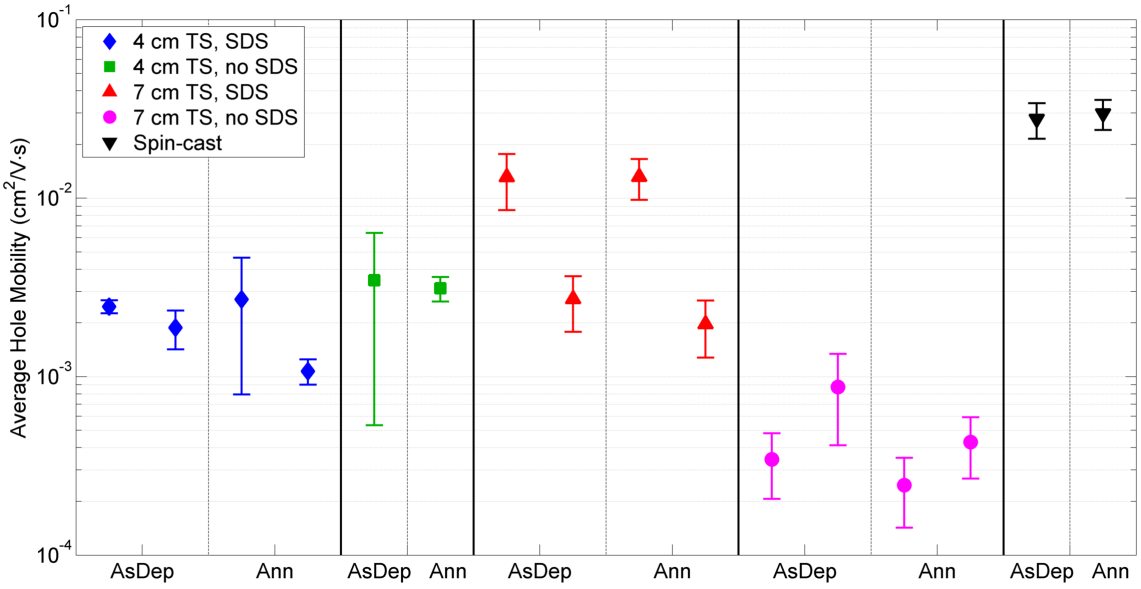

FIGURE 3.12: Summary of the hole mobilities calculated from RIR-MAPLE deposited OFET devices in comparison with spin-cast devices. The vertical bars indicated one standard deviation above and below the mean value after averaging the mobility values across all viable devices on a 16-device substrate.

attaching a glove box to the RIR-MAPLE chamber directly.

Figure 3.12 summarizes all mobility measurements across all different processing conditions. The data point is positioned at the mean value of all working devices measured, while the bars represent the standard deviation from the mean. Only one 4-cm-TS, no-SDS deposition contained working electrical devices. The poor film quality of the no-SDS devices contributed to this outcome. The 4 cm TS devices show consistency of mobility across all tested conditions. In contrast, the 7 cm TS devices are dramatically different with and without SDS. Additionally, annealing the devices proved to degrade them slightly. However, this effect may be due to exposure of the as-deposited devices to atmosphere during initial electrical testing. In any case, the data indicate that while SDS is incorporated into the P3HT thin films deposited by emulsion-based RIR-MAPLE, the presence of surfactant in the target leads to the highest in-plane hole mobilities for RIR-MAPLE deposited films

(which are only slightly below that of spin-cast films).

More interesting is the comparison of Table 3.2 with the relevant data in Figure 3.12. In order of highest to lowest mobility values, the deposition parameters are: spin-cast, 7 cm TS with SDS, 4 cm TS with SDS, and 7 cm TS without SDS. The corresponding relative quantity of in-plane (010)-oriented P3HT chains follows the same trend, indicating that they may play a role in the determination of in-plane mobility.

3.4 Effect of Target Surfactant on P3HT Thin Film Conjugation Length and Crystalline Aggregates

Additional insight into the film structure can be gained by analysis of the UV-visible absorbance data. Optical absorbance by P3HT has been extensively studied and modeled. Spano [47] studied the origin of the absorbance peaks using quantum chemistry calculations of the optically-mediated vibronic transitions between a ground state exciton and its first electrically excited state. The exciton is assumed to originate from the electronic and vibrational ground state, but is quantum-mechanically allowed to transition to any vibrational state in the first excited electronic state due to the broken symmetry presented by the partially ordered morphology of P3HT films. Another implicit assumption of this model is that a thin film of P3HT forms weakly-interacting H-aggregates whose optical absorbance could be explained by a modified Frank-Condon model [47]. H-aggregates can be described as polymer chains whose nearest neighbors are coupled through side-by-side interaction in contrast with J-aggregates in which polymer chains are electronically coupled end to end [58].

The Spano theory determines the contributions from the more-ordered aggregate regions in the P3HT relative to the higher energy single chain contributions in the amorphous regions. The crystalline aggregates can be modeled as a series of equal-width Gaussians, representing A_{00}-A_{1x} vibronic transitions, where x represents

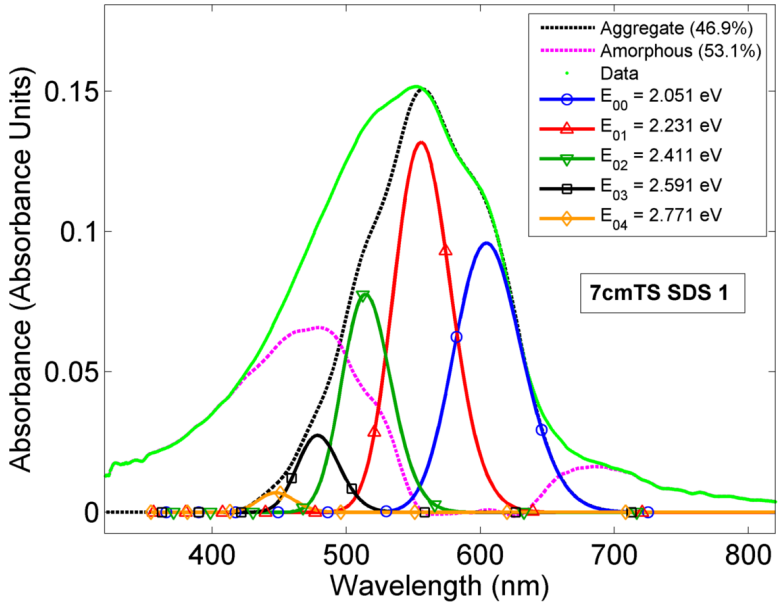

FIGURE 3.13: Spano absorbance analysis of RIR-MAPLE-deposited P3HT thin film with deposition parameters: 7 cm TS distance, with SDS, and device 1.

vibrational levels 0-4 in the first excited electronic state. A previous analysis of the applicability of the fit by Turner, et al. [59], has determined that the optimal fit region is λ = 551-643 nm (i.e. 1.93-2.25 eV) where only aggregates contribute to the absorbance spectrum. The equation that models the first five vibronic transitions of absorbance in the P3HT aggregate regions is given by [60]:

$$A(E) = C \sum_{m=0} \left(\frac{e^{-S} S^m}{m!} \right) \left(1 - \frac{W e^{-S}}{2E_p} \sum_{n \neq m} \frac{S^n}{n!(n-m)!} \right)^2 \times \frac{exp\left(-\frac{(E - E_{00} - mE_p - 0.5WS^m e^{-S})^2}{2\sigma^2} \right)}{\sigma\sqrt{2\pi}} \quad (3.3)$$

where C is a proportionality constant; m and n are different vibrational energy levels; E is the photon energy; E_p is the phonon energy separating the vibrational levels, which is taken to be dominated by the C=C ring breathing mode at 0.18 eV [61]; E_{00} is the electronic transition energy from the vibration-less electronic ground state

Table 3.3: Spano absorbance parameters extracted from nonlinear, least-squares fit to UV-visible absorbance data of P3HT thin films deposited by RIR-MAPLE.

P3HT Film	4 cm TS distance				7 cm TS distance			
	SDS		No SDS		SDS		No SDS	
	1	2	1	2	1	2	1	2
FWHM, σ (meV)	84.5	84.5	90.1	88.3	85.1	85.3	90.3	90.8
Excitonic Bandwidth, W (meV)	188	189	188	175	185	186	193	192
Estimated % Aggregates	47.9	46.9	53.3	47.8	46.9	48.9	46.8	46.3

to the vibration-less first electronic excited state; W is the excitonic bandwidth; σ is the full-width half-maximum (FWHM) of each transitional Gaussian; and, it S is the Huang-Rhys factor, taken to be 1 [62]. A nonlinear least-squares fit is applied via MATLAB to the 1.93-2.25 eV region. By holding the FWHM constant across all Gaussians, the first five vibronic absorbance transitions can be mapped as shown for example in Figure 3.13.

The FWHM (σ) and excitonic bandwidth (W) fit values are shown in Table 3.3. The excitonic bandwidth is inversely proportional to the conjugation length of the polymer chains, such that a lower value indicates fewer conformational defects along a polymer backbone and more order in general [61]. Clark et al., determined from absorption spectra of P3HT in solution that the relative increase in oscillator strength of the polymer chains that transition from disordered or amorphous orientations to a more-ordered aggregate-like orientation is 39±10% [61]. This figure can be used to estimate the fraction of the film composed of aggregates, as tabulated in Table 3.3 for the same RIR-MAPLE samples described in the previous section. An estimate of the aggregate contribution to the absorbance can be computed by first integrating under the total aggregate curve. The amorphous contribution is determined by subtracting the aggregate contribution from the total spectrum and integrating the remainder.

The amorphous contribution is then multiplied by 139% (±10%) to account for the oscillator strength differences. The aggregate percent then can be estimated by the ratio of the aggregate area to the sum of the aggregate and scaled amorphous areas.

Several observations can be made about the data in Table 3.3. The first observation is that the films fabricated with SDS surfactant have narrower FWHM values, indicating better internal ordering of the polymer chains [63]. Second, the excitonic bandwidth is inversely proportional to the interchain coherence length, an average unbroken conjugation length along the polymer backbone, which improves charge transport. Except for the second SDS sample, the 4 cm TS distance devices have almost identical interchain coherence lengths, which is consistent with the mobility data falling in the same range of values. The SDS samples of the 7 cm TS distance devices have longer intrachain coherence lengths (i.e. average conjugation lengths) compared with the no-SDS devices, which also is consistent with the SDS devices exhibiting larger mobilities. Moreover, the exciton bandwidths are inversely proportional to the mobility outcomes. That is, the lowest-to-highest excitonic bandwidths correlate to the highest-to-lowest intrachain coherence lengths, which in turn are proportional to the mobility outcomes. Finally, the estimated aggregate percentages across all films are of the same order (again, except for one fast-deposition, no-SDS device). This result indicates that although the films all contain roughly the same amount of crystalline/ordered regions of polymer, the packing and orientation of those separate crystalline regions along the P3HT/substrate interface plays a role in charge transport through those regions. By observing the surface structure of the films via AFM, additional explanation of the electrical behavior can be obtained.

Table 3.4: Deposition parameters for thin RIR-MAPLE films of P3HT. Sample number is indicated by #1 or #2.

		No SDS #1	**No SDS #2**	**SDS #1**	**SDS #2**
4 cm Target-Substrate	Thickness (nm)	28.4	18.8	40.0	31.4
	Roughness, R_q (nm)	24.3	14.1	28.3	20.6
	Deposition Rate (nm/min)	0.299	0.209	0.615	0.698
7 cm Target-Substrate	Thickness (nm)	13.6	20.7	24.2	27.0
	Roughness, R_q (nm)	30.5	21.2	25.8	21.8
	Deposition Rate (nm/min)	0.209	0.207	0.372	0.415

3.5 Effect of Target Surfactant on P3HT Thin Film Surface Morphology

A poorly-mixed RIR-MAPLE target ablates more unevenly due to spatial variations in the local absorption coefficient, which also affects the composition of the ejected material. In the case of SDS omission, the RIR-MAPLE target tends to separate into a mixture of oil and water domains during the freezing process. While more strongly absorbing regions will ablate a shallower region of the target in which the majority of the solvent evaporates prior to deposition, more weakly absorbing regions contain larger absorption depths that eject thicker volumes of material that are removed primarily by stress-fracturing the material beneath the surface [18]. A consequence of this mechanism is that the solvents are not completely vaporized prior to substrate deposition because of the lower power density of the laser pulse that is spatially spread over a larger volume. Therefore, a spatially homogeneous RIR-MAPLE target that has a large absorption coefficient at the laser wavelength is crucial to good quality films, requiring a surfactant in the emulsion target.

In order to determine the extent to which the presence of surfactant in the emulsion target impacts P3HT thin films, the surface morphology of films with and without surfactant were characterized by AFM. AFM measurements of two different

depositions for each set of parameters are outlined in Table 3.4. It is clear that the surfactant creates a well-mixed target as indicated by the higher average deposition rates. However, at these thicknesses, the surface roughness of each film is of the same order of thickness as the film itself. Thickness profiles (not shown) of the films generated by AFM nonetheless demonstrate that there is a contiguous film at these thicknesses. In general, it has also been observed that as the overall thickness of the film increases, the ratio of the surface roughness to the thickness tends to decrease. So these films represent the worst case scenario of roughness relative to thickness. Indeed, 10 nm is an approximate thickness lower limit that still allows contiguous films to be achieved.

The planar AFM images in Figure 3.14 and Figure 3.15 echo the data in the table and add additional insight. The non-SDS films are uneven and show circular features indicative of liquid droplets hitting the surface of the substrate, consistent with large target absorption depths that lead to stress fracturing of the target surface [18]. In addition, there are large particles of solid material due to the larger oil and water domains in the target, attributable to the omitted surfactant. The films fabricated with SDS, while still rough, exhibit a more spatially homogeneous profile across the film. Large particles are almost non-existent, and there is no evidence of liquid droplets, indicating a shallow absorption depth in the RIR-MAPLE target, which implies smaller oil and water domains within the frozen target. The surface morphology of the slowly deposited films (i.e. 7 cm TS distance) of Figure 3.15 follows the same trends as that of the fast deposition films. Therefore, it is clear that the poor surface quality of the surfactant-less films contributes to the poorer and more erratic electrical and optical behavior observed.

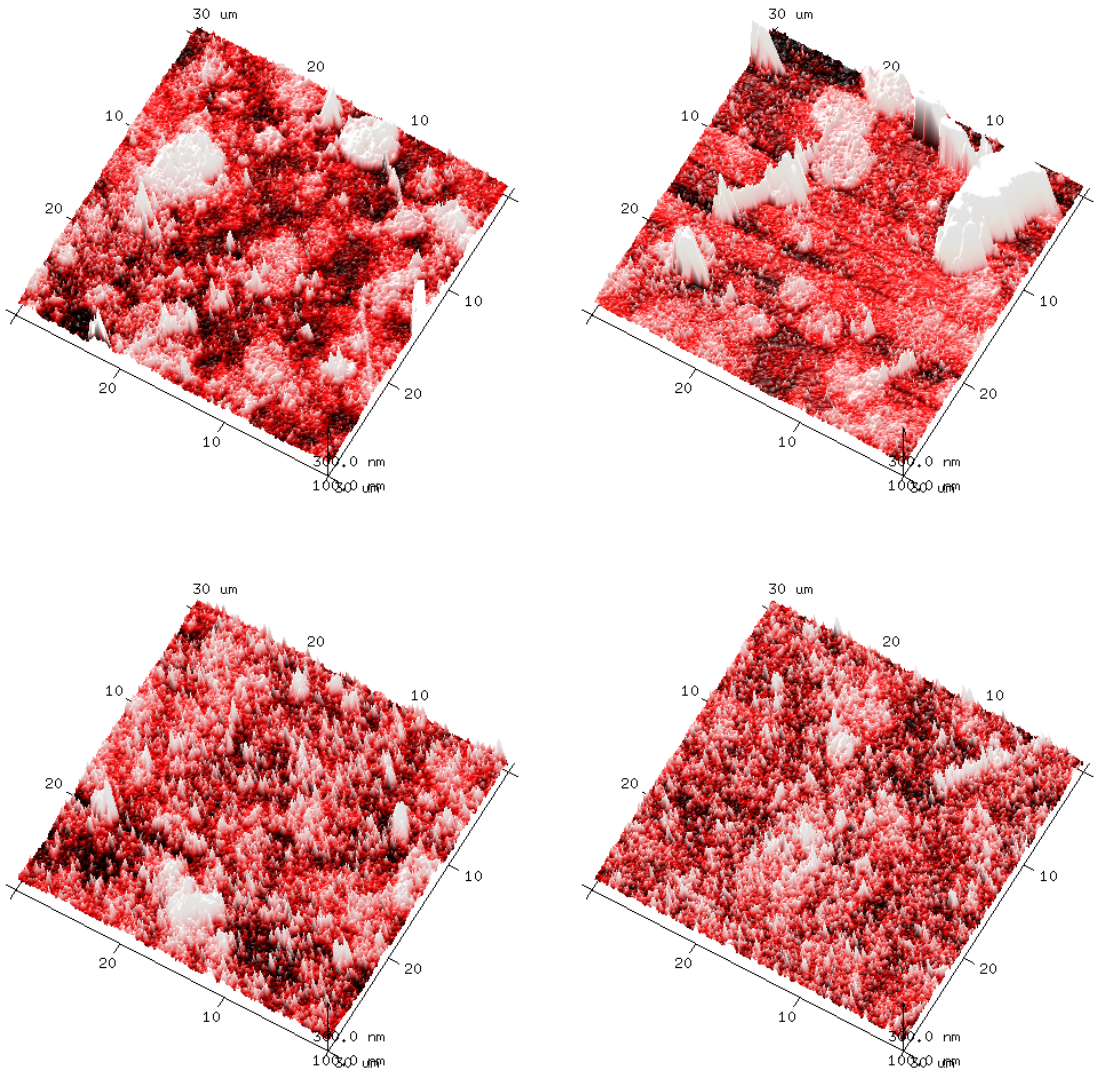

FIGURE 3.14: AFM measurements of thin P3HT films deposited at fast deposition rate (4 cm TS distance) showing the effect of the absence or presence of SDS surfactant. The top row shows 2 different constant-parameter depositions without SDS. The bottom row shows 2 different constant-parameter depositions with SDS.

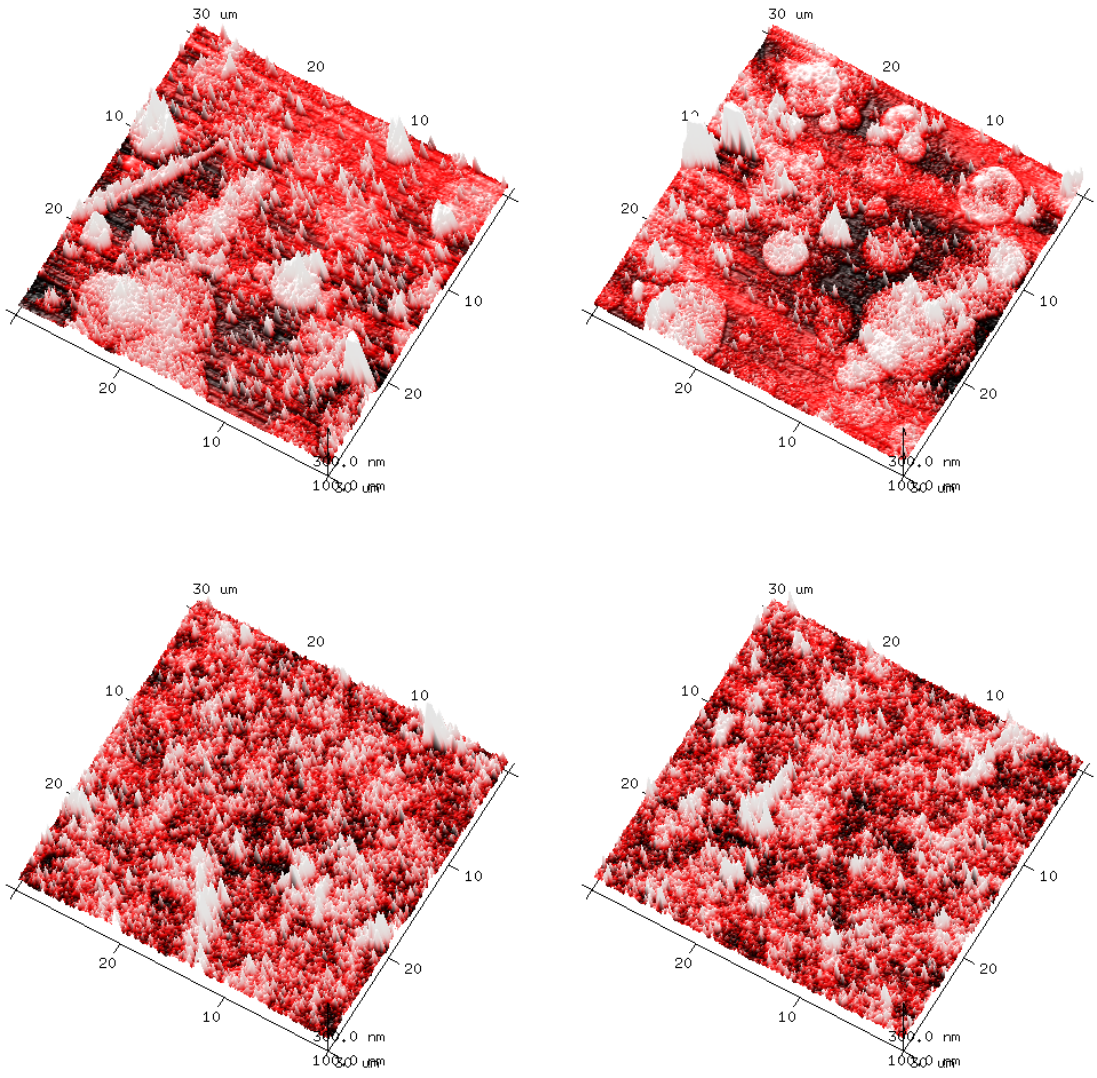

FIGURE 3.15: AFM measurements of thin P3HT films deposited at slow deposition rate (7 cm TS distance) showing the effect of the absence or presence of SDS surfactant. The top row shows 2 different constant-parameter depositions without SDS. The bottom row shows 2 different constant-parameter depositions with SDS.

3.6 Conclusions

This chapter demonstrated the effects of the surfactant, SDS, on P3HT thin films deposited by emulsion-based RIR-MAPLE. The surfactant required to produce the emulsified target for the RIR-MAPLE process presents competing features. The surfactant is required to minimize the oil and water domains within the emulsion to reduce the absorption depth of the frozen target, which leads to more efficient ablation of the host matrix material and smoother, more contiguous thin films. The surfactant also may contribute to a reduction of electrical or optoelectronic performance due to its insulating nature. However, mobility data determined that IP mobility is minimally affected by the demonstration of an RIR-MAPLE OFET with IP mobility similar to a spin-cast device.

Initially, SDS was discovered in RIR-MAPLE films by XRD analysis. Further study indicated that 1E-3 wt% SDS in DI water would provide a stable enough emulsion to flash freeze in the target cup without separating into large oil and water domains, but was also invisible to detection by XRD as ordered structures. GIWAXS analysis determined that the relative ratio of IP, π-stacked to side-chain-stacked polymer chains to the identical OOP ratio predicted the relative mobilities measured by OFET devices. These ratios were determined by calculating the ratio of the relevant peak amplitudes from the 1D GIWAXS integrations. A study of the UV-visible absorbance that applied the Spano theory provided additional evidence of larger crystallite domain sizes via FWHM as well as longer intrachain coherence lengths (i.e. longer unbroken conjugated segments along the polymer backbone) via the exciton bandwidth values for films produced with surfactant. The intrachain coherence lengths also trended with the mobility values. Finally, AFM images indicated the poor overall quality of the film surfaces when surfactant is omitted, which supports the poor performance, in general, of such devices.

4

Gradient Refractive Index Anti-Reflection Optical Coatings Deposited by RIR-MAPLE

Most anti-reflection (AR) coatings, used in applications such as flat screen displays, solar cells, or eyeglasses [64], are produced for glass substrates by physical or chemical vapor deposition of metal oxides or metal fluorides. However, when deposited on flexible organic substrates, such as plastics, these inorganic AR coatings experience cracking and delamination because of the mismatch between the coefficients of thermal expansion (CTE) for the AR coating and the plastic substrate. Therefore, polymeric AR coatings with materials properties that are compatible with organic, flexible substrates are required for current and emerging technologies, such as flexible flat panel displays [65] and plastic lens eyeglasses [66].

While quarter- and half-wave plates can reduce reflection at specific wavelengths, gradient refractive index (GRIN) coatings are desirable because they offer AR properties across a broad spectral band and for a wide range of incident angles. A truly broadband, omnidirectional, and polymeric AR coating would be ideal, but such a film is challenging because it requires grading the refractive index (RI) from that of

the organic substrate (e.g. polycarbonate with n = 1.5-1.6) to that of the surrounding medium (usually air with n = 1.0).

The first roadblock to overcoming this challenge to a polymeric GRIN film is that bulk polymers cannot achieve RI values significantly below the theoretically determined limit of n = 1.29 [67]. However, low RI polymeric materials can be achieved as an optical effective medium, that is, by incorporating a low index component into a higher index polymer matrix. For example, nanocomposites of metal nanoparticles within a polymer matrix can lower the RI to less than 1.0 through the visible range [68]. Air can also be incorporated as a low index component via porous films [44]. In fact, networks of porous polymers constitute an attractive option for low RI films due to their simplicity: a blend of two polymers is deposited onto a substrate, after which one component (porogen) is chemically dissolved, leaving a three-dimensional network of polymer and air pores. The constituent domain sizes of the polymer blend are critical, in this case, because they determine the light scattering characteristics of the overall film.

Solution-cast polymeric porous films have been reported as organic, gradient refractive index (GRIN), AR coatings; yet, the gradient structure actually consists of several, discrete stacked layers of single refractive index as opposed to a GRIN profile [44]. Similarly, layered nanocomposites of a polymer and oxide nanoparticles have been demonstrated by RIR-MAPLE to reduce the reflectance of a flexible substrate through the visible region [69]. Both demonstrations highlight a significant challenge to realizing a GRIN profile in polymeric films, that is, the required capability to continuously vary the RI over a given film thickness. For example, moth eye nanostructures that feature tapered polymer nanopillars have demonstrated GRIN profiles because the air content increases with decreasing nanopillar diameter from base to tip [70]. Furthermore, layering of solution-cast films is difficult because of the inevitable dissolution of existing layers by repeated deposition of polymers with

similar solubility.

While porous polymer films with a true gradient material structure are nearly impossible to create with solution-casting methods, this section will demonstrate that RIR-MAPLE can enable these structures for application to GRIN AR coatings. In contrast, emulsion-based resonant infrared matrix-assisted pulsed laser evaporation (RIR-MAPLE) is an organic thin film deposition technique (variation of pulsed laser deposition) that is capable of creating a polymeric, optical effective medium with a specific RI due to nanoscale domains [71] within the polymer blend. Therefore, this chapter demonstrates emulsion-based RIR-MAPLE as a technique to enable porous polymer networks with a specified RI that is designed using effective medium theory and is lower than those of the constituent materials in the polymer blend. Importantly, using emulsion-based RIR-MAPLE to achieve a polymeric, optical effective medium is the first step towards realizing a truly broadband, omnidirectional, AR coating appropriate for plastic substrates by enabling a polymeric GRIN profile.

In this chapter, details are presented of the application of RIR-MAPLE thin-film deposition to polymer blends comprising the homopolymers polystyrene (PS) and poly(methyl methacrylate) (PMMA), or block co-polymers of both, for use as optical anti-reflection (AR) coatings. In contrast to solution-based deposition, it will be shown that emulsion-based RIR-MAPLE demonstrates the versatility required for the fabrication of complex structures. Porous films with a gradient refractive index (GRIN) profile resulting from three dimensional control over the film morphology, namely control over polymer blend domain sizes and the ability to continuously vary polymer blend ratios over a given film thickness, will be demonstrated.

4.1 RIR-MAPLE Thin Film Growth and Characterization

The polymers were each dissolved in toluene, and then mixed with benzyl alcohol and water to create an emulsion. Each emulsion was flash frozen at -196 °C in the

pre-cooled target cup of the RIR-MAPLE system. A pulsed Er:YAG laser (λ= 2.94 μm) provided a 2-Hz, 1.46 J/cm^2 pulse train (90 μs) that deposited the polymer onto the substrate. All films were deposited on silicon substrates to facilitate characterization via spectroscopic ellipsometry (SE), atomic force microscopy (AFM), scanning electron microscopy (SEM) and reflectivity measurements. All depositions were 5 hours long, the silicon substrate was positioned 5 cm from the target, and the substrate temperature was held constant at 20 °C. All films were deposited on silicon substrates to facilitate basic materials characterization via spectroscopic ellipsometry (SE), atomic force microscopy (AFM), scanning electron microscopy (SEM) and reflectivity measurements. For the GRIN AR prototypes, polycarbonate substrates were used. After deposition of the blended PS:PMMA films, the PS component was cross-linked and the PMMA component was degraded by exposing the film under vacuum to UV light, followed by washing the glacial acetic acid. After this processing, the remaining film is a nanoporous, three-dimensional (3D), PS polymer network.

The degree of mixing, domain size, and porosity are important materials properties because the resulting RI of the films requires that the final coating be an optical effective medium. Optimization of the film thickness and surface roughness are also critical to achieving high quality GRIN AR coatings. The structural characterization of the polymer blend thin films, especially determination of the nanoscale domain size and porosity, was conducted using TEM, AFM, and scanning electron microscopy (SEM). Film thickness and root-mean-squared (RMS) surface roughness were determined by AFM imaging and surface profilometry. In addition, AFM phase images were analyzed to observe the blended film morphology after PMMA decomposition. Optical characterization of bare Si (or polycarbonate) substrates and porous PS films deposited on Si (or polycarbonate) are conducted using spectroscopic ellipsometry (SE) and reflectivity measurements with an integrating sphere.

4.2 Nanoscale Phase Domains in Homopolymer Blends

In order to fabricate a polymeric, porous coating that behaves as an optical effective medium, it is critical to co-deposit a polymer blend (AR polymer and porogen polymer) with isotropic nanoscale phase domains that are significantly less than the wavelength of incident light. A rule of thumb for an optical effective medium is that the domains must be ten times smaller than the wavelength of interest (<40 nm for the visible range). When this domain size condition is satisfied, light scattering is avoided and the light wave experiences the heterogeneous medium, effectively, as a homogeneous medium with material properties that are a mixture of the constituent materials. As long as the pore sizes remain below this threshold, small variations in the distribution of pore sizes should have little effect on the refractive index. Therefore, various studies were performed to determine the domain sizes in blended films of PS and PMMA deposited by sequential RIR-MAPLE deposition.

First, in order to observe the nanoscale domain size of as-grown PS:PMMA blended homopolymer films, a staining procedure was used for TEM imaging to provide contrast between the stained PS and the unstained PMMA. The PS component of a PS:PMMA (1:1) blend can be selectively stained by RuO_4 vapor (film exposure to RuO_4 vapor for 90 minutes) and viewed by TEM to determine the degree to which the two polymers mix [72]. The TEM image in Figure 4.1 shows that RIR-MAPLE produces nanoscale PS domains of less than 100 nanometers.

Second, the impact of post-growth annealing on the domain size of PS:PMMA polymer blends was investigated. The goal was to determine the extent to which annealing would allow limited polymer chain mobility to reduce the surface roughness of the films while maintaining the smallest single-phase polymer domains possible and avoiding macroscale separation of the dissimilar homopolymers. For this study, four sets of three samples were grown to test the variation in anti-reflection performance

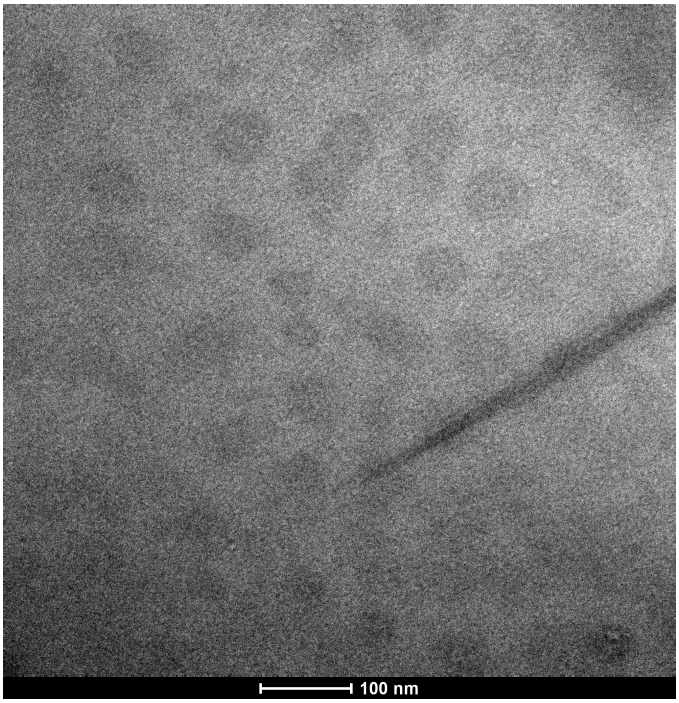

FIGURE 4.1: TEM image of RIR-MAPLE grown PS:PMMA 1:1 film that has been exposed to RuO_4 vapor for 90 minutes. The PS component absorbs the vapor and is stained; the PMMA is unaffected. PS domains are less than 100 nm.

with thermal annealing. Each set included one of three polymer ratios of PS:PMMA by weight: 1:3, 1:1, and 3:1. Both the PS and PMMA were purchased from Sigma-Aldrich and used as received. The PS has a weight-averaged molecular weight of M_w = 350,000 g/mol and a glass transition temperature of T_g = 95 °C. The PMMA has M_w = 350,000 g/mol and T_g = 105 °C. The heat treatment was varied as follows: as-grown at 20 °C, annealed at 100 °C, annealed at 120 °C, and annealed at 140 °C. All anneals took place under vacuum for 30 minutes. The anneal temperatures were chosen relative to the glass transition temperatures of the polymers. By annealing at 100 °C, the PS was above its T_g, but the PMMA was below its T_g. The anneals at 120 °C and 140 °C were chosen to be above the T_g of both polymers, but at some point above T_g, the polymer domains begin to agglomerate into larger sized domains.

Table 4.1 compiles a metric of the surface roughness of the films grown for this

Table 4.1: The RMS surface roughness, R_q, normalized by the film thickness for the three PS:PMMA polymer ratios both before and after a 3 minute glacial acetic acid wash. In general, the roughness increases after the acid wash due to the formation of pores left by the PMMA component removal.

	Before Acetic Acid Wash				After Acetic Acid Wash			
PS:PMMA Polymer Ratio	As-Grown	100 °C	120 °C	140 °C	As-Grown	100 °C	120 °C	140 °C
1:3	0.18	0.14	0.12	0.08	0.33	0.39	0.39	0.39
1:1	0.11	0.12	0.04	0.06	0.18	0.28	0.13	0.33
3:1	0.14	0.13	0.10	0.26	0.11	0.30	0.19	0.25

study. The films range in thickness from 45 to 150 nm, but Table 4.1 shows the RMS surface roughness, R_q, that has been normalized by the thickness so that a direct comparison can be made between films. It would be difficult to compare absolute R_q values because different proportions of otherwise identical-thickness films are removed with the acetic acid wash, depending on the initial polymer ratio. Before the acetic acid wash, the roughness represents 11-18% of the as-grown films. Annealing for 30 minutes at 100 °C, which is between the glass transition temperatures of the two polymers, improves the roughness somewhat. Annealing for 30 minutes at 120 and 140 °C reduces the roughness to as low as 4% of the film thickness. Absolute values of the RMS roughness for films prior to the acetic acid wash range between 4 and 16 nm for films of 30-150 nm thickness. After the acetic acid wash, the films have decreased in thickness to a range of 24-88 nm and have an R_q range of 8-15 nm. In general, the roughness/thickness ratio has increased due both to the thinner films, but also to the increased porosity imparted to the films due to removal of the PMMA component.

Figures 4.2-4.5 show the AFM phase images of the PS:PMMA films grown by RIR-MAPLE that are as-grown, annealed at 100 °C, annealed at 120 °C, and annealed at 140 °C, respectively. All films were annealed for 30 minutes. Each figure depicts films that were grown with a PS:PMMA ratio of 1:3, 1:1, and 3:1, and all

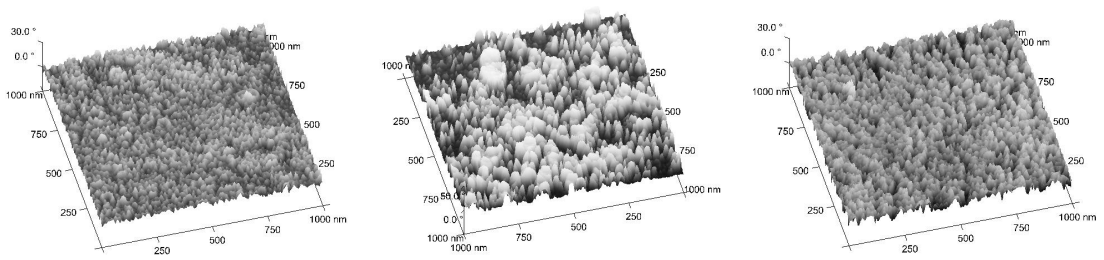

FIGURE 4.2: AFM phase images of as-grown PS:PMMA film after 3 minute acetic acid wash. Polymer ratios are (left) 1:3, (middle) 1:1, and (right) 3:1 PS:PMMA.

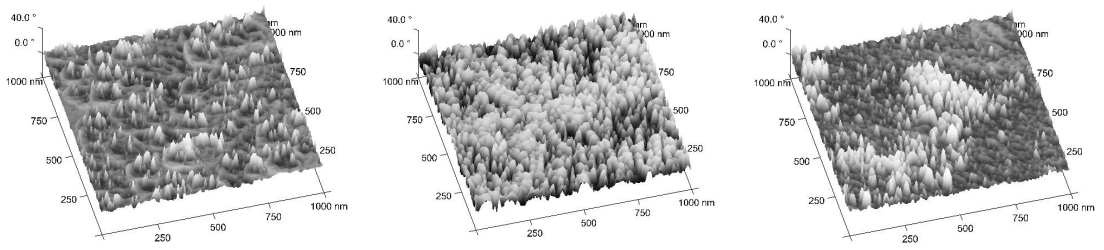

FIGURE 4.3: AFM phase images of PS:PMMA films after annealing at 100 °C and then a 3 minute acetic acid wash. Polymer ratios are (left) 1:3, (middle) 1:1, and (right) 3:1 PS:PMMA.

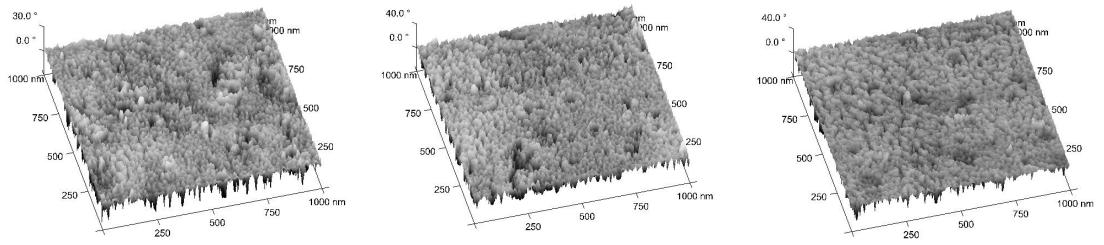

FIGURE 4.4: AFM phase images of PS:PMMA films after annealing at 120 °C and then a 3 minute acetic acid wash. Polymer ratios are (left) 1:3, (middle) 1:1, and (right) 3:1 PS:PMMA.

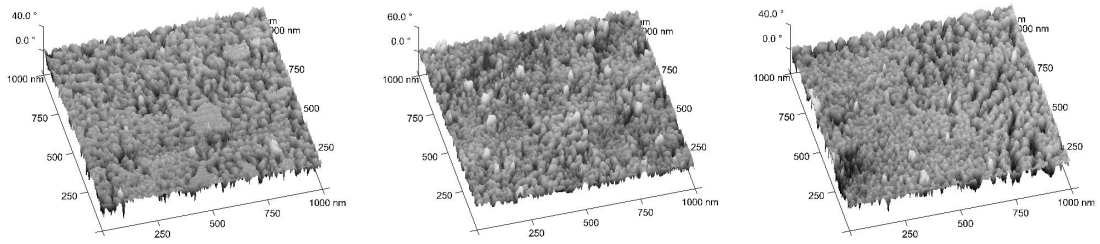

FIGURE 4.5: AFM phase images of PS:PMMA films after annealing at 140 °C and then a 3 minute acetic acid wash. Polymer ratios are (left) 1:3, (middle) 1:1, and (right) 3:1 PS:PMMA.

films have had the PMMA component removed by washing in acetic acid for 3 minutes each. The phase image, rather than the height image, was shown to provide higher resolution of the materials. Additionally, it has been shown that the AFM phase image is proportional to the Youngs modulus of the material imaged [73]. Therefore, a distinction can be made between the PS in the lighter regions and the silicon substrate in the darker regions. All images depict a 1 μm^2 area of the film.

First, it is important to note that for the as-grown samples, for all PS:PMMA blend ratios, the domain sizes of the remaining PS are in the nanoscale (<100 nm). Second, it is important to evaluate more closely the impact of annealing temperature on the domain size. After the acetic acid wash, the center image of Figure 4.2 shows that the remaining PS domains exist in a range of size scales. Figure 4.3, center, shows an overall smoothing of the film when annealed at 100 °C for 30 minutes, but the domains after the wash are still heterogeneous in size. At 100 °C, the film is above the PS glass transition temperature of 95 °C, but below that of PMMA (T_g = 105 °C). It is possible that the PS reorganized itself around the fixed PMMA, leading to the varied domain sizes. When the temperature is raised above the T_g of both PS and PMMA, the domain size of the remaining PS after the acetic acid wash is small and the distribution is relatively homogeneous as shown in Figure 4.4. Raising the anneal temperature to 140 °C yields PS domains that have started to

increase in size. This effect is more obvious in Figure 4.5, left, which depicts the 1:3 PS:PMMA films, where there are large domains in the center of the image.

Thus, this annealing study of blended PS:PMMA homopolymer films deposited by sequential RIR-MAPLE demonstrated that the annealing temperature has little impact on the normalized surface roughness after PMMA removal, but it does impact the domain sizes of the remaining PS homopolymer. The effect of a given annealing temperature seems to depend on its relation to the glass transition temperature of the constituent materials. In this particular study, the optimal temperature for a 30 minute anneal is 120 °C, which is above the glass transition temperatures of both PS and PMMA, but not high enough that the nanoscale domains begin to agglomerate into larger microscale domains. This study is important not only because it verifies that the nanoscale domains are observed in as-grown, blended RIR-MAPLE films, but because it indicates a possible technique for tuning the domain size in such films.

While the annealing study characterizes the PS domains after the acetic acid wash has removed the PMMA porogen, for application to GRIN AR coatings, the remaining PS must be cross-linked by exposure to UV light in order to prevent collapse of the three-dimensional porous scaffold Therefore, we next present evidence of the nanoscale domain sizes in porous PS films after they were UV-crosslinked and washed with glacial acetic acid. For this work, three ratios by volume of PS:PMMA were chosen: 3:1, 1:1, and 1:3, corresponding to 25%, 50%, and 75% porous films, respectively. SEM images of the films were collected to characterize the nanoscale domain sizes.

SEM images of the as-deposited films prior to PMMA removal were collected to demonstrate lack of porosity. Figure 4.6 shows SEM images at two different magnifications of an RIR-MAPLE-deposited blended 1:1 PS:PMMA film prior to removal of the PMMA layer with acetic acid. The films become featureless as magnification is increased. SEM images of the film surfaces for the porous PS films on Si are shown

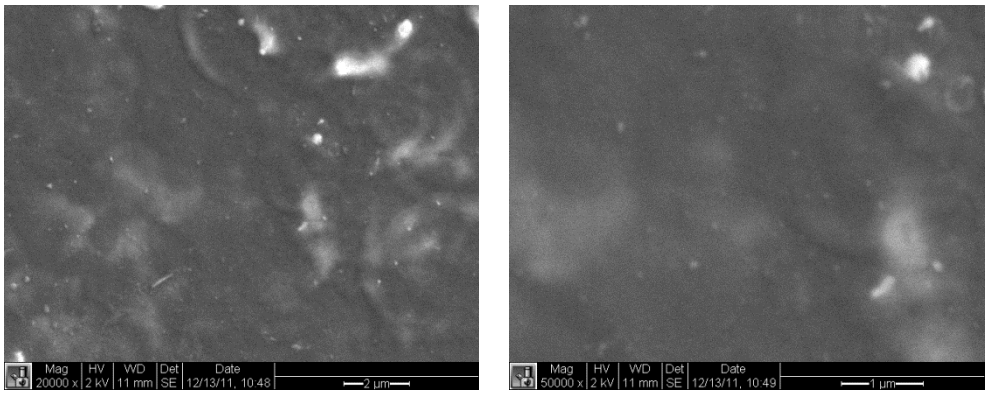

FIGURE 4.6: SEM images of as-deposited blended PS:PMMA 1:1 v/v films deposited by RIR-MAPLE show no evidence of porosity prior to removal of the PMMA component via acetic acid.

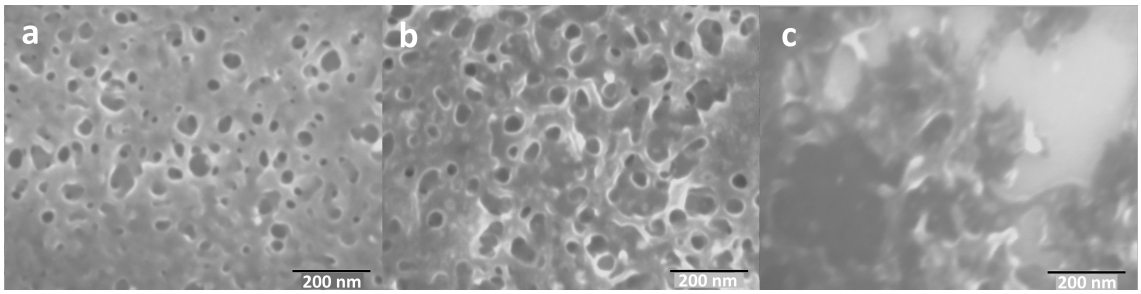

FIGURE 4.7: SEM images of porous polystyrene films: (a) 25% porosity, (b) 50% porosity, (c) 75% porosity.

in Figure 4.7. At magnification equal to that of Figure 4.7, the SEM images in Figure 4.6 show nonporous surfaces, but the films also begin to charge due electron bombardment.

The SEM images for the 25%, 50%, and 75% porosity films, shown in Figures 4.7a, b, and c, respectively, clearly demonstrate that the porosity increases as the PMMA content increases in the blended homopolymer films deposited by RIR-MAPLE. The 75% porous film of Figure 4.7c has so little PS remaining after PMMA removal that pore collapse at the surface is evident. Nevertheless, the pores closer to the substrate are most likely intact, as demonstrated by the optical characterization of the porous

films. It is evident in the SEM images that the average pore size is of the order of 50 nm, satisfying the effective medium criterion that the pore size must be of the order of 10% or less of the incident wavelength. Therefore, these porous films meet the effective medium requirements for the majority of the visible spectrum.

Thus, RIR-MAPLE has been demonstrated to effectively co-deposit PS and PMMA homopolymers, producing nanometer-scale mixing of the components that is ideal for organic anti-reflective optical coatings.

4.3 Optical Effective Media Using Homopolymer Blends

Bruggemans effective medium theory [74], shown in Equation 4.1, is used to determine the correct volume ratio between PS and PMMA that yields a desired effective RI after the PMMA component is dissolved:

$$f\frac{n_a^2 - n^2}{n_a^2 + 2n^2} + (1-f)\frac{n_{ps}^2 - n^2}{n_{ps}^2 + 2n^2} = 0 \tag{4.1}$$

where f is the volume fraction of air pores; $(1-f)$ is the volume fraction of the PS network; n_a is the RI of air (1.0), n_{ps} is the RI of PS (n_{ps} = 1.590 at λ= 600 nm), and n is the effective RI of the porous film. Using the Bruggeman formula (Equation 4.1), the three PS:PMMA volume ratios under investigation (3:1, 1:1, and 1:3) correspond to nominal porosities (i.e. volume fractions of air) of 25%, 50%, and 75%, respectively. As an example, the corresponding calculated effective RI values at 600 nm are 1.402, 1.306, and 1.166, respectively.

For those samples with UV cross-linking (shown in Figure 4.7), the measured optical properties are compared to calculated optical properties in order to confirm that emulsion-based RIR-MAPLE achieves the desired RI values by the deposition of an optical effective medium with nanoscale domain sizes. The calculated reflectivity assumes homogeneous media; therefore, experimental deviation from the theoretical

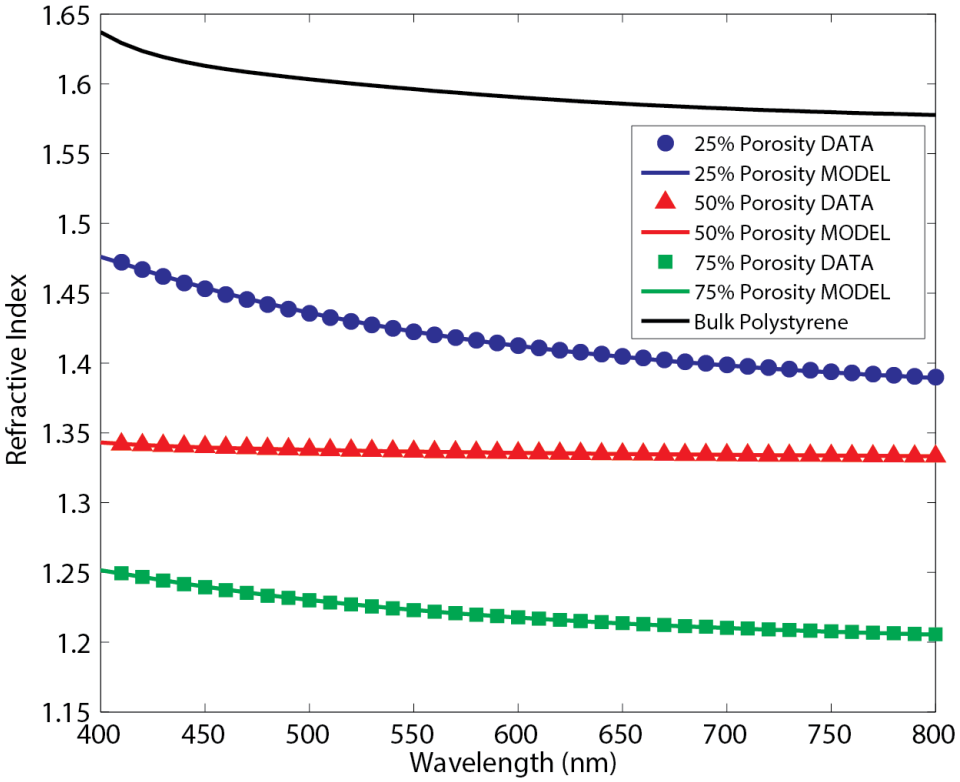

FIGURE 4.8: Refractive index spectra of porous polystyrene films as measured by spectroscopic ellipsometry. Experimental data points are shown relative to bulk polystyrene (black line); Sellmeier fits to the experimental RI data are represented as solid lines. Fitting coefficients are given in the supplemental materials.

reflectivity spectrum should be indicative of the extent to which the porous films deviate from an effective medium. Importantly, these studies demonstrate that RIR-MAPLE enables porous films with tailored RI using only homopolymers.

The RI values of the porous PS films, measured by spectroscopic ellipsometry (400-800nm), are shown using data points in Figure 4.8 (25% porosity - circles, 50% porosity - triangles, and 75% porosity - squares). The measured bulk polystyrene RI spectrum [75] is also shown as a reference. For each porosity, the RI value as a function of incident light wavelength, λ, is calculated using the Sellmeier equation,

Table 4.2: Dispersive RI Sellmeier coefficients of porous PS films. The C_i values represent UV absorption peaks of bulk PS. The B_i values are determined by a least squares fit to the measured RI data (400-800 nm).

Porosity	B_1	B_2	B_3	C_1 (nm^2)	C_2 (nm^2)	C_3 (nm^2)
25%	-3.793	5.730	-1.083	194^2	215^2	264^2
50%	4.916	-4.721	0.573	194^2	215^2	264^2
75%	-1.623	2.535	-0.495	194^2	215^2	264^2

Equation 4.2, for comparison to the measured RI values [76]:

$$n(\lambda)^2 = 1 + \sum_i \frac{B_i \lambda^2}{\lambda^2 - C_i} \tag{4.2}$$

where the Sellmeier coefficients B_i and C_i are fitting parameters. The C_i values are determined by the absorption spectrum of the material (bulk PS) and correspond with ultraviolet absorption peaks (194 nm, 215 nm, and 264 nm, respectively) [77]. A nonlinear, least-squares fitting routine is used to determine the B_i values from the measured RI. The coefficient of determination parameter, R^2, which approaches a value of one when the fit perfectly matches the data, was calculated for all three sample porosities. In this case, R^2 is approximately unity when fitting the Sellmeier equation to the experimental data. The theoretical RI Sellmeier coefficients that result from fitting the measured RI are shown in Table 4.2.

The theoretical RI dispersion curves are represented by the solid lines in Figure 4.8. The expected trend is observed in the RI data: as the porosity increases, the RI decreases as more air is introduced into the film composition. The RI values calculated using Bruggeman effective medium theory at 600 nm are 1.402, 1.306, and 1.166, for 25%, 50%, and 75% porosities, respectively; and, the experimental values are 1.413, 1.336, and 1.218, respectively. The increasing disparity between the predicted and experimental values with increasing porosity implies an increasing amount of pore collapse as the amount of solid material is decreased in the 3D

network and the structural stability is decreased.

The issue of pore collapse is also explored by comparing the measured and calculated reflectivity spectrum for each sample with different porosity (using the bare silicon substrate as a reference). At normal incidence to the film, the condition under which reflectivity measurements were made, the reflectivity is given by a simple Fresnel transfer matrix approach for a single homogeneous film on a homogeneous substrate, surrounded by air:

$$R(\lambda, n, d, \theta = 0^\circ) =$$

$$\frac{n^2\left(n_a - n_{ps}\right)^2\left[\cos\left(\frac{2\pi}{\lambda}nd\right)\right]^2 + \left(n_a n_{ps} - n^2\right)^2\left[\sin\left(\frac{2\pi}{\lambda}nd\right)\right]^2}{n^2\left(n_a + n_{ps}\right)^2\left[\cos\left(\frac{2\pi}{\lambda}nd\right)\right]^2 + \left(n_a n_{ps} + n^2\right)^2\left[\sin\left(\frac{2\pi}{\lambda}nd\right)\right]^2} \tag{4.3}$$

where λrepresents the wavelength of the incident light, d is the film thickness, θ is the light incidence angle relative to the substrate normal, and n_a, n_{ps}, and n, are the dispersive RI values of air, polystyrene, and the porous film, respectively.

The reflectivity is very sensitive to film thickness and incident light wavelength, as demonstrated in Figure 4.9a and b, in which the reflectivity for a 50% porous PS film is calculated as a function of d and λ, respectively. The RI value for n used to calculate the reflectivity is that measured by spectroscopic ellipsometry for the PS film with 50% porosity. In Figure 4.9a, the calculated reflectivity is plotted as a function of film thickness for three different incident wavelengths (400 nm, 600 nm, 800 nm); while in Figure 4.9b, the calculated reflectivity is plotted as a function of incident wavelength for three different film thicknesses (50 nm, 100 nm, 150 nm). These plots demonstrate that an intuitive trend of reflectivity vs. porosity cannot be determined directly because of the variations that occur due to incident wavelength or film thickness. Rather, the reflectivity data is analyzed by determining the quality of the fit between the measured and calculated reflectivity for each specific sample.

As seen in Equation 4.3, the RI dispersion of the porous films, $n(\lambda)$, and the

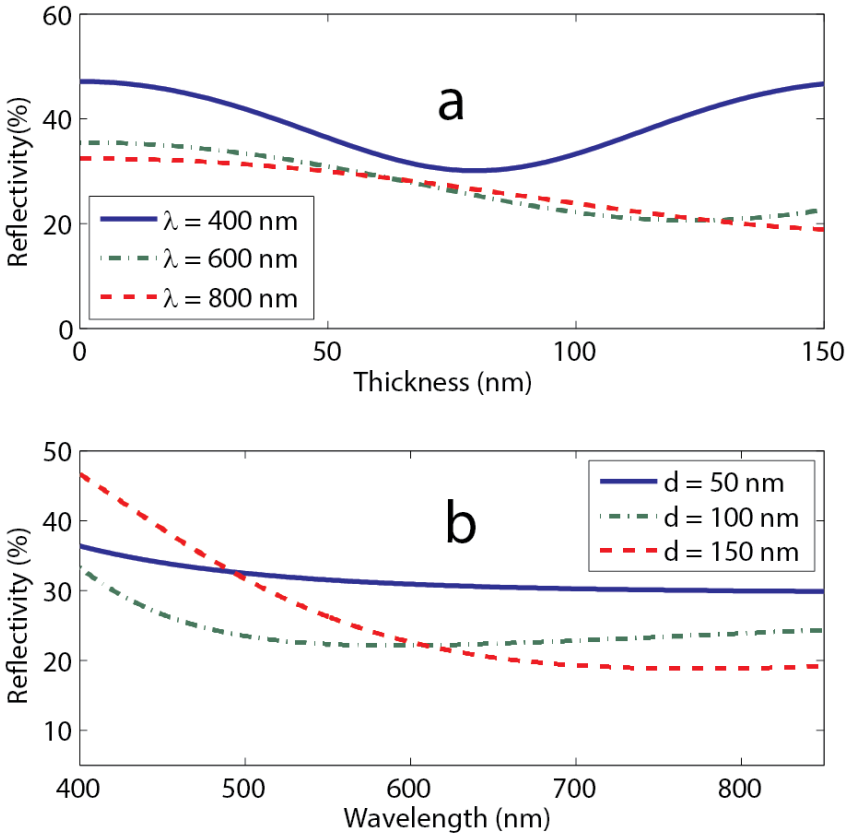

FIGURE 4.9: Calculated reflectivity spectra of porous polystyrene thin films (50% porosity by volume). (a) Film thickness effects for three different incident wavelengths (400 nm, 600 nm, 800 nm). (b) Spectral effects for three film thicknesses (50 nm, 100 nm, and 150 nm).

film thickness, d, are the two primary experimental parameters that determine the calculated reflectivity. Therefore, two possible approaches are pursued in order to compare the measured and calculated reflectivity spectra for the porous films: 1) Method A: let d equal the measured film thickness (by AFM or profilometer) and determine $n(\lambda)$ by fitting the measured and calculated reflectivity; or 2) Method B: let $n(\lambda)$ equal the measured RI dispersion (by spectroscopic ellipsometry) and determine d by fitting the measured and calculated reflectivity. A nonlinear least

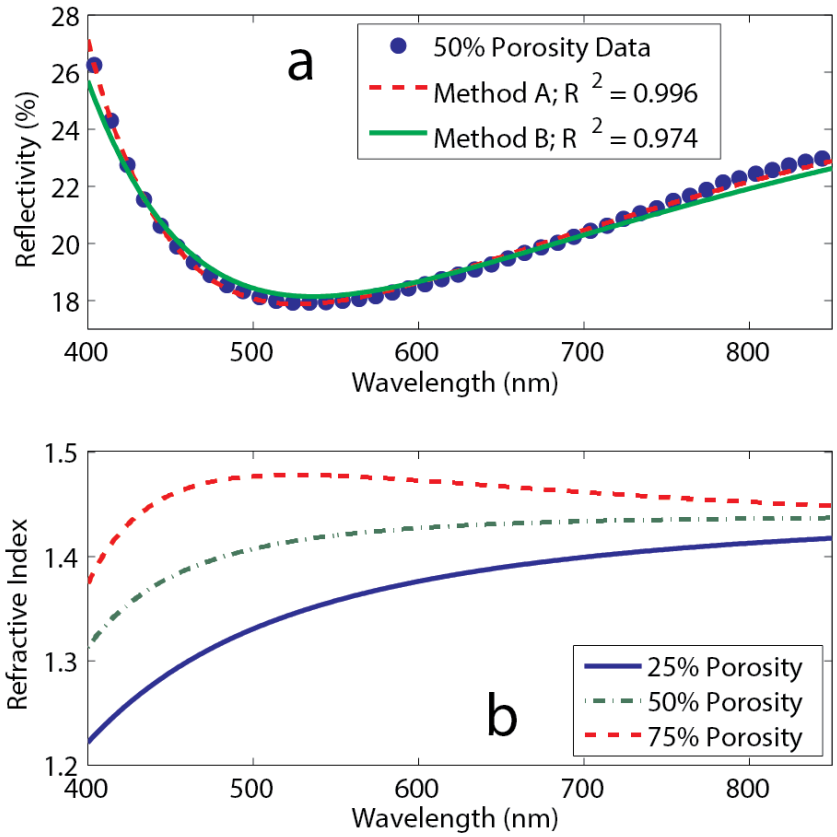

FIGURE 4.10: (a) Comparison of measured and fit (Methods A and B) reflectivity spectra for 50% porous polystyrene film. The red curve represents Method A, which results in an RI spectrum with anomalous dispersion that is non-physical (see Figure 4b). The green curve represents Method B, which is the true physical representation of the film. (b) Non-physical refractive index spectra that resulting from fitting the measured reflectivity using Method A. The corresponding porosities trend in the wrong direction with respect to the RI value. Also, the RI shape demonstrates anomalous dispersion, yet normal dispersion is observed in the measured ellipsometry data.

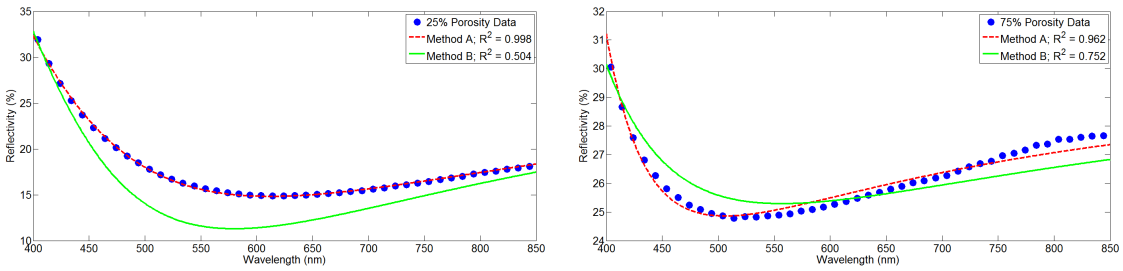

FIGURE 4.11: Comparison of measured and fit (Methods A and B) reflectivity spectra for 25% (left) and 75% (right) porous polystyrene films. Method A is non-physical. Method B is the true physical representation of the film.

squares fitting routine is used in each case. Figure 4.10a shows examples of the two approaches to fitting the measured and calculated reflectivity spectra for the 50% porosity film.

Figure 4.11 shows the measured and calculated spectra for the 25% and 75% porosity films. The blue circles represent the measured reflectivity data, the red curve represents the calculated reflectivity spectrum for Method A, and the green curve represents the calculated reflectivity spectrum for Method B. For the red curve, the R^2 value that indicates the goodness of the fit is approximately unity, but the RI that results from fitting the measured and calculated reflectivity spectra, shown as the blue curve in Figure 4.10b, is not physical. In fact, Figure 4.10b demonstrates that the RI dispersion, $n(\lambda)$, determined by Method A is non-physical for each film porosity due to the anomalous dispersion that is not observed in the measured ellipsometry data. Additionally, the RI values trend in the wrong direction for the given porosities; for example, the 75% film porosity should yield the lowest RI and the 25% film porosity should yield the highest RI. However, by using Method B, some insight into the film integrity can be achieved.

Figure 4.12 shows the measured reflectivity (data points) compared to the calculated reflectivity determined using Method B (solid lines) for each sample porosity. It

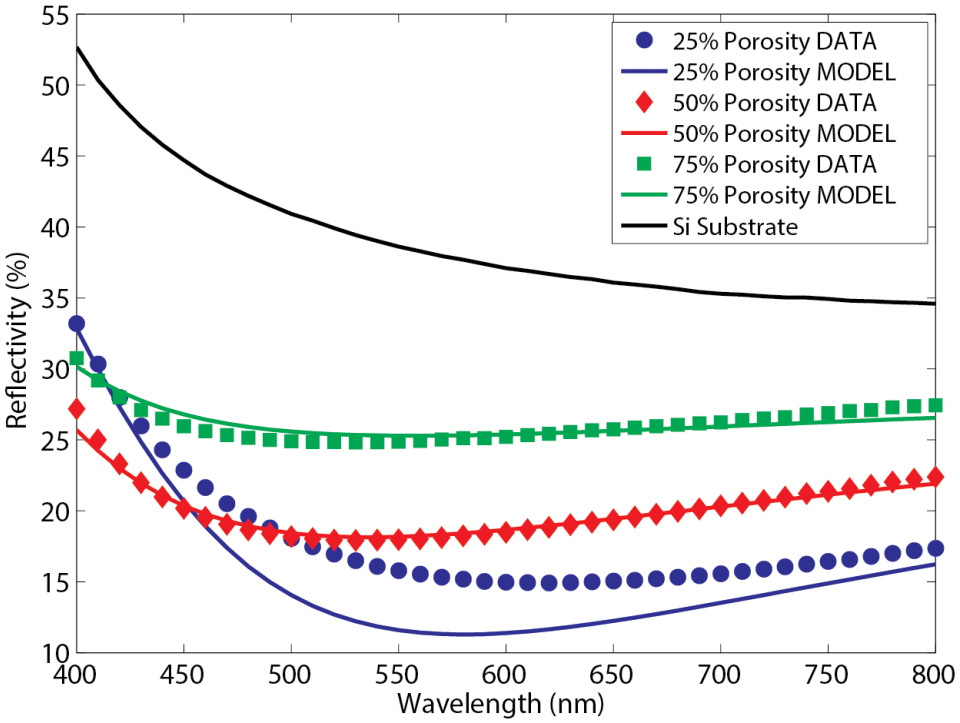

FIGURE 4.12: Measured reflectivity spectra (using integrating sphere) of the RIR-MAPLE-deposited porous polystyrene films (i.e. after PMMA removal). Markers depict experimental data relative to the Si substrate (black line); solid lines represent the Fresnel transfer matrix model fit to the measured data using Method B.

is apparent that all samples reduce the reflected light relative to the substrate alone, and that the calculated reflectivity shows a reasonable fit to the measured reflectivity data. To be specific, the reflectivity of the bare silicon substrate at 600 nm is 37.2%, and this measured value reduces to 15.0%, 18.5%, and 25.2%, for the PS films with 25%, 50%, and 75% porosity, respectively. However, as cautioned in the discussion of Figure 4.9, this reflectivity trend with porosity at a single wavelength cannot be generalized because the film thicknesses vary for each sample.

This issue is explored further by comparing the measured and fit film thicknesses determined using Method B for each film porosity. For the 25%, 50%, and 75% porosity films, the average film thickness was measured to be 89 nm, 69 nm, and 46 nm, respectively, while the thickness determined by fitting the reflectivity is 97.4

nm, 82.5 nm, and 79.8 nm, respectively. The R^2 values are 0.504, 0.974, and 0.752 for the fits to the 25%, 50% and 75% porosity films, respectively. As the nominal porosity increases, the measured and the fit values of the film thickness diverge, with a 25% porous film having only 8 nm difference, while the 75% porous film has a 34 nm span that indicates more severe pore collapse. As another check of the measured data, Bruggemans effective medium theory (Equation 4.1) is used to determine the effective porosity that accounts for the observed pore collapse. Analytical expressions for the dispersive RI values of air and polystyrene were calculated from the Sellmeier equation based on independent RI data of air and polystyrene [78]. These analytical expressions were used in conjunction with Equation 4.1 to fit the measured RI of the porous films, and the effective porosity (i.e. volume fraction of air) is extracted as a fitting parameter. The results demonstrate that the effective porosities follow the same general trend as the targeted porosity: namely, 28.8%, 41.8%, and 60.9% calculated porosities for the 25%, 50%, and 75% nominal porosities, respectively. In addition, these effective porosity values provide a measure of the integrity of the pore structure. As the porosity increases, or as the corresponding RI decreases, the reduction of the effective porosity compared to the corresponding targeted value indicates an increase in the occurrence of pore collapse, a trend mirrored by the difference between the measured and fit film thicknesses.

Thus far, we have demonstrated that RIR-MAPLE has the capability to co-deposit PS and PMMA homopolymers with nanoscale pores suitable for visible light wavelengths to experience the porous regions as effective media. The refractive index of the effective medium can be controlled by tailoring the porosity of the film by controlling only the ratio of the two materials during deposition. In the next section, results are presented of gradient refractive index films fabricated by RIR-MAPLE.

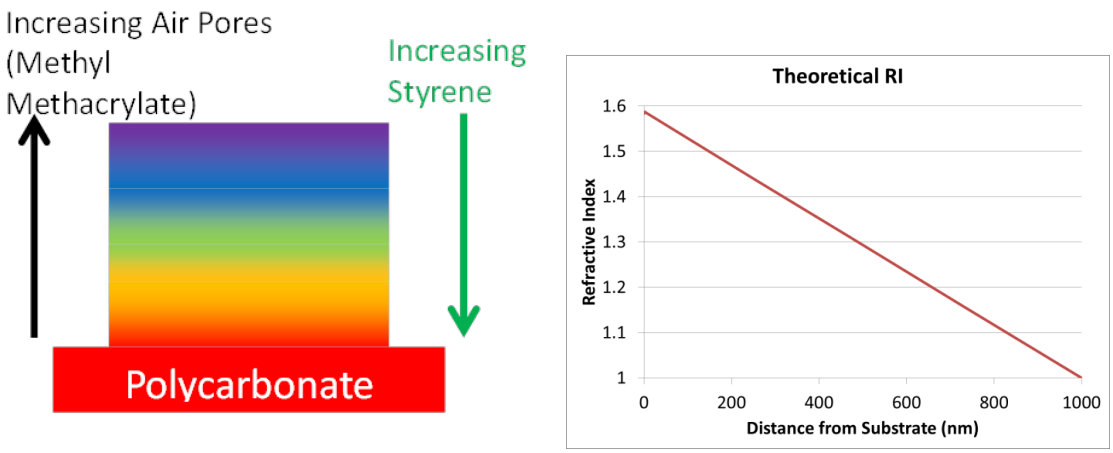

FIGURE 4.13: (left) Schematic of the gradient RIR-MAPLE film; (right) Linear distribution of the refractive index that results from grading the PS:PMMA ratio.

4.4 Gradient Refractive Index Anti-Reflection Coating

A schematic of the gradient device is shown in Figure 4.13. The RIR-MAPLE film contains polystyrene content that begins at 100% at the polycarbonate substrate. PMMA is then mixed in to the PS in a volume ratio that results in a linear refractive index distribution from the PC substrate to the film surface. Unlike the previous sections, where homopolymers were primarily employed, these designs incorporated block copolymers, PS-b-PMMA, where the block sizes were varied in the same ratio as the homopolymers, namely, 3:1, 1:1, and 1:3. Therefore, the final films were created by four different target configurations: PS homopolymer and PS-b-PMMA 3:1, PS-b-PMMA 3:1 and PS-b-PMMA 1:1, PS-b-PMMA 1:1 and PS-b-PMMA 1:3, and PS-b-PMMA 1:3 and PMMA homopolymer. The copolymers are included in the GRIN AR coating to help prevent the partial collapse of the porous films. By adding copolymers, the UV cross-linking should be more effective at structurally holding the films together after dissolution of the porogen PMMA.

Fresnel theory of reflections at optical interfaces determines the practical requirements of the GRIN film. It is important to note that the calculations assume the

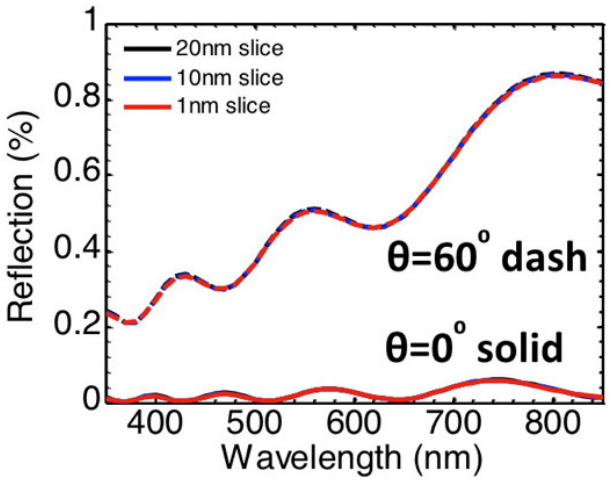

FIGURE 4.14: Fresnel theory calculations of reflectance of a 1 μm thick film with a linearly graded refractive index between a polycarbonate substrate (n = 1.58) and air (n = 1.00). Calculations are included for normal incidence (0°) and 60° relative to normal for three different thicknesses of constant RI slices.

refractive index across the visible region has an extinction coefficient of zero. A simple linear RI profile (Figure 4.13) over a 1 μm thick film gives the predicted reflectance in Figure 4.14 for normal incidence ($\theta = 0°$) and for light incident at 60° from normal incidence, both less than 1%. If the 1 μm thick film is composed of slices that are each of constant RI, the theory predicts identical behavior for slice thicknesses of 1, 10, and 20 nm each, as shown in Figure 4.14. This insensitivity to discretization of the GRIN profile is important because preliminary work with PS/PMMA blend films indicated that 10 nm is the minimum film thickness of a PS:PMMA blend that can be deposited with RIR-MAPLE with continuous spatial coverage on the substrate. For film thicknesses less than 10 nm, AFM analysis proved that the film was discontinuous across the substrate.

The minimum film thickness that RIR-MAPLE can deposit results from the fact that the process is inherently quantized and statistical. The quantization comes from the finite amount of material that is deposited by each laser pulse. Moreover,

the spatial distribution of the material from each pulse is not uniform across the substrate. Therefore the statistical nature of the process ensures full coverage of the substrate after some minimal average thickness is deposited on the substrate. The process is statistical because both the target and substrate are actively rotated during deposition to guarantee that the plume of material ejected by each laser pulse will result in a different spatial configuration of material that is deposited on a new orientation of the substrate. Additionally, the laser is rastered across the spinning target so that the plume of material originates from a slightly different location at each laser pulse.

Because of this requirement to discretize the GRIN profile, two different prototypes were fabricated in which RIR-MAPLE was used to deposit GRIN AR coatings on polycarbonate substrates. The first GRIN film design consisted of 10 nm slices of constant material composition, while the second design consisted of 20 nm slices of constant composition. The theoretical results showing identical film performance between 10 and 20 nm slices motivated the simplification to 20 nm slices because it reduced the number of distinct layers required during growth from 100 to 50 for a 1 μm thick film.

To deposit the films, sequential RIR-MAPLE deposition was used. Based upon deposition rate calibration runs for each material, a delay time was provided for each material within each constant-RI slice, during which the laser would raster only across that portion of the target. The control software was programmed to change the PS:PMMA ratio after a given slice was completed. In this way, the film was built up slice by slice. It is crucial to point out that although the films were comprised of thin slices of constant-RI material, that the resulting film is still graded because there was no break in the process between slices. Conversely, in spin-cast processing each constant-RI layer must be allowed to dry prior to subsequent layer depositions, meaning that the polymer layer is evolving from solution form to solid form during

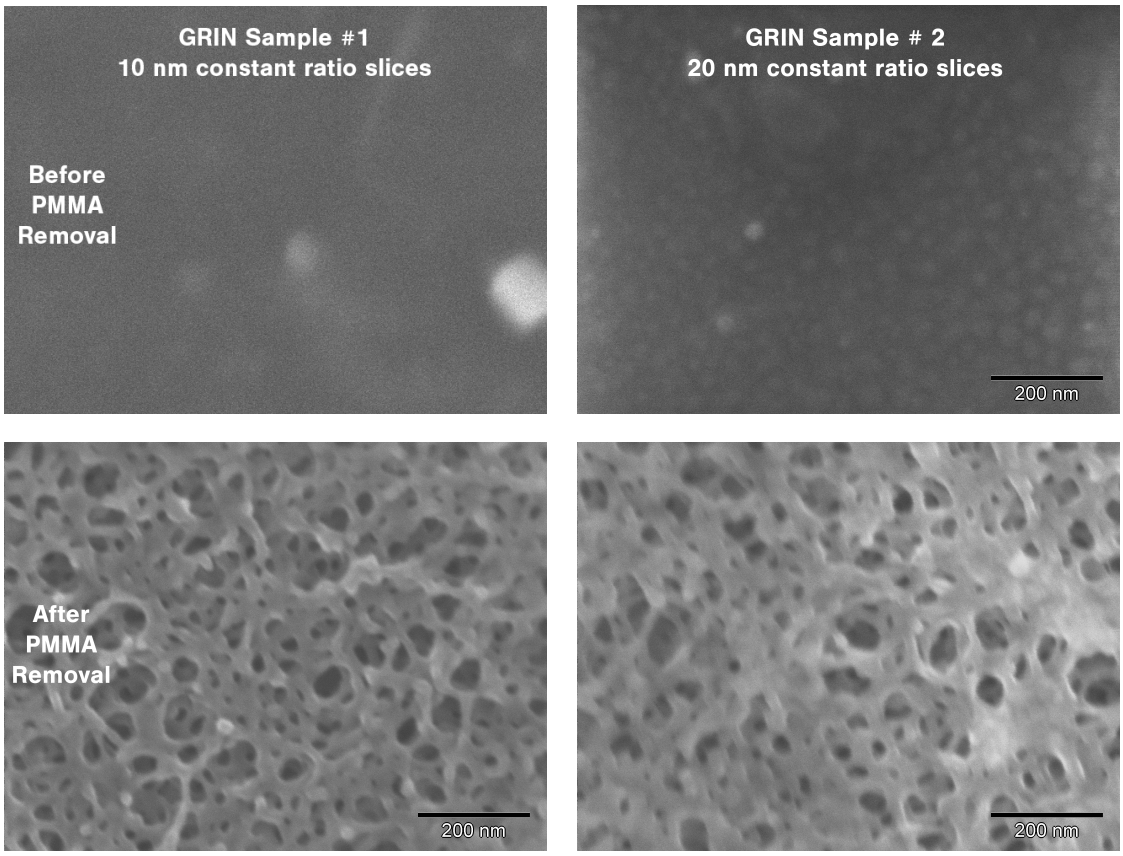

FIGURE 4.15: SEM images of the surface of the two GRIN films fabricated by RIR-MAPLE. The top row shows no porosity after deposition. The bottom row shows the porous PS structure at the film surface after porogen removal. The first column represents GRIN sample 1 with 10-nm slices. The second column represents GRIN sample 2 with 20-nm slices.

the deposition process. Moreover, all layers would be required to have orthogonal solvents to avoid dissolution of the previously deposited layers. In RIR-MAPLE, the majority of the solvents are removed from the polymers during the process so that there is minimal evolution of the deposited material after it contacts the substrate.

SEM images of both GRIN films before and after removal of the porogen PMMA are shown in Figure 4.15. Both designs show surfaces that have a similar appearance, so performance results are based primarily on the optical measurements of the films. The R/T/A measurements completed with an integrating sphere (Fig-

ure 4.16) showed that the two designs behaved differently. The 10 nm slice prototype performed better than the 20 nm slice prototype. Both GRIN films reduced the reflectance relative to the bare substrate. The transmittance was only improved in the 10 nm slice sample, and then only for wavelengths above 480 nm. The absorbance and scattering have been lumped into one parameter because the spectrometer could only measure diffuse and specular reflectance and total transmission. The absorbance/scattering was increased from 1-2% on the bare substrate to 4-5% for both GRIN films. Therefore, the reflectance has been reduced, but it was replaced with an absorbent, scattering haze, as observed in the photo of Figure 4.16.

Visible inspection of the films under magnification revealed that the film surfaces contained micron-sized features, usually pits reducing the film thickness, that contribute to the increase in absorbance and scattering. In addition, a visual survey of the nanoscale pores in the SEM images indicates that some are larger than 10% of the shortest relevant wavelengths, which degrades performance at the blue end of the visible spectrum. Still, the 10-nm slice prototype reduced the reflectance and increased the transmittance through the visible range, proving that RIR-MAPLE has the capability to fabricate thin organic film structures that were previously out of reach. Future designs will require that the microscale features be eliminated and that the pore sizes be reduced in order to better approximate an effective medium throughout the entire AR coating thickness.

4.5 Conclusions

RIR-MAPLE has enabled true gradient films by providing nanoscale domain sizes relevant for porous effective media, and has provided a means to deposit the layered films necessary for such spatial grading, without the solvent restrictions of solution-based techniques. A polymeric, optical effective medium featuring a blend of different homopolymer components, PS and PMMA, and block copolymer, PS-b-PMMA, with

varying block sizes, has been deposited using emulsion-based RIR-MAPLE. Removal of the PMMA component after UV cross-linking of the PS component leaves a porous PS film that yields a decrease in reflectance and an increase in transmittance. Importantly, these porous films have been shown to behave as effective media for the majority of the visible spectrum. In addition, the corresponding RI value can be tuned from that of the bulk PS material near 1.59 to values below those achievable with bulk materials only. An RI of 1.20 in the visible region was achieved with the highest porosity film homopolymer film (75%). It should be possible to achieve an RI value closer to that for air in the polymer films by preventing collapse of the porous structures. Future work will focus on making the porous PS structures more stable and durable.

The demonstrated nanoscale, polymer blend domain sizes provided by emulsion-based RIR-MAPLE opens the technique and polymeric materials to a wide variety of applications. For example, optical effective media are useful beyond the AR coatings based on a GRIN profile [44] that provide the motivation for this work. The ability to tailor the constitutive parameters of blended polymer films could enable optical coatings and components [79] using novel materials, such as those that use the photorefractive effect where the domain sizes and constituent mixing are critical [80]. Porous scaffolds, which are applicable as fuel cells, aerogels [81, 82], or catalysts [83], are another area where nanoscale domain size plays an important role. For example, in catalytic processes, the pore size determines the flow rate and surface area of the reactants that contact the porous catalyst [83]. RIR-MAPLE can also facilitate multifunctional materials by blending two or more materials, each of which contains at least one desired quality of a multifunctional, composite material. For example, in the case of materials for drug release, one material may help with drug release (PEG), while the second material hinders drug release (PLGA). By controlling the domain size of each material in a blended film, the diffusion of the drug within the

blend [84] can be controlled. Thus, the capability of emulsion-based RIR-MAPLE to deposit blended polymer films with nanoscale domains helps resolve fundamental challenges faced by solution-based deposition and broadens the application of polymeric materials for functional thin films and coatings.

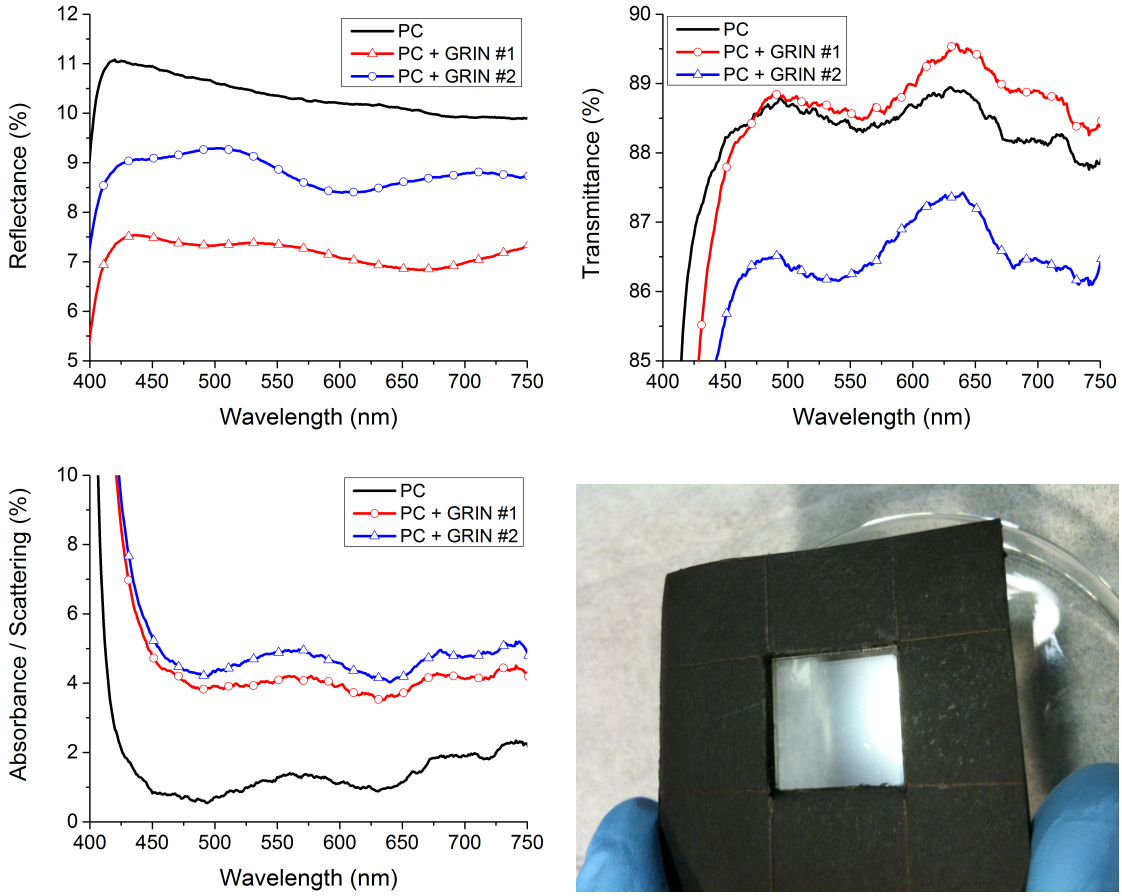

FIGURE 4.16: Optical R/T/A analysis using an integrating sphere of the bare polycarbonate (PC) substrate and the two RIR-MAPLE fabricated GRIN films. GRIN film 1 contained 100 slices of 10 nm thickness where each slice contained a constant RI ratio. GRIN film 2 contained 50 slices of 20 nm thickness at constant RI ratio in each slice. Reflectance is improved by both GRIN film design. Only design 1 improved transmission through the substrate. Both designs increased the absorbance and scattering across the spectrum. GRIN design 1 is shown in the bottom right image in a black holder to minimize contact with the film.

5

Organic Photovoltaics by Emulsion-Based RIR-MAPLE

Organic photovoltaics (OPV) show significant promise in power generation due to attractive features such as ease of deposition, light weight, structurally flexible, large-scale production, and reduced cost compared with inorganic cells. There has been much work done on the solution processing of polymers for optoelectronics devices, however, the resulting device properties have been shown to be generally uncontrollable and unrepeatable [85]. Large-scale production is particularly difficult due to the loss in average efficiency compared with higher efficiency research devices, which tend to be cherry-picked from a large sample pool and tend to have areas of the order of $\leqslant 1$ cm^2 [86]. Prior to this work, the highest power conversion efficiency (PCE) reported for a device fabricated by the MAPLE process was PCE = 0.03% and consisted of a solar cell with a bilayer active region ($V_{OC} = 0.32$ V, $J_{SC} = 0.33$ mA/cm^2, and FF = 0.28) [87]. The work in this chapter will demonstrate that emulsion-based RIR-MAPLE is capable of producing a P3HT:PCBM solar cell with PCE = 1.0%.

The OPV active region under investigation comprised an electron-donating polymer, poly(3-hexyl thiophene) (P3HT) and an electron-accepting small molecule, [6,6]-

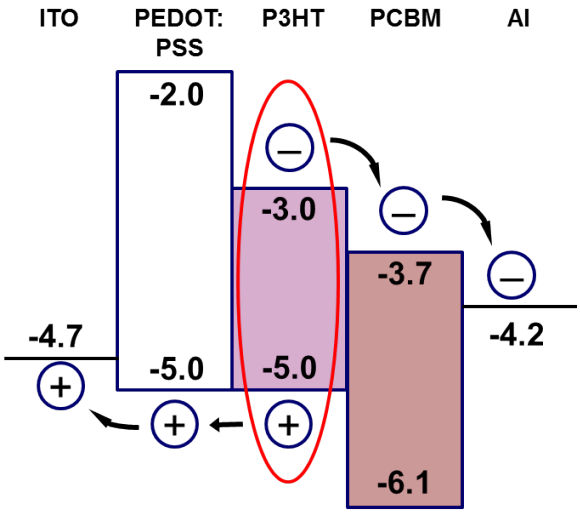

FIGURE 5.1: Energy band diagram of P3HT:PCBM photovoltaic device showing LUMO and HOMO values in eV relative to the vacuum level. The P3HT absorbs photons that create excitons, which are then split at the P3HT/PCBM interface into free carriers. Electrons are collected at the Al cathode; and, holes are collected at the ITO anode.

phenyl-C_{61} butyric acid methyl ester ($PC_{61}BM$). Although there are several other ball-shaped allotropes of carbon, notably C_{70}, that are used as electron acceptors with or without functionalized side chains, we drop the "61" notation going forward for simplicity. The P3HT lowest unoccupied molecular orbital (LUMO) and highest occupied molecular orbital (HOMO) levels were reported to be -3.0 eV and -5.0 eV, respectively. The PCBM LUMO and HOMO levels are located at -3.7 eV and -6.1 eV, respectively. P3HT has been shown to be more crystalline than other semiconducting polymers. When mixed with PCBM, P3HT will self-assemble into a generally amorphous bulk with crystalline domains of P3HT and PCBM scattered throughout the bulk [88]. The separation of the domains is required to be on the order of the diffusion length in each material so that two mechanisms can efficiently occur, shown in the schematic diagram of Figure 5.1. First, because most of the photon absorption occurs in the P3HT, PCBM domains must be located within a

diffusion length of the polymer domains so that efficient splitting of photogenerated excitons into free electrons and holes will take place at the interface. The difference between the LUMO levels of P3HT and PCBM provides the energy needed to overcome the exciton binding energy of approximately 1.0 eV in order to generate free carriers. Second, separated holes and electrons must diffuse to the lower resistance, more crystalline regions of the P3HT and PCBM, respectively, to facilitate transport to the contacts. The carriers must then traverse the lower-resistance ordered regions via hopping conduction between localized energy states, which is different from the delocalized transport through crystalline inorganic semiconductors.

5.1 RIR-MAPLE Growth of OPV Active Regions and Device Characterization

To prepare the active layer materials for deposition, P3HT and PCBM were separately dissolved in ortho-dichlorobenzene (oDCB). Dissolution was aided by heating the materials to 60 °C in air overnight. Next, phenol, heated to 60-70 °C to liquefy it, was mixed with the oDCB in volume ratios of 2:1 oDCB:phenol for the P3HT, and 1:1 for the PCBM. The different volume ratios result from the fact that P3HT has a smaller solubility radius than PCBM (see Appendix B). Phenol serves two purposes: to add O-H bonds to the target to absorb the infrared (IR) laser energy, and to lower the vapor pressure of the mixture to reduce evaporation of the higher vapor pressure oDCB in the vacuum environment. Finally, DI water is added in a volume ratio of 4:1 water:oDCB to be used as the primary absorber of the IR laser energy. Because this mixture is an oil/water emulsion, the phases remain separate until a small amount of surfactant is added. Sodium dodecyl sulfate (SDS) was added to the DI water prior to mixture with the solvents at a concentration of 0.001 wt% to facilitate mixing of the oil and water phases. The surfactant study of Chapter 3 explains how the appropriate amount of SDS was determined.

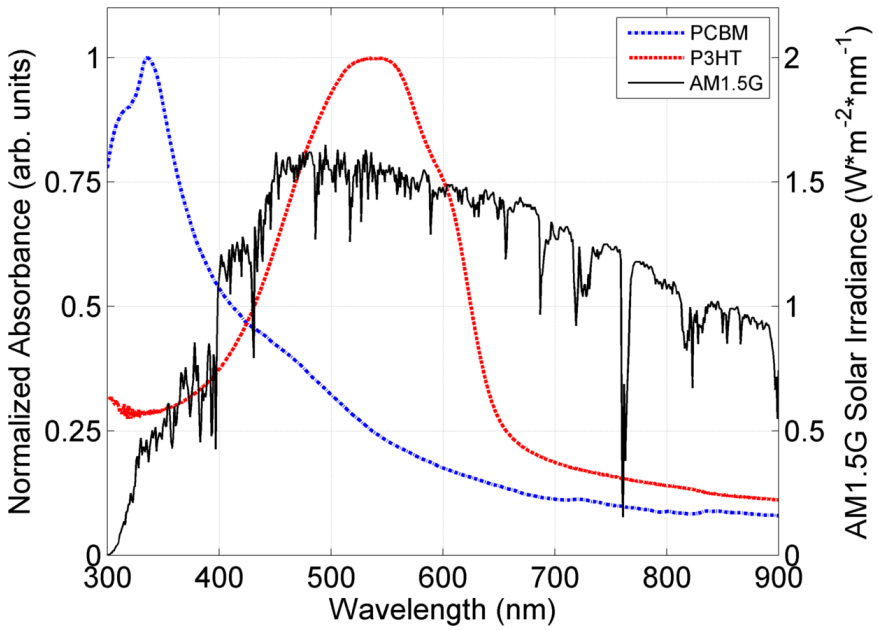

FIGURE 5.2: Measured UV-Vis absorbance of PCBM and P3HT, normalized to the peak value, plotted against the AM 1.5G solar spectrum [1].

Four primary figures of merit for photovoltaic devices are routinely extracted from a current-voltage (IV) plot, and include the open-circuit voltage, V_{OC}(V), the short-circuit current density, J_{SC} (mA/cm^2), the fill factor, FF (unitless), and the power conversion efficiency, PCE (%). IV measurements of all OPV devices in this work were completed using a Keithley Instruments 4200-SCS semiconductor analyzer. JV plots of current density versus voltage normalize the current by the device active area so that comparison can be made amongst devices of differing size. A solar simulator (Abet Technologies, model 10500) was set to one-sun equivalent output irradiance (AM 1.5G spectrum [1]) at 25 °C by placing a calibrated reference silicon cell (Oriel, model 91150) in the output path and adjusting the focus of the solar simulator Xe lamp.

External quantum efficiency (EQE) is defined as the number of electrons that reach the external circuit relative to the number of photons incident on the cell [89]. The measurement is taken at zero bias through the spectral region to which the cell

responds. The measured UV-visible (UV-Vis) absorbance of both PCBM and P3HT are shown in Figure 5.2 along with the AM 1.5G solar spectrum [1]. It is clear that there are very few solar photons available for the PCBM to absorb, so the majority of the solar power will be absorbed by the P3HT polymer. Grazing incidence, wide angle x-ray scattering (GIWAXS) and UV-Vis absorbance measurements of P3HT:PCBM devices were made following the same procedures as for the P3HT-only devices in Chapter 3, which are described in Section 3.1.2 and Section 3.1.4, respectively.

5.2 Bulk Heterojunction P3HT:PCBM Ratio Study

The most common research-grade OPV device reported on in the literature is fabricated by spin-casting. After many studies, the optimum ratio, as defined by the highest photovoltaic PCE, of P3HT:PCBM for a bulk heterojunction structure has been determined to be slightly more P3HT than PCBM in a volume ratio of 1:0.7 or 1:0.8 [90, 91]. The spin-casting process allows the user to directly determine the ratio of the two materials in the resultant film by solution concentration alone. In contrast, the RIR-MAPLE process has an additional step that might be described as a "transfer efficiency." For example, one prepared target may contain 1 wt% each of two separate materials dissolved and frozen within it resulting in a 1:1 volume ratio within the target. However, the rate at which the laser transfers each of the two materials to the substrate may be very different, depending on many factors, such as molecular weight, absorption coefficient of the emulsion, and the quality of the emulsion (i.e. oil/water domain sizes). Therefore, it is important to determine the optimum ratio of these materials *within the RIR-MAPLE target* in order to fabricate an optimized BHJ OPV.

A wide range of P3HT:PCBM volume ratios was chosen: 1:3, 1:2, 1:1, 2:1, 3:1. Calibration depositions of each material separately determined that P3HT tends to deposit nearly twice as fast as PCBM. Consequently, P3HT was prepared at a

Table 5.1: OPV metrics for the P3HT:PCBM BHJ ratio study.

P3HT: PCBM	V_{OC} (V)	J_{SC} (mA/cm^2)	FF	PCE (%)
1:3	0.383	1.594	0.396	0.242
1:2	0.414	1.701	0.388	0.273
1:1	0.670	2.303	0.469	0.725
2:1	0.560	1.209	0.417	0.282
3:1	0.569	1.973	0.444	0.499

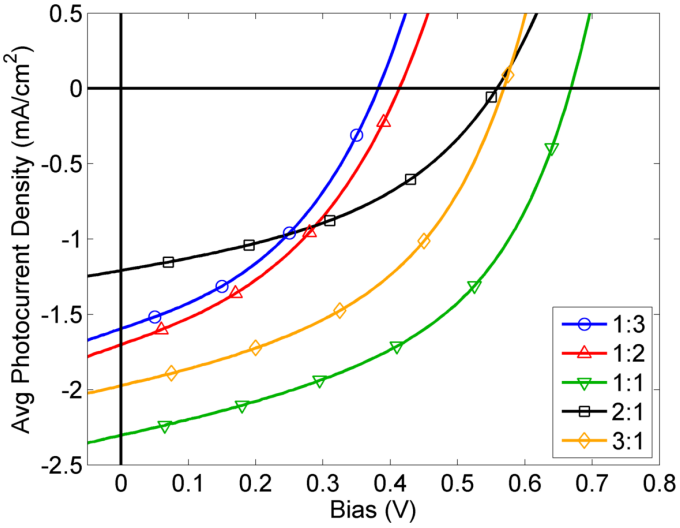

FIGURE 5.3: Average photocurrent density versus applied bias for each of the five RIR-MAPLE target volume ratios: 1:3, 1:2, 1:1, 2:1, and 3:1. Each curve is the average of six different 9 mm^2 devices.

reduced concentration in its primary solvent, ortho-dichlorobenzene (oDCB), compared to PCBM in its primary solvent (also oDCB) as an attempt to equalize the deposition rates. The RIR-MAPLE target was partitioned so that each material is frozen separately in its own location and can therefore be used to control the ratio of the materials in the film. For each P3HT:PCBM ratio, six 9 mm^2 OPV devices per substrate were measured separately for the IV and EQE measurements. The average current density versus applied bias is shown in Figure 5.3, with the corresponding four primary metrics shown in Table 5.1. The device with the highest PCE was the

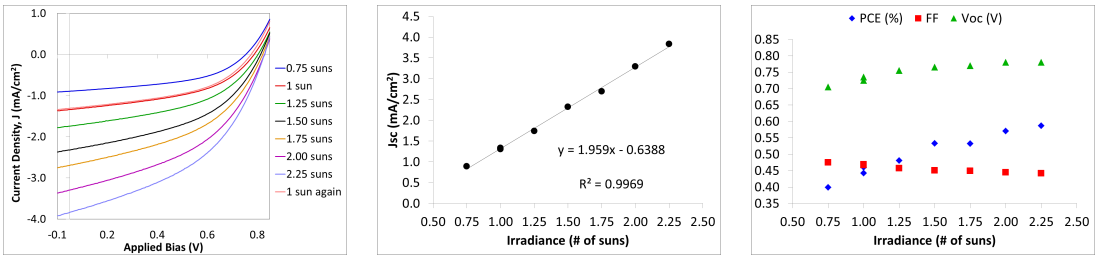

FIGURE 5.4: JV response of a bilayer device to an irradiance of 0.75-2.25 suns in 0.25-sun increments, demonstrating the proportionality of the current to irradiance.

1:1 ratio device with 0.725%. The majority-PCBM devices performed the worst, generally due to the low V_{OC} values. The 2:1 device performance appears anomalously low compared with the 1:1 and 3:1 devices, and may be due to a thinner active layer.

It is important to note that for this early study, the IV measurement setup did not contain a mask to isolate each device. Therefore the current densities are artificially high by approximately 30%. This was not concerning for the ratio study because the goal was only to determine the best performing ratio of materials, not find the absolute PCE values. The assumption that the measured values would still follow the same trends while masked to the device size derives from the observed linear response of the current to the irradiance, shown in Figure 5.4. Therefore, reducing the active area is comparable to decreasing the irradiance.

The EQE plots in Figure 5.5a give more insight into the IV results. The two materials complement each other by having separate regions of the spectrum in which each dominates the absorption of light. The boundary between the two regions is roughly split along the UV/visible boundary at $\lambda = 400$ nm, where the PCBM peaks around $\lambda = 336$ nm, and the P3HT has a broad peak in the region $\lambda = 520$-560 nm. The EQE in each region is a direct measure of the ability of each material to absorb light, generate excitons, and separate the excitons at a P3HT:PCBM interface, and transport the free carriers successfully to the external circuit via the contacts.

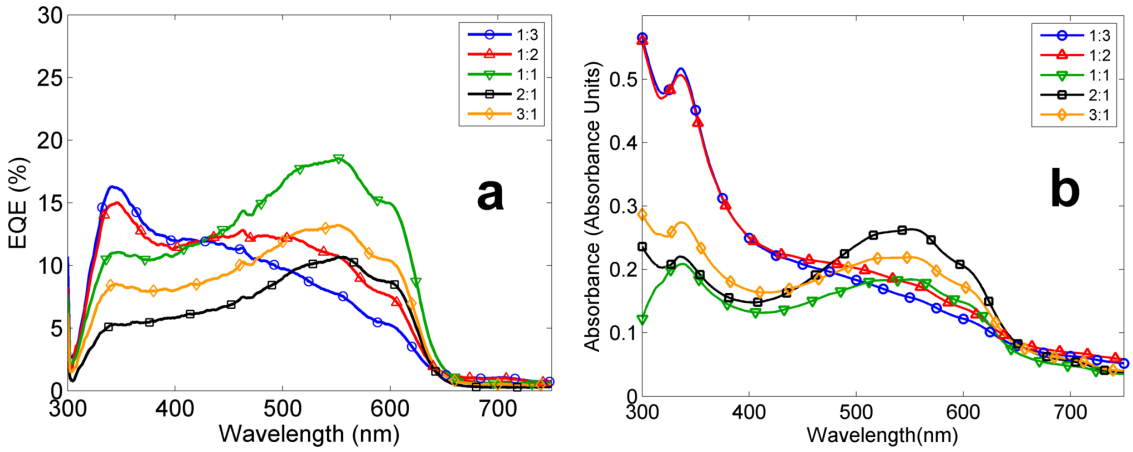

FIGURE 5.5: (a) Measured external quantum efficiency and (b) UV-visible absorbance for five RIR-MAPLE target volume ratios of P3HT:PCBM OPVs 1:3, 1:2, 1:1, 2:1, 3:1.

All EQE data were measured spatially at the same location within the light source. However, the devices were not masked to the device area during measurement. Therefore, the spectral shape of each ratio is correct, but the absolute EQE level required scaling. It is well known that the short circuit current density can be derived from EQE spectra [89]. The relationship between Jsc and the EQE spectrum is the following:

$$J_{SC} = \frac{q}{hc}\int_{\lambda_1}^{\lambda_2} \lambda(EQE(\lambda))S(\lambda)d\lambda \tag{5.1}$$

where S(λ) represents the illumination spectral irradiance, q is the elementary charge, h is Plancks constant, and c is the speed of light. Because a solar simulator was used for this measurement, the solar spectrum (AM 1.5G) is substituted for S(λ). The absorbance measurements are shown in Figure 5.5b.

GIWAXS data were measured to determine the orientation of the P3HT chains relative to the plane of the substrate. Two-dimensional GIWAXS plots are shown in Figure 5.6. Measurements of a film composed only of PCBM are shown in Figure 5.6f: the telltale signs of PCBM are the omnidirectional orientation of the strong peak near

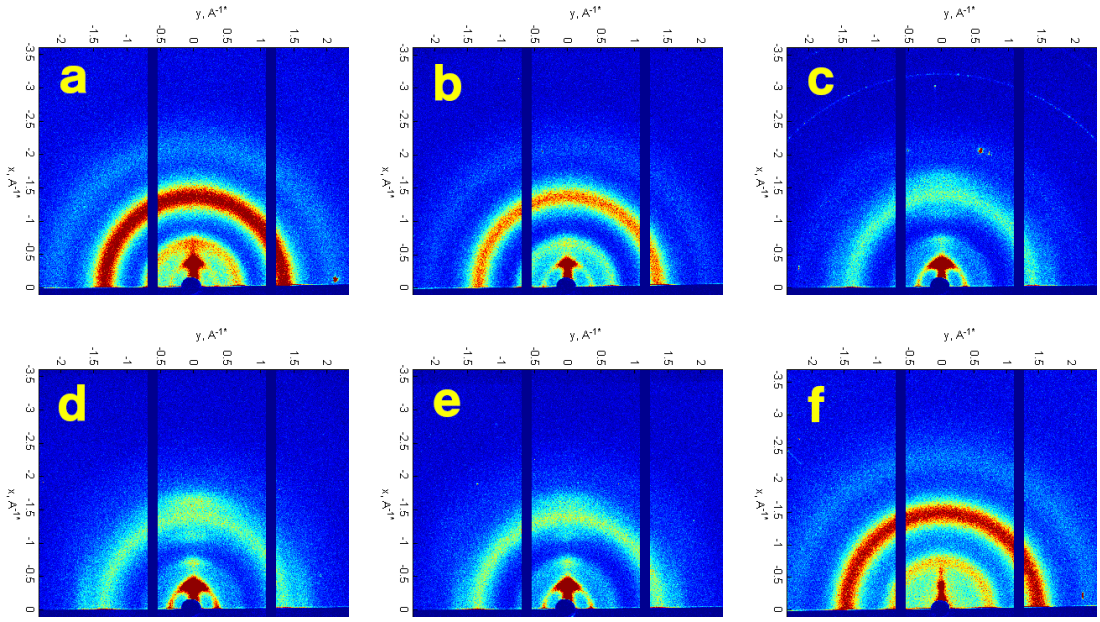

FIGURE 5.6: 2D GIWAXS images of films made of the following RIR-MAPLE P3HT:PCBM target ratios: (a) 1:3; (b) 1:2; (c) 1:1; (d) 2:1; (e) 3:1. For comparison, a PCBM-only film deposited by RIR-MAPLE is shown in (f).

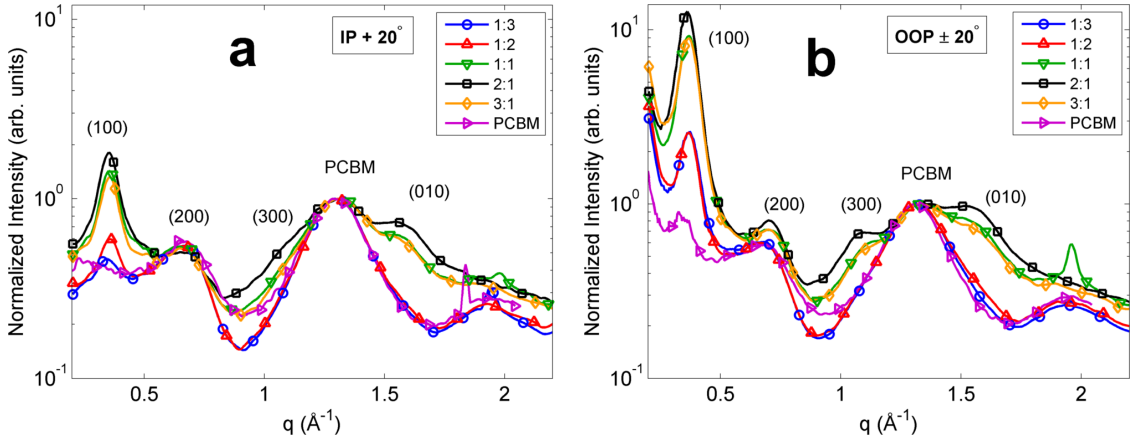

FIGURE 5.7: 1D GIWAXS data from Figure 5.6 integrated along the (a) IP and (b) OOP directions and normalized to the PCBM peak near q = 1.30 Å^{-1} to accentuate the P3HT peaks.

Table 5.2: Peak ratios measured from 1D GIWAXS data in Figure 5.7. The 1:3 and 1:2 P3HT:PCBM devices had no (010) peak from which to calculate a ratio.

P3HT:PCBM	IP		OOP		OOP/IP	
	(010)/(100)	(010)/PCBM	(010)/(100)	(010)/PCBM	(010)/(100)	(010)/PCBM
1:1	0.437	0.624	0.084	0.771	0.192	1.236
2:1	0.408	0.737	0.074	0.940	0.181	1.275
3:1	0.452	0.598	0.079	0.709	0.175	1.186

q = 1.30 $Å^{-1}$, and the two weaker peaks near the P3HT (200) peak and near q = 1.95 $Å^{-1}$. Figures 5.6a-e represent a progression from the most to the least percentage of PCBM in the film. It is clear that the addition of one material reduces the structural order of the other material, which is clearly evident in Figures 5.6a-c, but requires the 1D integrations in Figure 5.7 to discern the differences in the majority P3HT films. The curves are normalized to the PCBM peak near q = 1.30 $Å^{-1}$, which enhances the (300) and (010) peaks, and are plotted on the same y-axis scale for comparison. The films that contain greater than 50% PCBM exhibit a suppression of almost all P3HT structure. The P3HT is less disruptive of the ordered PCBM regions due to the PCBM molecules being physically much smaller than P3HT chains.

Table 5.2 displays the peak ratios of 1D GIWAXS data in an analysis identical to the P3HT-alone devices in Section 3.2. An interpretation of the OOP/IP metric can be described using a Gedanken experiment. Solar cells are only useful as power sources if they work as ambipolar devices. If only one carrier reaches the contacts, then the device rapidly becomes space-charge limited by the build-up of the non-transporting carrier. Because PCBM is a small molecule, it is assumed that conduction through PCBM is isotropic. Therefore, the anisotropic conduction of P3HT may affect the device performance by orienting more conductive pathways in different directions.

It may be useful to examine the relative quantities of crystalline polymer domains

and how they are oriented relative to the direction of charge conduction in the device. Charge conduction in P3HT is highest along the polymer backbone, then next highest between the π-π orbital overlap region between two adjacent backbones; the carbon side chain axes represent the least conductive pathway. Because the resistance will be lowest along a polymer backbone lacking conformational defects, the charge will travel along this conjugation length until a conformational defect is reached. At that time, it may be energetically more favorable to hop to another polymer chain. The lowest resistance hopping direction is along the (010) direction, between adjacent backbones. Hence, it is useful to look at the ratio of lower-resistance (010) crystallite domains versus the higher resistance (100) crystallite domains. Transport in vertical devices will ultimately follow the path of least resistance and very likely will be 3D in nature in an amorphous material system such as P3HT and PCBM. As such, the OOP/IP (010)/(100) ratio provides a relative quantity of low resistance pathways in the vertical direction relative to the lateral direction. To be clear, this ratio estimates the charge transport properties only and has nothing to do with light absorbance or exciton generation and dissociation.

In addition to the structural information inferred from the GIWAXS study, an analysis of the P3HT UV-visible absorbance using the Spano theory outlined in Chapter 3 can determine some information about the level of crystallinity in the polymer regions. Because the data presented here encompass the absorbance of both the P3HT and PCBM components, the PCBM component must be removed to compare the data with the model. The absorbance of a PCBM-only film was measured and then scaled to match the peak value of the combined P3HT:PCBM data. Both sets of data were also smoothed using a robust local regression model in MATLAB that weights each point proportionally to the local median before fitting a quadratic polynomial to each local window, which encompasses 3% of the total data set. The advantage of using this method is that the ability of outliers to skew

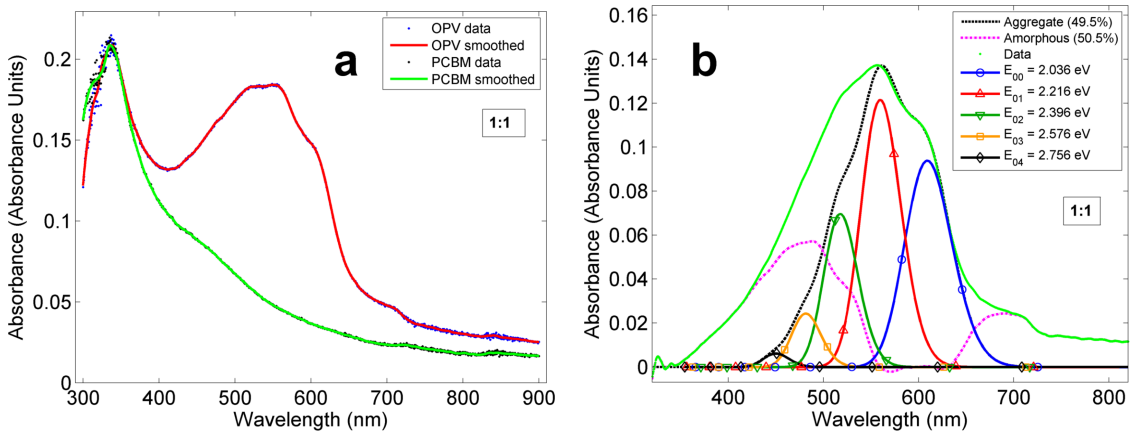

FIGURE 5.8: (a) OPV and PCBM-only absorbance data are shown for a 1:1 P3HT:PCBM RIR-MAPLE target ratio. The data are locally smoothed and then the PCBM-only data are scaled to the OPV PCBM peak to be subtracted. (b) The resulting P3HT contribution is shown with the Spano theory overlaid, which determines the crystalline aggregates in the P3HT bulk. The remainder of the spectrum accounts for disordered chains in the amorphous regions.

Table 5.3: Spano absorbance analysis fit parameters for RIR-MAPLE BHJ P3HT:PCBM films.

P3HT:PCBM Ratio	1:3	1:2	1:1	2:1	3:1
FWHM, σ (meV)	81.1	82.6	82.5	83.1	82.5
Exciton Bandwidth, W (meV)	153.5	166.7	155.8	178.6	166.5
Estimated % Aggregates	64.1	57.8	49.5	52.5	52.8

the smoothed curve is reduced. The PCBM values were then subtracted from the combined data, as in Figure 5.8a, to leave the contribution due to P3HT only, shown in Figure 5.8b as "Data".

The results of the Spano analysis are shown in Table 5.3. The best performing device, the 1:1 ratio device, consists of the smallest amount of aggregates, indicating that percent crystallinity is only one component that affects device performance. However, the 1:1 device does contain a smaller exciton bandwidth, which correlates

Table 5.4: OPV metrics for the P3HT:PCBM BHJ ratio study near 1:1.

P3HT: PCBM	V_{OC} (V)	J_{SC} (mA/cm^2)	FF	PCE (%)
0.7:1	0.735	3.278	0.415	0.998
1:1	0.663	2.806	0.344	0.640
1:0.7	0.794	2.361	0.429	0.804

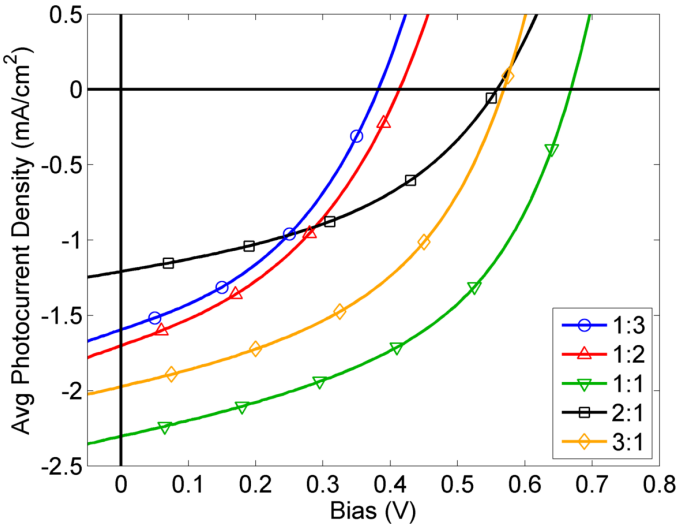

FIGURE 5.9: Average JV characteristics of the 2nd ratio study to determine the true optimum RIR-MAPLE target ratio of P3HT:PCBM in a BJH OPV device. Each curve is the average of six different 9 mm^2 devices. The work was motivated by knowledge of the optimum ratio of P3HT:PCBM in spin-cast films, which is slightly larger than unity.

well with a more ordered film [58].

5.3 Optimizing the P3HT:PCBM Ratio in the Bulk Heterojunction Structure

The results of the ratio study indicated at that a 1:1 P3HT:PCBM ratio in the RIR-MAPLE target would give the optimal results for a bulk heterojunction solar cell. However, as mentioned before, spin-cast films tend to exhibit their optimal performance at a ratio of P3HT:PCBM slightly larger than unity, such as 1:0.7 or

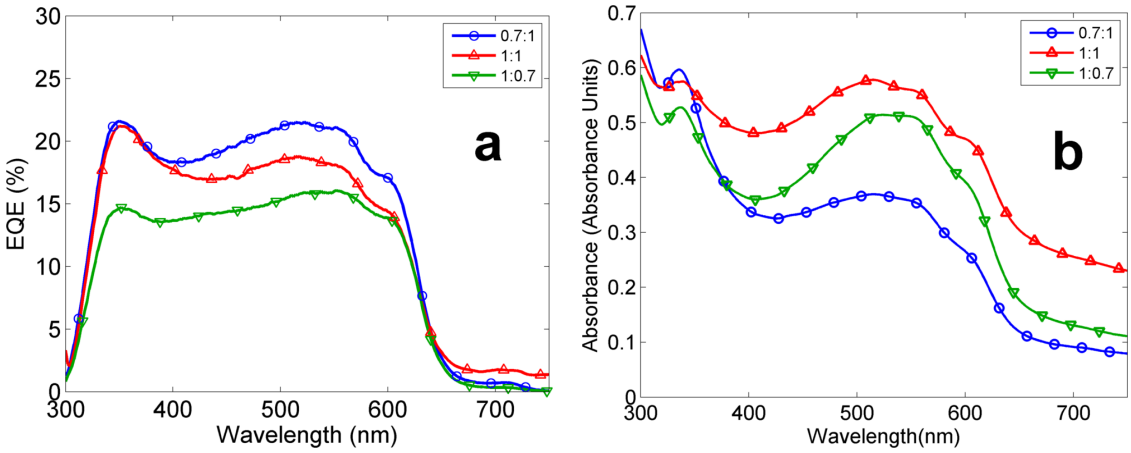

FIGURE 5.10: (a) EQE and (b) absorbance for the three ratios near 1:1 P3HT:PCBM RIR-MAPLE target volume ratio: 0.7:1, 1:1, 1:0.7.

1:0.8 [91]. Therefore, an extension of the ratio study was made to the region around 1:1. Three ratios were chosen: 0.7:1, 1:1, and 1:0.7. These ratios represent the volume of each material present in the RIR-MAPLE target. The emulsion targets for each material were prepared identically to those prepared for the first ratio study. The results of this optimization study are shown in the JV curves of Figure 5.9 and the corresponding device metrics are shown in Table 5.4. Surprisingly, the optimum RIR-MAPLE ratio was found to be the opposite of spin-cast films at 0.7:1 P3HT:PCBM by volume. This ratio also provided the best performing devices with an average PCE = 1.0%.

The EQE and absorbance for the three ratios are shown in Figure 5.10. The best-performing device, the 0.7:1, had both the highest overall EQE, but also had approximately equal contributions to the current from the PCBM peak near 336 nm and the broad P3HT peak between 520-560 nm. The absorbance data in Figure 5.10b do not trend with the EQE or JV results. Rather, the 0.7:1 is shown to have the lowest absorbance of the three ratios. However, it is the P3HT contribution between 450-650 nm, and not the PCBM contribution, that is low. Therefore the volume ratio

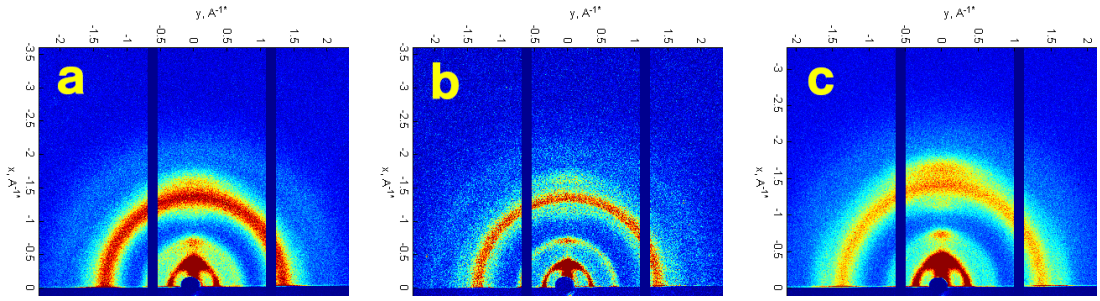

FIGURE 5.11: 2D GIWAXS images of the following RIR-MAPLE target ratios of P3HT:PCBM: (a) 0.7:1; (b) 1:1; (c) 1:0.7.

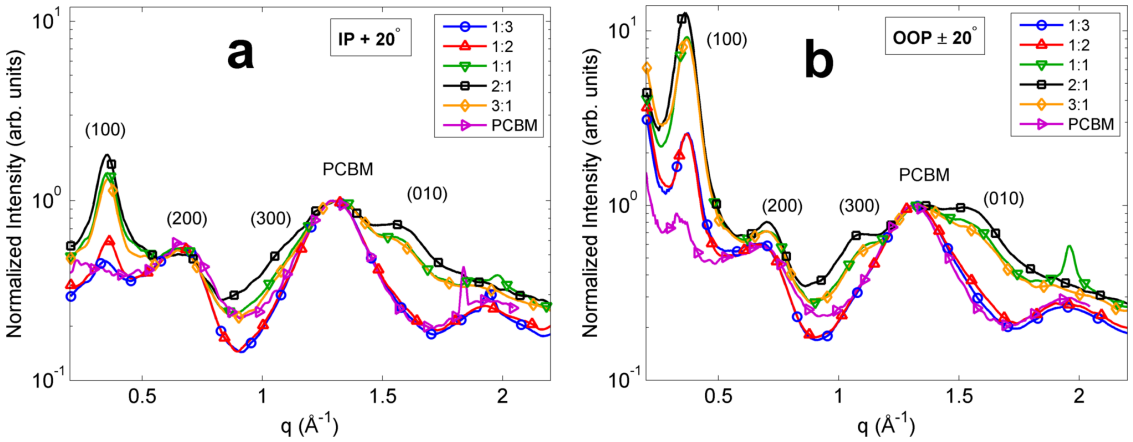

FIGURE 5.12: 1D GIWAXS data integrated along the a) IP and b) OOP directions from the data in Figure 5.11. The data have been normalized to the main PCBM peak near q = 1.30 Å^{-1} to accentuate the P3HT peak differences.

of the materials must play a role by either forming more organized polymer structures or orienting P3HT chains such that higher mobility crystallographic orientations are utilized as the charge percolation pathways. By looking at the GIWAXS data, we can determine that this is indeed the case.

The 2D GIWAXS images are shown in Figure 5.11, and the corresponding 1D integrations are shown in Figure 5.12, again normalized to the main PCBM peak near q = 1.30 Å^{-1} to accentuate the P3HT peak differences. The OOP/IP (010)/(100) ratio (see Table 5.5) is largest in the device with the highest PCE, the 0.7:1 device.

Table 5.5: Peak ratios measured from 1D GIWAXS data in Figure 5.12.

P3HT:PCBM	IP		OOP		OOP/IP	
	(010)/(100)	(010)/PCBM	(010)/(100)	(010)/PCBM	(010)/(100)	(010)/PCBM
0.7:1	0.342	0.410	0.104	0.571	0.304	1.393
1:1	0.291	0.441	0.069	0.522	0.237	1.184
1:0.7	0.335	0.652	0.087	0.894	0.260	1.371

Table 5.6: Spano absorbance analysis of the P3HT:PCBM ratios near 1:1.

P3HT:PCBM Ratio	0.7:1	1:1	1:0.7
FWHM, σ (meV)	83.5	79.6	82.8
Exciton Bandwidth, W (meV)	204.3	160.4	198.0
Estimated % Aggregates	58.5	37.7	51.8

The 1:1 and 1:0.7 devices also trend with the (010)/(100) ratio. There appears to be no correlation between the quantity of ordered (010) regions due to the P3HT and the quantity of ordered PCBM regions as determined by the GIWAXS data.

However, the exciton bandwidths tabulated in Table 5.6 have an inverse relationship with the PCE results. Therefore, the shortest average conjugation length along the backbone axis occurs in the 0.7:1 devices. This result gives strength to the idea that much of the transport must occur through interchain hopping. Additionally, the largest percentage of aggregates is in the 0.7:1 device, indicating that there are more domains to hop between within that device.

5.4 Device Structure Study

Layered or gradient structures of two or more materials are difficult to achieve by solution-casting methods due to the requirement that the two materials be soluble in orthogonal solvents to avoid removing a previously deposited layer. The process for both types of structures is straightforward for emulsion-based RIR-MAPLE. In

this section we present a comparison of organic photovoltaic devices fabricated by RIR-MAPLE with the bulk heterojunction, bilayer, and gradient structures.

Our hypothesis is that a gradient structure should result in the best performance of the three structures due to the combination of the BHJ and bilayer structures' best features. The BHJ has better exciton dissociation due to the large interfacial area between the materials, but still requires carriers to hop through their preferred materials (i.e. holes through P3HT and electrons through PCBM) without recombining at the numerous P3HT/PCBM interfaces to reach the contacts. The bilayer provides superior transport of the separated carriers to the contacts because of the minimization of recombination interfaces provided by a lack of the opposite material in the single-material layers. However, the bilayer lacks the large exciton dissociation area of the BHJ, so many photogenerated excitons in each single-material layer recombine because there is no interface to provide the energy to split the exciton, reducing the efficiency of the device. In contrast, the gradient structure provides an increase in the number of exciton dissociation interfaces throughout the active bulk compared with the bilayer, but the gradient material profile improves transport of the separated carriers by providing an increase, compared with the BHJ, in the volume of each carriers preferred material as it travels to its respective contact.

A schematic of the three structures is shown in Figure 5.13. All BHJ devices were deposited with split RIR-MAPLE targets, which contained separate volume regions for each material. Bilayer devices were deposited by first depositing P3HT alone, then moving the substrate with a wobble stick to an evacuated load lock chamber connected to the main deposition chamber without exposing the sample to atmosphere. The RIR-MAPLE target was replaced with PCBM alone and the deposition chamber was evacuated prior to reintroducing the substrate. The PCBM layer was then deposited. For simplicity, the bilayer structures were fabricated by depositing equal-thickness layers onto the substrate. All gradient layered devices

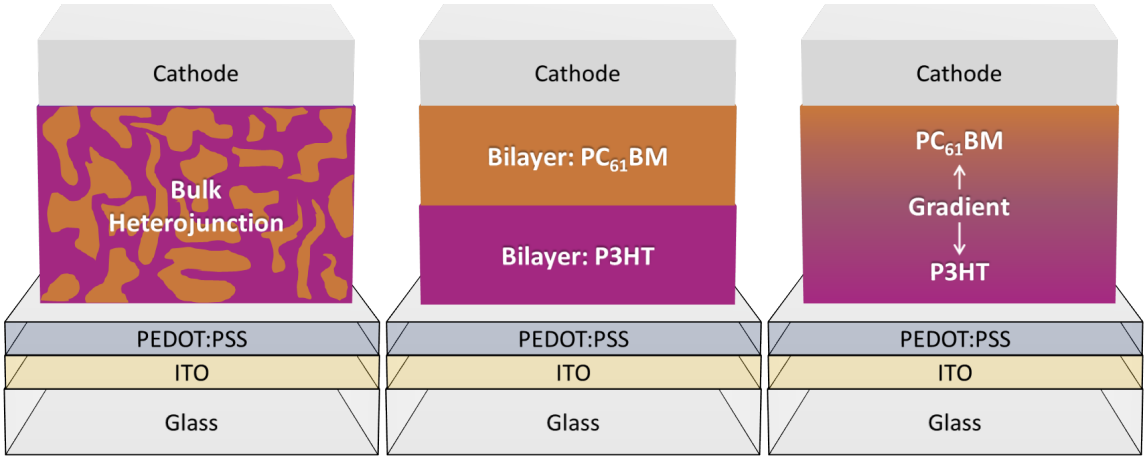

FIGURE 5.13: Schematic of the three OPV structures fabricated by RIR-MAPLE: a bulk heterojunction, a bilayer, and a gradient layered film.

Table 5.7: OPV metrics for different device structures.

P3HT: PCBM	V_{OC} (V)	J_{SC} (mA/cm^2)	FF	PCE (%)
BHJ (0.7:1)	0.730	3.303	0.413	0.995
Bilayer	0.681	2.651	0.421	0.762
Gradient	0.727	3.079	0.431	0.964

were deposited by splitting the RIR-MAPLE target. The gradient films consisted of 11 layers that began with a solid layer of P3HT, which was followed by nine middle layers that increased the PCBM content in 10% increments, and was finally capped by a solid layer of PCBM. The ratio of the materials was controlled by varying the time the laser spent ablating one target material relative to the other.

The electrical characteristics of the best performing devices for each OPV active region structure are shown in Figure 5.14 and Table 5.7. It is important to note that each curve is an average of six different 9mm^2 devices. The BHJ and gradient devices were remarkably similar in performance. Both device structures were measured to have power conversion efficiencies of 1.0%, which is a record for a MAPLE-deposited BHJ device and the first time a gradient structure has been fabricated and char-

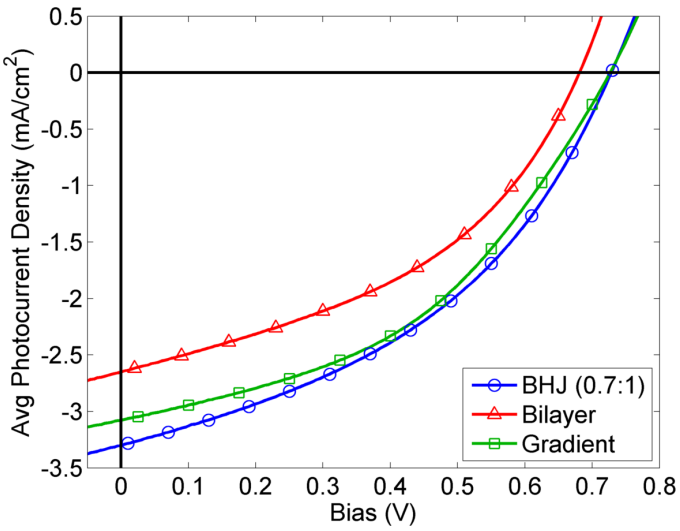

FIGURE 5.14: Best performance of each device structure deposited by RIR-MAPLE: bulk heterojunction at the optimum target volume ratio of 0.7:1 P3HT:PCBM, a bilayer of equal thickness P3HT and PCBM layers, and a gradient layered film. Each curve is an average of 6 different 9 mm^2 devices.

acterized. The bilayer performance demonstrates the limitations afforded by this structure. The reduced output current is due to the limited interfacial area providing exciton dissociation, whereas in the BHJ and gradient structures, almost the entirety of the active bulk contains exciton dissociation locations at the material interfaces spread throughout the thickness.

The EQE data in Figure 5.15a all demonstrate that the three device structures are approximately 20% efficient at converting photons to charge carriers. The absorbance data in Figure 5.15b appear to be uncorrelated with the electrical performance, but are included here for completeness.

The 2D GIWAXS data are shown in Figure 5.16, and the corresponding 1D integrations in the IP and OOP directions are shown in Figure 5.17. When comparisons are attempted using the GIWAXS peak ratios tabulated in Table 5.8, it becomes clear that these ratios are not suited for comparison when measuring different device structures. It is important to remember that the GIWAXS peak ratios attempt to

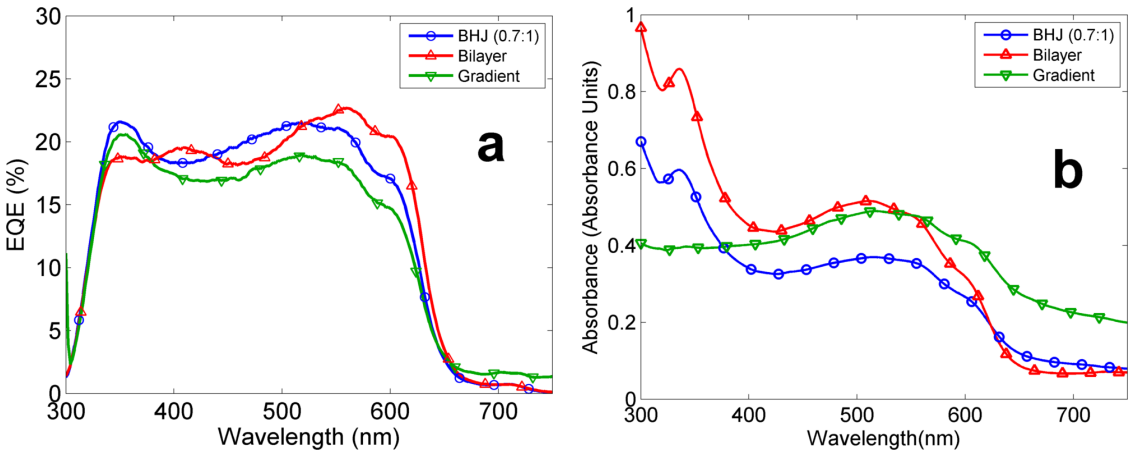

FIGURE 5.15: (a) EQE and (b) absorbance of the highest performing device of each structure type.

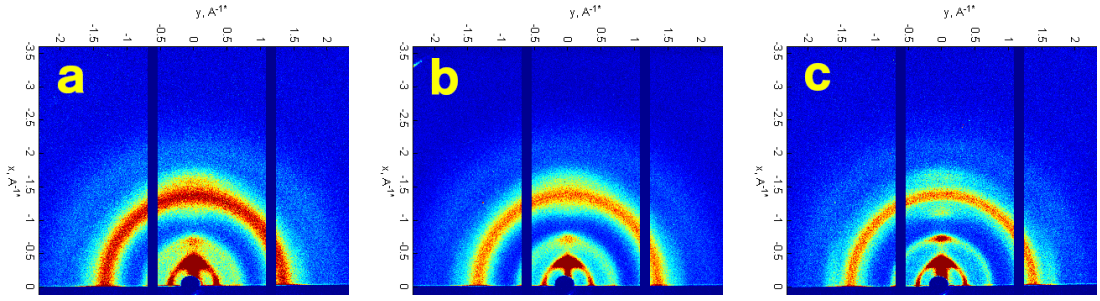

FIGURE 5.16: 2D GIWAXS images of the highest PCE device of each structure type: (a) BHJ (0.7:1); (b) Bilayer; (c) Gradient.

capture the carrier transport properties of the structures. Upon altering the internal morphology of the structures by spatially changing the positions of the P3HT and PCBM molecules in the average direction of charge transport (e.g. z-direction in a vertical device), other factors need to be accounted for as well. For example, exciton generation and dissociation rates, and carrier recombination rates will differ from structure to structure. Therefore the GIWAXS peak ratios as predictors of device performance appear to be limited to variations within a given type of structure where the spatial composition of the device is not altered along the average direction

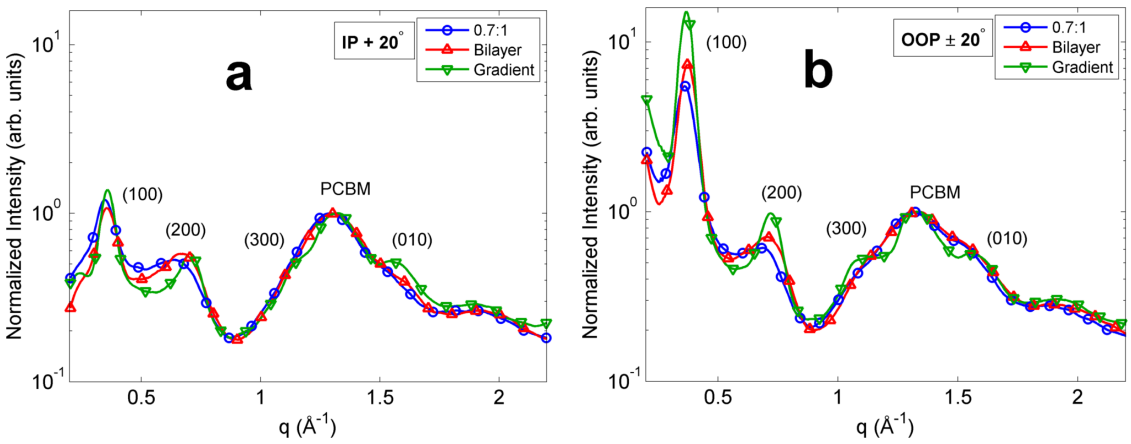

FIGURE 5.17: 1D GIWAXS data integrated along the a) IP and b) OOP directions for the highest PCE devices of each type in the study.

Table 5.8: Peak ratios measured from 1D GIWAXS data in Figure 5.17.

P3HT:PCBM	IP		OOP		OOP/IP	
	(010)/(100)	(010)/PCBM	(010)/(100)	(010)/PCBM	(010)/(100)	(010)/PCBM
BHJ (0.7:1)	0.342	0.410	0.104	0.571	0.304	1.393
Bilayer	0.397	0.426	0.081	0.596	0.204	1.399
Gradient	0.369	0.510	0.037	0.558	0.100	1.094

of charge transport.

Finally, the Spano absorbance data presented in Table 5.9 show a curious result that warrants further study. The small percentage of ordered aggregates in the gradient devices is offset by the very small exciton bandwidth, which correlates with a longer unbroken conjugation length along the polymer backbone axis. The BHJ device, by contrast, has nearly twice the ordered aggregates, but the performance is tempered by the shorter backbone conjugation (as determined by the large exciton bandwidth). What is curious about this outcome is that both devices achieved almost identical electrical characteristics and were both the best-performing devices overall.

Table 5.9: Spano absorbance analysis of the different OPV structures.

Structure	BHJ (0.7:1)	Bilayer	Gradient
FWHM, σ (meV)	83.5	81.8	82.1
Exciton Bandwidth, W (meV)	204	221	149
Estimated % Aggregates	58.5	53.9	35.0

5.5 Conclusions

Organic photovoltaic devices of P3HT and PCBM have been deposited by RIR-MAPLE to determine how the process affects the performance. A study to determine the optimum volume ratio of P3HT to PCBM in the RIR-MAPLE target determined that a 0.7:1 P3HT:PCBM ratio produced BHJ devices with the highest PCE of 1.0%. A structure study provided two primary benefits: it demonstrated the capability of the RIR-MAPLE process to create bilayer and gradient layered films, not possible with solution methods; and, the predicted superior performance of the gradient structure proved to be approximately equivalent to the BHJ, perhaps due to interfacial roughness between the constant-ratio gradient layers. However, the gradient layered devices also achieved 1.0% power conversion efficiency, matching the BHJ performance.

Overall, emulsion-based RIR-MAPLE has been demonstrated to provide versatile performance and applicability in the fabrication of organic thin films. Specifically, RIR-MAPLE has proven to be more versatile in the deposition of polymers, polymer blends, and polymer/nanoparticle blends regardless of the compatibility of the material solubilities. Layered heterostructures are successfully demonstrated to work as designed. Moreover, RIR-MAPLE produces films that act as effective media, which are dependent on small nanoscale domain sizes, which are difficult to control with

solution methods. Finally, layered films of different materials can be deposited using only the RIR-MAPLE process, which preserves interfaces that may be sensitive to environmental conditions. As always, there is more work to be done, but emulsion-based, RIR-MAPLE possesses unique capabilities that when further optimized may produce results that are not possible with any other organic thin film deposition technique.

6

Future Work

Emulsion-based RIR-MAPLE has progressed in its capabilities and achievements. However, there are still breakthroughs and improvements to be made before it can be considered a mature technology. In this final chapter, I will outline the problems that need attention in each of the areas represented in this dissertation by Chapters 2-5: 2) Fundamental RIR-MAPLE process; 3) Trade-offs presented by use of a surfactant in the target emulsion; 4) Gradient refractive index anti-reflection coatings; and, 5) Organic photovoltaics. I will also suggest potential pathways to a solution when applicable.

A fundamental understanding of all the physical and chemical processes that comprise emulsion-based, RIR-MAPLE has not yet been achieved. A poorly understood, yet very important, process is the flash-freezing of the emulsion in the RIR-MAPLE target. It is highly desirable to understand and control the physics and/or thermodynamics of the freezing process to ensure repeatable and consistent thin film outcomes. There are several factors that affect this process. The miscibility of all materials in a given emulsion needs to be determined across the wide temperature range of 77-300 K in which the emulsion must exist in stable, or at least metastable,

form. Changes in miscibility with temperature and its time derivative will determine the final domain sizes of the constituent materials in the frozen emulsion, which in turn is important to the laser ablation process because it affects the absorption depth of the laser pulse. The laser absorption depth determines the ablation regime (see [18]) by raising or lowering the energy density in the ablated material, which affects the type of physical process that removes the target material and sets the ratio of solvents, water, and polymer that reaches the substrate surface.

The pressure in the vacuum chamber must be accounted for when composing the target emulsion. The target materials have different rates of sublimation depending on their vapor pressures. It is desirable for the target composition to remain well-mixed and negligibly changed throughout the duration of a deposition to avoid ablation regime changes, as mentioned above. Therefore, the choice of solvents needs to be guided not only by the Hansen solubility parameters (see Appendix B), but also by the phase diagram of pressure versus temperature, which also needs to be known over the temperature range 77-300 K. This new information may lead to a wider use of the parameter space available with the RIR-MAPLE process (see Appendix C).

The use of a surfactant in the RIR-MAPLE emulsion is germane to the topics of both Chapters 2 and 3. The surfactant used for this work, sodium dodecyl sulfate (SDS), has proven to be a double-edged sword. It provides well-mixed targets, but the electrical performance has been mixed: in-plane mobility appears to be comparable to solution-cast devices, but out-of-plane performance (represented by OPVs) has fallen short of comparable solution-cast devices. Therefore, two approaches present themselves. One approach is to explore other surfactants, and if possible, use conductive surfactants that are less likely to degrade electrical performance. A member of my doctoral committee, Prof. Jie Liu, suggested graphene oxide, which acts as a surfactant, but is also conductive. The second approach is to configure the target composition to eliminate the surfactant altogether. This may include elimination of

the water, or conversely, depositing water-soluble materials to eliminate the solvents, among other things.

The porous polystyrene films of which the gradient refractive index anti-reflection coatings are composed will need the following attributes to be improved. To reduce the optical haze that contributes to the higher level of absorbance and/or scattering, the surfaces of the films after the acetic acid exposure need to be smoother. That is, they need to contain only nanoscale features and no microscale (or larger) pits, undulations, or projections. Moreover, further optimization of the emulsion can be accomplished to reduce the domain sizes in the target and, subsequently, in the films. Finally, a material more structurally robust than polystyrene needs to be incorporated into the process to avoid the partial pore collapse observed in this work.

The organic photovoltaic devices fabricated with emulsion-based RIR-MAPLE have improved measurably since our first attempts. Here are a few suggestions that might provide a leap in performance, rather than the incremental improvements now observed. Introduce a controlled atmosphere in the form of an inert gas (e.g. nitrogen) glove box that attaches directly to the RIR-MAPLE chamber. Therefore, organic materials that are susceptible to water and oxygen can be processed from native material to finished device without exposure to either contaminant. For this to occur, a thermal evaporator will need to be included in the full system as well.

Improvements in the control of film roughness would benefit nanoscale device heterostructures that may need smooth interfaces to achieve superior performance. Conversely, a rougher film may lead to performance improvements, such as for a bacterial attachment surface that would benefit from maximizing the surface area. Thin film characterization of organic material blends could benefit from energy-filtered TEM (EFTEM), which has the potential to differentiate between organic molecules with similar electron densities [92]. Because TEM has a spatial resolution on the

order of a few nanometers, EFTEM could also provide a spatial map of the internal morphology to assist with device modeling. Finally, attempt to fabricate tandem organic photovoltaic devices. RIR-MAPLE has an advantage in heterostructure fabrication over solution-casting, so extrapolate that to its logical conclusion, which leads to devices with very many layers. Moreover, inorganic tandem photovoltaics currently produce efficiencies in excess of 40%. Therefore, higher efficiencies could be achieved through tandem devices in addition to improvements in materials engineering. It is two different approaches to the same goal.

Appendix A

Processing and Characterization Conditions

There is a very large parameter space associated with the RIR-MAPLE process: laser fluence, target-substrate distance, chamber pressure, laser repetition rate, target chemistry, substrate temperature, target rotation rate, substrate rotation rate, and others all affect the outcome of the thin film deposited. Additionally, there is a multitude of characterization techniques used to probe the resultant films. This appendix describes the conditions associated with fabricating and characterizing the thin films and devices produced in this work.

Unless noted, the conditions for the RIR-MAPLE depositions presented in this dissertation are as follows: 7 cm TS distance, 1E-3 wt% SDS surfactant added to the deionized water, controlled 25 °C in-situ substrate temperature, a 90 μs laser pulse at 2 Hz laser repetition rate, 10-100 μTorr chamber pressure, and laser pulse irradiance of 1.45-1.60 J/cm^2. These are parameters that have been found to give the best results.

All polymers in this work were used as-received from the manufacturer. All molecular weights of the PS, PMMA, and P3HT polymers were purchased from

Sigma-Aldrich. The MEH-PPV was purchased from American Dye Source.

For GPC measurements completed in Chapter 2, the polymer films deposited by RIR-MAPLE onto glass slides were prepared by dissolution in tetrahydrofuran (THF) and then by isolating the polymer for molecular weight measurement using standard rotary evaporator techniques. Clean THF was mixed with the polymer in an amount to achieve 2 mg/ml for GPC analysis. Only 200 μL of the polymer solution was injected into the GPC system to reduce peak broadening. GPC analysis was carried out on the following equipment: Optilab DSP Interferometric Refractometer and Dawn EOS-Enhanced Optical System, both from Wyatt Technology. The polymer was separated in a PLgel, 5 μm, 104 Å column from Agilent Technologies, using inhibitor-free THF as the mobile phase. The system was able to measure an approximate range of Mw between 104-106 g/mol (Da) with a light scattering wavelength of $\lambda = 690$ nm. ASTRA V software, version 5.3.4.16 (Wyatt Technology), was used for data analysis. The values of the refractive index increment, dn/dc, using THF as the mobile phase were determined after injecting a known amount of polymer: PMMA dn/dc = 0.088 [93], P3HT dn/dc = 0.285 [94], and MEH-PPV dn/dc = 0.293; when possible, these values have been confirmed from the literature. GPC samples were measured within one day after removal from vacuum.

For the molecular weight study in Chapter 2, ^{1}H NMR spectra were taken on a Varian Inova 400 MHz spectrometer. Sample preparation took place in a chemical fume hood. Samples were dissolved in chloroform-d and injected into Wilmad-LabGlass Pyrex 5 nm tubes for testing. Final spectra were an average of 64 runs on samples that were exposed to atmosphere for less than one day. FTIR spectra were taken on a Thermo Electron Nicolet 8700 spectrometer with 1.9 cm^{-1} wavenumber resolution. The films had been deposited onto undoped silicon and were measured in transmission mode under a nitrogen atmosphere at room temperature. All RIR-MAPLE films were measured by FTIR within one hour of removal from the vacuum

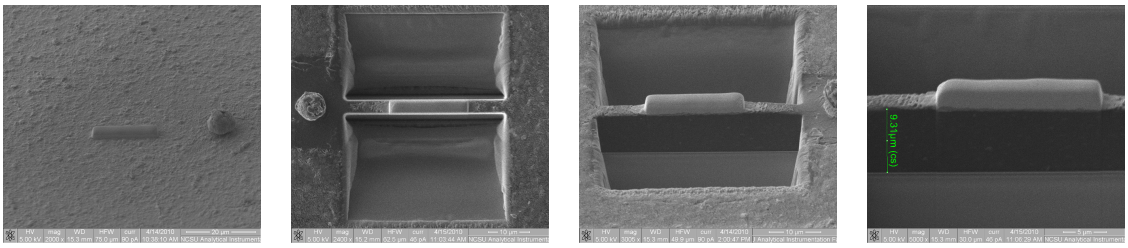

FIGURE A.1: SEM images of the FIB milling process (l to r): (a) Sample surface coated with AuPd and Pt bar. (b) Top view of sample after coarse milling. (c) An oblique view of milled sample shows the vertical slice; the polymer (dark) and glass (light) substrate layers are distinguishable. (d) Total sample thickness measures 9.31 μm.

system. Until ready for measurement, samples were kept in plastic clamshell cases that were wrapped in aluminum foil to shield them from ambient light. The P3HT and MEH-PPV samples were characterized by FTIR within one hour of deposition in order to minimize contact both with the atmosphere and with light sources.

For the cross-sectional TEM section, the samples were prepared as follows using the FIB milling process. This process was originally developed for preparation of inorganic materials, which tend to exhibit higher levels of hardness than the organic polymers currently being investigated. Therefore, it is more difficult to use the FIB milling process with organic thin films without some sample damage.

The organometallic deposition process occurs as follows: a needle supplies a gaseous source of Pt/C near the surface of the sample; an electron beam impinges on the gas and knocks the platinum onto the surface while the carbon is pumped away; there is usually some residual carbon mixed in at the deposition site, but it is negligible. The deposited platinum bar, shown in Figure A.1, has dimensions of 18 μm (L) x 3 μm (W) x 3 μm (H). The purpose of the platinum is to protect the material that will be analyzed and to provide a place where the FIB-etched slice can be lifted out of the bulk sample after the milling is finished.

During FIB milling, a focused ion beam of Gallium ions (Ga^+) impinges on the

surface of the sample at the desired location. The Au/Pd covering the surface of the sample dispels charge that may build up due to the Ga^+ ions. Two pits are created, as seen in Figures A.1(b) and (c), one on either side of a 2-3 μm thick slice. The pits completely penetrate the deposited sample and partially penetrate the substrate. In Figure A.1(d), the total thickness of the depositions atop the substrate is shown to be 9.31 μm, which includes the drop-cast polymer, the RIR-MAPLE-deposited polymer and the sputtered Au/Pd layers.

As the FIB milling moves closer to the sample slice, the rate of milling is decreased to minimize the potential damage to the slice. Coarse material removal occurs at 18 μm/hr at a beam voltage of 30 kV and a beam current of 20 nA. Finer removal occurs at a rate of 3 μm/hr at a beam voltage of 30 kV and a beam current of 7 nA. Near the Pt bar (i.e. near the sample slice), a much slower, finer removal rate can be utilized at a beam voltage of 5 kV and a beam current of 90 pA. The sample slice is thinned to the order of hundreds of nanometers thick. Two slits are vertically cut from the bottom of the slice at either end of the slice so that what remains resembles a flag on a horizontal pole. A stylus is attached to the Pt bar and the final two cuts are made to free the slice from the bulk sample. The slice is then placed on a carbon TEM grid consisting of a comb of open-ended bars and is further thinned in situ to a final thickness of approximately 100 nm for TEM imaging.

For the cross-sectional TEM and anti-reflection coatings sections, the TEM images were taken on an FEI Tecnai G2 Twin microscope at a tension of 200 kV. TEM grids were dipped in a 1 wt% solution of PMMA (350 kDa) in trichloroethylene to provide a non-staining scaffold film on which to deposit the PS:PMMA films.

Film thicknesses throughout this work were generally determined from either AFM images or via a profilometer. An AlphaStep IQ was used for the profilometer measurements. All AFM images were taken on a Digital Instruments Dimension 3100 microscope using Veeco TESP tips with a spring constant of either 42 N/m

or 0.5 N/m. The AFM measurements were conducted using a Digital Instruments Dimension 3100 with Bruker TESP silicon tips with 42 N/m spring constant and 8-12 nm tip radius.

The SEM measurements in Chapter 4 were conducted using an FEI XL30 FEG at an accelerating voltage of 3 kV at a working distance of 5-6 mm and 300,000 times magnification. An attempt to coat the films in gold resulted in the gold filling the pores of the films. Therefore, the images were taken with the native films, but the silicon substrates were grounded with copper tape to reduce charge accumulation.

Optical characterization of the RIR-MAPLE films from Chapter 4 was done at the University of Texas at Arlington in collaboration with the Zhou group. Spectral reflectance was measured by an integrating sphere with a beam spot of 1 mm diameter at normal incidence. The reflectivity was measured at normal incidence by a JASCO V-570 spectrophotometer with an attached integrating sphere that measures the light reflected by the sample from all directions.

The refractive index for all films in Chapter 4 was measured using an ellipsometer with a beam spot of 400 μm diameter. An HS-190, variable angle spectroscopic ellipsometer (VASE) by J. A. Woollam Co. was used to extract the ellipsometric data in the wavelength range 400-800 nm in steps of 10 nm. The spectroscopic ellipsometric data was averaged over multiple angles of incidence from 65°-75° in steps of 5°. WVASE32^{TM} software was used to model the optical constants of film thickness and refractive index of the porous homopolymer films.

In Chapters 3 and 5, GIWAXS data originate as two-dimensional (2D) images. These 2D images of the scattering profiles were reduced to 1D plots by integrating the scattering intensities in the IP and OOP directions, which are defined as the perpendicular direction ±20°, and the IP direction +20°. Figure A.2 shows a screen shot of the SAXSgui (SAXSLab) software that is used to process the GIWAXS data. The software generates an azimuthal angle versus q plot from the original polar plot.

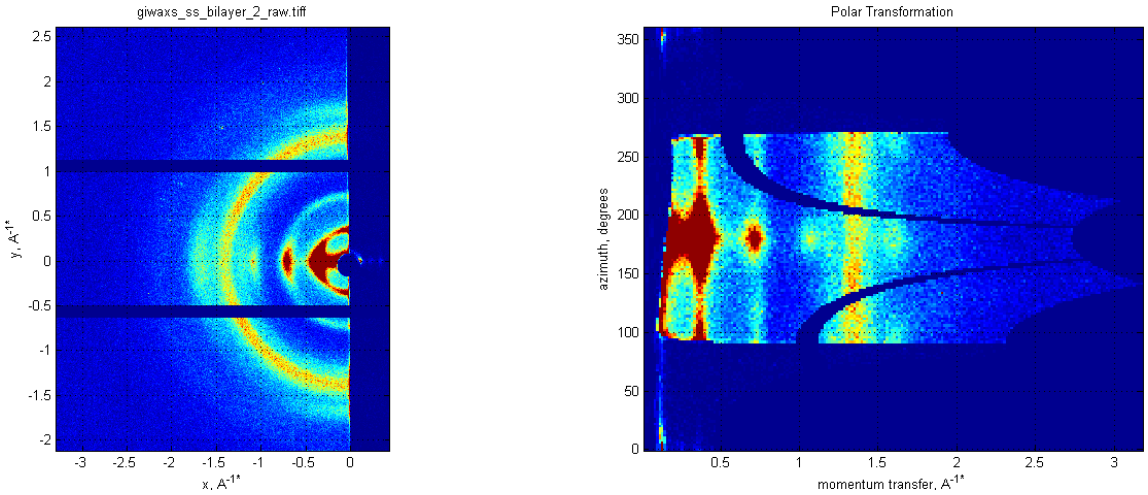

FIGURE A.2: Raw image of a GIWAXS 2D scattering plot on the left, which is transformed to a plot of azimuthal angle vs. q (momentum transfer) via SAXSgui software (SAXSLab). The OOP direction is located at 180°; the IP direction is located at 90° and 270°. The horizontal bars in the raw image represent boundaries between the active regions of the x-ray detector.

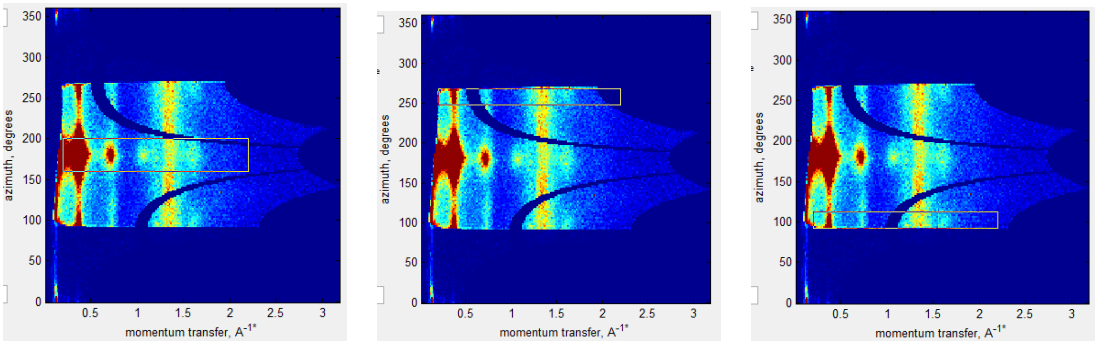

FIGURE A.3: (left) OOP area of integration; (center) 1st IP area of integration; (right) 2nd IP area of integration. The two IP integrations are averaged where they overlap, while the data are discarded in the dropout regions.

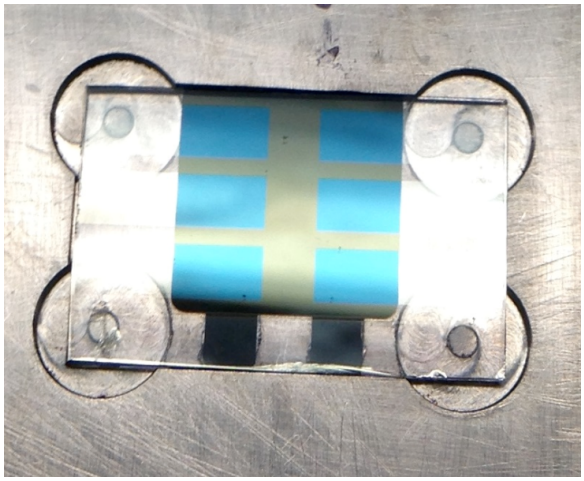

FIGURE A.4: Patterned ITO glass substrate seated in the cathode deposition mask. The six ITO strips are clearly visible against the square active region deposited by RIR-MAPLE. The two cathode strips can be seen as the vertical openings beneath the substrate that each overlaps three ITO anodes. There is another ITO strip that runs the length of the substrate at the bottom and acts to connect the deposited cathodes together.

The linear plot allows patterns to be more easily discovered. It also allows integration of an angular region to be more easily defined with a simple box. Figure A.3 shows the three different areas that are integrated from the 2D image to create the 1D traces. Two IP areas are captured and averaged due to the splitting of the IP direction into 90° and 270° locations. The OOP direction is defined as 180 degrees.

The OPV samples were prepared as follows. Patterned indium tin oxide (ITO) glass substrates were purchased from Xinyan Technology, Ltd. Each glass substrate was 25 mm x 16 mm x 1.1 mm and contained 10 Ω/square ITO patterned such that 6 separate devices could be fabricated (Figure A.4). While all anodes consisted of separate ITO contact strips, the top cathode was deposited in two strips perpendicular to the anodes. Each cathode created three 3 mm x 3 mm pixels, each of which was a separate device, that were connected in parallel; a separate ITO strip connected the two cathodes together at the bottom edge of the chip.

The nonconductive side of the substrate was marked with a diamond scribe for identification during processing. The substrates were cleaned in the Duke SMIF clean room using the following procedure. The substrates were placed in a single layer in a glass Petri dish and sonicated for 5 minutes each in acetone, then isopropanol, and then filtered, deionized (DI) water. The substrates were dried with filtered nitrogen gas between each solvent step. After the DI water rinse, the substrates were ozone plasma-ashed (Emitech, model K-1050X) for 4 minutes at 100 W to remove any remaining organic material. Finally, the substrates were rinsed in DI water and dried with filtered nitrogen gas.

To smooth out the roughness of the ITO surface, aqueous poly(3,4-ethylenedioxythiophene) poly(styrenesulfonate), or PEDOT:PSS, (Heraeus Clevios^{TM} PVP AI 4083) was spincast in the clean room in air on top of the ITO. Typical spinning parameters of 5000 RPM for 30 seconds produced PEDOT films of thickness between 30-40 nm. The PEDOT:PSS films were annealed in air on a 120°C hot plate in the clean room for five minutes to remove any excess water from the films. The PEDOT-covered substrates were then transported out of the clean room to a vacuum box in the group lab until deposition of the active layer materials.

The P3HT specifications (purchased from Sigma-Aldrich and used as received without any further processing) listed the regioregularity as 98% head-to-tail as measured by ^{1}H NMR. The purity was listed as 99.995% based on trace metals analysis, and the number-averaged molecular weight was M_n = 70.52 kDa, with PDI = 1.7, which gives M_w = 119.9 kDa. The PCBM (purchased from Sigma-Aldrich and used as received without any further processing) purity was reported to be 99.5%.

Deposition of the top contact involved the use of a thermal evaporator located within the nitrogen glove box system located at the NCSU Nanofabrication Facility (NNF), a shared instrumentation facility at North Carolina State University (NC State). A small gas-tight, amber-colored travel box was purged until a humidity

sensor saturated on the low end, generally taking an hour to complete. The amber coloring blocked UV radiation from entering the box. The OPV samples were then removed from the vacuum storage box, which is evacuated by a hydrocarbon oil pump to the milliTorr range, and placed in the purged amber box for travel to NC State. A small tank of ultra-high purity nitrogen gas was used to purge the box during the 35-50 minutes it takes to drive to NC State. The samples were immediately removed from the amber box and placed in the nitrogen glove box system at NNF.

A stainless steel shadow mask was used to thermally evaporate the cathode material, which was aluminum, atop the active region. One recessed substrate position is shown in Figure A.4. The two vertical cathode windows in the stainless steel mask can be clearly seen near the center of the image, overlapping the horizontal ITO bars. The intersection of the cathode and the ITO anode creates a 3 mm x 3 mm pixel, of which each is a separate OPV device. The cathode was deposited at a rate of 0.2-0.4 nm/sec to a total thickness of 100-150 nm. A thicker top layer is required for these devices compared with spin-casting due to the larger surface roughness of the RIR-MAPLE films.

After cathode deposition, the devices were removed from the evaporator via the glove box to preclude exposure to atmosphere. A proprietary light-curable epoxy (Ossila, Ltd., part #131) and thin glass cover slips were used to encapsulate the finished devices while in the nitrogen atmosphere. This step was taken to avoid further exposure to atmosphere during transport back to Duke and to stabilize the response for the optoelectronic characterizations (IV and EQE) that occurred in atmosphere.

IV measurements of all OPV devices in this work were completed using a Keithley 4200-SCS semiconductor analyzer. The solar cell temperature was measured via a thermocouple in contact with the reference cell. A mask that rejects all light except a 9 mm^2 square area is placed in the path of the beam in order to separately

illuminate each of the six 9 mm^2 square pixels on each substrate. The reference cell is then placed directly beneath the mask to ensure that the spatially inhomogeneous irradiance that is output by the solar simulator is equivalent to 1 sun through the mask. The output of the reference cell was factory-calibrated to 1 V/sun for an active area of 20 mm x 20 mm. However, the top contact of the cell measures 1 mm x 20 mm, thereby reducing the active area to 19 mm x 20 mm. The ratio of 9 mm^2 to 380 mm^2 is 0.0237, which is multiplied by 1 V/sun to give 0.0237 volts output at 1 sun irradiance. Therefore, the reference cell reads this value when the solar simulator is properly adjusted to 1 sun.

To measure the IV characteristic of one OPV device, the active area of the test cell is mounted at the same height as the reference cell beneath the mask. Illumination of the P3HT:PCBM active region is through the glass substrate and the transparent ITO contact. Electrical connections are made to the cathode and anode of the test cell using toothless copper alligator clips to increase the surface area of the contact. A four-probe measurement is used to remove the effects of lead resistance in the measurement probes of the Keithley 4200-SCS [95]. The test sample holder is mounted to an XY-axis stage to adjust the position of the test cell beneath the mask. Alignment of the test cell is completed by monitoring the current output of the test cell under illumination in real time and adjusting the position with the XY-axis stage to maximize the output current. The underlying assumption of this method is that the test cell produces its maximum current when the top contact is spatially in line with the solar simulator photon flux. This is a reasonable assumption because the path to the contact of any free charge is otherwise increased, greatly increasing the probability that the charge will recombine before reaching the contact.

The EQE data were taken on an Oriel monochromator-based EQE system with a 500 W Xe light source. A 30-Hz chopper was placed between the light source and the monochromator. The output of the test device was fed into an Oriel Merlin

lock-in amplifier to provide rejection of any background DC light. Additionally, a series of optical lowpass filters provided rejection of higher energy photons due to the monochromator gratings. For a spectral measurement encompassing the range λ = 300-800 nm, three different set-ups were used: no filter was used for λ = 300-340 nm; a filter with a cut-off wavelength of 340 nm was used for λ = 340-600 nm; and, a filter with a cut-off wavelength of 600 nm was used for the range λ = 600-800 nm. The entire system was controlled through Oriel's TracQ Basic software. A 20 mm x 20 mm calibrated silicon detector provided a measurement of the spectral power output by the EQE system onto the test devices. However, the output light was reduced to the size of the test device at 3 mm x 3 mm square so that the optical power measured by the silicon cell would be a direct measurement of the responsive area of the test device. Although Xe sources are widely used to mimic the solar spectrum, they require proper focusing of the reflecting mirror relative to the lamp filament to achieve the correct irradiance desired; the result is that the spectral and irradiant spatial homogeneities in the plane perpendicular to the photon direction are often limited. Indeed, this was the case with our system. Prior to masking the EQE system output to 9 mm^2, the measured EQE of a particular device was dependent upon spatial placement within the output beam. This was corrected after the light was masked.

An EQE measurement was completed as follows. After the Xe lamp had been on for a minimum of 30 minutes to warm up, the calibrated silicon cell was positioned in the output beam. A reference spectral response curve was measured from the current output of the cell, which was amplified and converted to a voltage signal through a transimpedance amplifier built into the reference cell housing with a gain of g_{ref} = 1E6 V/A. A second spectral response curve was taken at the beginning of a measurement session with the EQE system shutter closed to ensure that the noise floor was below the signal level, which was always true for the data presented here.

The spectral responsivity of the silicon cell provided a conversion of the reference curve to the optical power of the photons output by the EQE system. Next the silicon cell was replaced with a test cell at the identical spatial location of the reference cell. This was accomplished with a 3-axis translational stage set-up with micrometer precision. The monochromator was set to output $\lambda = 555$ nm, near the peak of P3HT absorbance. The real time test cell current was monitored on the lock-in amplifier while the micrometer positioners along the axes parallel to the test cell plane were actuated to maximize the test cell current prior to a full spectrum being taken, again, assuming that the maximum current manifested at maximum cathode illumination. The transimpedance gain was again set at $g_{test} = 1E6$ V/A on the light bias amplifier (Oriel, part #70714) connected to the test cell unit, which provided ample signal-to-noise, and allowed for direct comparison of the reference output. A spectral response curve was taken for the range $\lambda = 300$-800 nm in 2 nm increments. The EQE of the test device could then be calculated according to the following equation provided by the manufacturer, Newport Oriel:

$$EQE(\%) = 2.2(100\%)\frac{g_{ref}}{g_{test}}\frac{hc}{e\lambda}\frac{R_{ref}(\lambda)}{S_{ref}(\lambda)}S_{test}(\lambda) \tag{A.1}$$

where the factor 2.2 is an empirical constant from the manufacturer, h is Planck's constant in J·s, c is the speed of light in m/s, e is the elementary charge in C, λ is the wavelength of light in m, $R_{ref}(\lambda)$ is the reference silicon detector spectral responsivity in A/W, $S_{ref}(\lambda)$ is the spectral response of the reference silicon detector in V, and S_{test} (λ) is the spectral response of the OPV test cell in volts.

The thermally-evaporated cathode for the OPV devices took three forms during the course of several studies: 100-150 nm Al; 50 nm of Ca, followed by 100 nm of Al; and, 1 nm LiF, followed by 150 nm Al. It was found that the best performance resulted from the use of Al alone as a cathode.

The surface roughness explains the superiority of Al as the cathode contact. Spin-

cast device show an improvement in performance with either a Ca/Al or a LiF/Al contact, both for the same reason. The Ca provides a lower work function that blocks holes and facilitates electron transport to the Al. Similarly, LiF of thickness 1 nm or less provides an interface dipole that effectively lowers the work function locally at the interface, which affects the carriers in a manner like the Ca layer. However, spin-cast films tend to be very smooth so that the interface between the active region and the cathode can be assumed to be featureless.

The rougher surface provided by RIR-MAPLE requires more material to ensure full coverage of the entire surface due the hills and valleys of the local surface. Therefore, 1 nm of LiF deposited on a surface of root-mean squared (RMS) roughness of $R_q = 30$ nm is unlikely to provide complete coverage of the active region prior to the deposition of the Al. In fact, this is what we observed. The LiF/Al devices showed a dramatic decrease in performance compared with Al alone. The Ca/Al devices fared better due to the increased thickness of the Ca layer prior to Al deposition, but they were overall poorer performers than the devices with Al alone. The results were highly dependent on device structure and annealing conditions, further pointing to surface roughness as the primary factor.

Appendix B

Hansen Solubility Parameters

Emulsion-based RIR-MAPLE requires a mixture of solvents and organic materials that may or may not be miscible with each other. The Hansen solubility parameters are useful tools that aid in *a priori* determination of "good" or miscible solvents to mix to create a good target emulsion. The treatment here follows information found in references [96, 97]. The overall solubility parameter, δ, is derived from the cohesive energy density of a given material, and is also known as the Hildebrand solubility parameter. Charles Hansen divided this parameter into three components, two parameters based on the dispersive and polar van der Waals forces and the other a hydrogen bonding parameter. The relationship is given by:

$$\delta^2 = \delta_d^2 + \delta_p^2 + \delta_h^2 \tag{B.1}$$

where δ_d is the dispersive parameter, δ_p is the polar parameter, and δ_h is the hydrogen bonding parameter.

Another material property, the solubility radius, R_0, can be defined for a material. The solubility radius is an experimentally determined value in three-dimensional Hansen parameter space (i.e. dispersive-polar-hydrogen bonding axes) that is a

Table B.1: Hansen solubility parameters and radii for the polymers and small molecules used in this work.

Units are $(J/cm^3)^{1/2}$	Solubility Parameter	Dispersion Force	Polar	Hydrogen-Bonding	Solubility Radius
Polymer	δ	δ_d	δ_p	δ_h	R_0
PS	**22.5**	21.3	5.8	4.3	12.7
PMMA	**22.6**	18.6	10.5	7.5	8.6
$PC_{61}BM$	**20.4**	3.5	7.2	21.9	7.5
P3HT	**20.0**	18.5	5.3	5.3	2.7
MEH-PPV	**19.4**	18.6	2.4	5.0	*

Table B.2: Hansen solubility parameters for solvents used in this work.

Units are $(J/cm^3)^{1/2}$	Solubility Parameter	Dispersion Force	Polar	Hydrogen-Bonding
Polymer	δ	δ_d	δ_p	δ_h
Toluene	**18.2**	18.0	1.4	2.0
Trichloroethylene	**19.0**	18.0	3.1	5.3
Chloroform	**19.0**	17.9	3.1	5.7
Tetrahydrofuran	**19.5**	16.8	5.7	8.0
Chlorobenzene	**19.6**	19.0	4.3	2.0
Ortho-Dichlorobenzene	**20.5**	19.2	6.3	3.3
Benzyl Alcohol	**23.8**	18.4	6.3	13.7
Phenol	**24.1**	18.0	5.9	14.9
Water	**47.8**	15.5	16.0	42.3

guideline choosing miscible solvents for the material. The solubility radius indicates the approximate distance in parameter space that can be traversed before the material becomes insoluble. It is a quantification of the old saying that "like dissolves like" because if the solvent parameters are too different from those of the organic material, the two will be immiscible. Tables B.1 and B.2 summarize the Hansen solubility parameters and radii for the materials used in this work.

To calculate the difference in parameter space between two materials, the follow-

ing empirically-derived equation is required:

$$(R_a)^2 = 4(\delta_{d1} - \delta_{d2})^2 + (\delta_{p1} - \delta_{p2})^2 + (\delta_{h1} - \delta_{h2})^2 \tag{B.2}$$

where R_a represents the solubility difference in Hansen parameter space, the subscripts, d, p, and h, represent the dispersive, polar, and hydrogen bonding components, respectively. The subscripts 1 and 2 represent material 1 (e.g. polymer) and material 2 (e.g. solvent), respectively. The relative energy difference (RED) can then be calculated by taking the ratio RED $= R_a/R_0$. When the RED value is less than or equal to one, the two materials are likely miscible; then the RED value is greater than one, the two materials are likely immiscible. It is important to remember that the solubility radius is a guideline; a RED value greater than one may still give miscible results, and vice versa.

To determine the solubility parameters of a mixture of solvents, one can use a linear combination of the parameters for each solvent based on the volume fraction of each in the mixture:

$$\delta_{i,mix} = f\delta_{i,2} + (1 - f)\delta_{i,1} \tag{B.3}$$

where the i^{th} parameter of the mixture, $\delta_{i,mix}$, is given by the ith parameters of material 1, $\delta_{i,2}$, and material 2, $\delta_{i,2}$, and the volume fraction of material 1, f, and of material 2, $1 - f$.

A graphical example of this is shown in Figure B.1. When f equals zero, the RED values are those of the polymer in solvent 1 alone. When f equals one, the RED values are those of the polymer in solvent 2 alone. RED values at or below one represent likely miscibility.

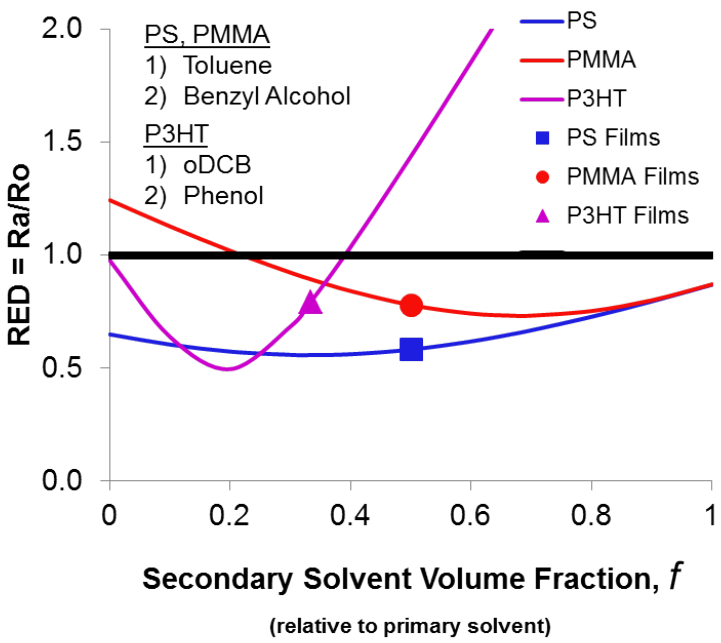

FIGURE B.1: Solubility determination of a polymer in a mixture of two solvents. A linear combination of the Hansen solubility parameters of the two solvents plotted versus the volume fraction of solvent 2 in a mixture with solvent 1 are used to determine the RED values (values at/below 1 indicate likely miscibility). The symbols indicate the values used for the majority of the films in this work.

Appendix C

RIR-MAPLE Parameter Study of P3HT

Emulsion-based RIR-MAPLE has a large parameter space that can be utilized to affect the outcome of deposited organic thin films. A study of the effects of varying the parameters on P3HT films was completed using the following RIR-MAPLE parameters.

Four target parameters were chosen:

1) Weight percent of polymer in primary solvent = P3HT wt% in trichloroethylene (TCE)
2) Secondary : primary solvent mass ratio = Phenol : TCE
3) Water : secondary solvent mass ratio = Water : Phenol
4) Weight percent of surfactant in deionized water = SDS wt% in Water

Four MAPLE process parameters were chosen:

1) Laser Fluence (mJ/cm^2)
2) *In situ* Substrate Temperature (°C)
3) Target to Substrate Distance (mm)
4) Chamber Pressure (Torr)

The following two tables of data represent P3HT films that were deposited using parameter values that were selected at random from a predefined range for each

Table C.1: P3HT films deposited by varying 8 RIR-MAPLE parameters at random within predefined parameter ranges. Samples 1-8.

INPUT PARAMETERS	S01	S02	S03	S04	S05	S06	S07	S08
Target: P3HT Polymer Weight Percent in TCE	0.5	0.01	0.1	0.1	4	0.01	0.01	1
Target: Phenol:P3HT Solution Mass Ratio	2:1	1:2	1:2	2:1	8:1	2:1	2:1	1:4
Target: Water:Phenol Mass Ratio	1:4	2:1	8:1	1:4	1:8	2:1	4:1	1:8
Target: Surfactant Weight Percent	0.2	0.2	0.01	0.1	0.001	0.2	0.01	0.2
MAPLE: Laser Panel Setting	6.5	7.5	6.5	6.5	6.5	6.5	8	8.5
MAPLE: Substrate Temperature (°C)	50	75	50	150	50	125	150	50
MAPLE: Substrate-Target Distance (mm)	65	56	44	60	52	40	44	70
MAPLE: Pressure (Torr)	1E-06	1E-05	1E-05	1E-01	1E+00	1E-03	1E-04	1E+00
OUTPUT PARAMETERS	S01	S02	S03	S04	S05	S06	S07	S08
Contiguous Film? (0 = no; 1 = yes)	0	1	1	1	0	1	1	1
AFM: Thickness (nm)	21.28	100.2	32.22	22.97	5.48	77.09	20.48	1530
AFM: Roughness, R_q (nm)	292	90.8	47.7	57.7	328	40.6	43.6	629
XRD: Peak 1 Location (degrees)	2.07	2.17	5.34	4.49	5.28	2.16	1.9	5.27
XRD: Peak 1 FWHM (degrees)	0.28	0.35	0.39	0.52	0.5	0.33	0.42	0.76
XRD: Peak 1 Relative Intensity	7.39	19.13	1.36	1.42	1.24	44.76	8.8	2.05
XRD: Peak 2 Location (degrees)	4.38	4.35	-	-	-	4.34	4.28	-
XRD: Peak 2 FWHM (degrees)	0.39	0.4	-	-	-	0.35	0.66	-
XRD: Peak 2 Relative Intensity	1.84	3.12	-	-	-	5.65	1.63	-
XRD: Peak 3 Location (degrees)	6.6	6.5	-	-	-	6.5	6.37	-
XRD: Peak 3 FWHM (degrees)	0.29	0.42	-	-	-	0.37	0.56	-
XRD: Peak 3 Relative Intensity	1.21	1.88	-	-	-	3.16	1.05	-

parameter. The output parameters were a mix of qualitative and quantitative. Characterization by AFM determined average thickness and roughness, but also a judgment as to whether the resulting deposition was in fact a contiguous film. In some cases, there was continuous material across the surface; in other cases, there were only granules of material scattered across the substrate. XRD was used to look for ordered structure within the resulting depositions.

Table C.2: P3HT films deposited by varying 8 RIR-MAPLE parameters at random within predefined parameter ranges. Samples 9-15.

INPUT PARAMETERS	S09	S10	S11	S12	S13	S14	S15
Target: P3HT Polymer Weight Percent in TCE	0.1	0.5	0.01	1	0.01	1.5	0.25
Target: Phenol:P3HT Solution Mass Ratio	8:1	1:1	1:4	1:4	1:2	1:2	1:1
Target: Water:Phenol Mass Ratio	4:1	1:4	8:1	4:1	2:1	1:2	1:4
Target: Surfactant Weight Percent	0.1	0.005	0.01	0.005	0.2	0.005	0.01
MAPLE: Laser Panel Setting	5	6	6.5	6	7.5	8	7
MAPLE: Substrate Temperature (°C)	25	200	100	25	75	175	100
MAPLE: Substrate-Target Distance (mm)	56	44	70	52	56	52	44
MAPLE: Pressure (Torr)	1E-03	1E+00	1E+01	1E-02	1E-05	1E-03	1E-02
OUTPUT PARAMETERS	S09	S10	S11	S12	S13	S14	S15
Contiguous Film? (0 = no; 1 = yes)	1	0	0	0	1	1	0
AFM: Thickness (nm)	8.81	19.5	0	4.14	133.3	2712	187
AFM: Roughness, R_q (nm)	11.9	141	41.2	142	61.3	1232	201
XRD: Peak 1 Location (degrees)	2.08	5.19	-	2.78	2.16	5.22	5.03
XRD: Peak 1 FWHM (degrees)	0.41	0.73	-	0.67	0.32	0.8	0.69
XRD: Peak 1 Relative Intensity	14.24	1.25	-	4.1	28.83	3.35	1.29
XRD: Peak 2 Location (degrees)	4.37	-	-	5.44	4.34	-	-
XRD: Peak 2 FWHM (degrees)	0.34	-	-	0.38	0.35	-	-
XRD: Peak 2 Relative Intensity	1.47	-	-	1.21	3.5	-	-
XRD: Peak 3 Location (degrees)	6.43	-	-	-	6.51	-	-
XRD: Peak 3 FWHM (degrees)	0.35	-	-	-	0.36	-	-
XRD: Peak 3 Relative Intensity	0.83	-	-	-	2.16	-	-

Bibliography

[1] ASTM, "G-173-03: Standard tables for reference solar spectral irradiances: Direct normal and hemispherical on 37° tilted surface," 2003.

[2] A. Inigo, C. Chang, W. Fann, J. White, Y. S. Huang, U. S. Jeng, H. Sheu, K. Y. Peng, and S. A. Chen, "Enhanced hole mobility in poly-(2-methoxy-5-(2-ethylhexoxy)-1,4-phenylenevinylene) by elimination of nanometer-sized domains," *Advanced Materials*, vol. 17, no. 15, pp. 1835–1838, 2005.

[3] Y. Shi, J. Liu, and Y. Yang, "Device performance and polymer morphology in polymer light emitting diodes: The control of thin film morphology and device quantum efficiency," *Journal of Applied Physics*, vol. 87, no. 9, pp. 4254–4263, 2000.

[4] H. Sirringhaus, T. Kawase, R. H. Friend, T. Shimoda, M. Inbasekaran, W. Wu, and E. P. Woo, "High-resolution inkjet printing of all-polymer transistor circuits," *Science*, vol. 290, no. 5499, pp. 2123–2126, 2000.

[5] M. I. Sluch, C. Pearson, M. C. Petty, M. Halim, and I. D. W. Samuel, "Photo- and electroluminescence of poly(2-methoxy,5-(2'-ethylhexyloxy)-p-phenylene vinylene) Langmuir-Blodgett films," *Synthetic Metals*, vol. 94, no. 3, pp. 285–289, 1998.

[6] R. Saf, M. Goriup, T. Steindl, T. E. Hamedinger, D. Sandholzer, and G. Hayn, "Thin organic films by atmospheric-pressure ion deposition," *Nat Mater*, vol. 3, no. 5, pp. 323–329.

[7] D. B. Chrisey, A. Pique, R. A. McGill, J. S. Horwitz, B. R. Ringeisen, D. M. Bubb, and P. K. Wu, "Laser deposition of polymer and biomaterial films," *Chemical Reviews*, vol. 103, no. 2, pp. 553–576, 2003.

[8] R. Frycek, M. Jelnek, T. Kocourek, P. Fitl, M. Vrnata, V. Myslk, and M. Vrbov, "Thin organic layers prepared by MAPLE for gas sensor application," *Thin Solid Films*, vol. 495, no. 1-2, pp. 308–311, 2006.

[9] B. R. Ringeisen, D. B. Chrisey, A. Piqu, H. D. Young, R. Modi, M. Bucaro, J. Jones-Meehan, and B. J. Spargo, "Generation of mesoscopic patterns of

viable Escherichia coli by ambient laser transfer," *Biomaterials*, vol. 23, no. 1, pp. 161–166, 2002.

[10] C. E. Allmond, A. T. Sellinger, K. Gogick, and J. M. Fitz-Gerald, "Photochemical synthesis and deposition of noble metal nanoparticles," *Applied Physics A: Materials Science & Processing*, vol. 86, no. 4, pp. 477–480, 2007.

[11] R. Pate, K. R. Lantz, and A. D. Stiff-Roberts, "Tabletop resonant infrared matrix-assisted pulsed laser evaporation of light-emitting organic thin films," *IEEE Journal of Selected Topics in Quantum Electronics*, vol. 14, no. 4, pp. 1022–1030, 2008.

[12] A. Piqué, R. A. McGill, D. B. Chrisey, D. Leonhardt, T. E. Mslna, B. J. Spargo, J. H. Callahan, R. W. Vachet, R. Chung, and M. A. Bucaro, "Growth of organic thin films by the matrix assisted pulsed laser evaporation (MAPLE) technique," *Thin Solid Films*, vol. 355-356, pp. 536–541, 1999.

[13] D. M. Bubb, P. K. Wu, J. S. Horwitz, J. H. Callahan, M. Galicia, A. Vertes, R. A. McGill, E. J. Houser, B. R. Ringeisen, and D. B. Chrisey, "The effect of the matrix on film properties in matrix-assisted pulsed laser evaporation," *Journal of Applied Physics*, vol. 91, no. 4, pp. 2055–2058, 2002.

[14] D. M. Bubb, B. Toftmann, J. R. F. Haglund, J. S. Horwitz, M. R. Papantonakis, R. A. McGill, P. W. Wu, and D. B. Chrisey, "Resonant infrared pulsed laser deposition of thin biodegradable polymer films," *Applied Physics A: Materials Science & Processing*, vol. 74, no. 1, pp. 123–125, 2002.

[15] D. M. Bubb, S. M. O'Malley, C. Antonacci, D. Simonson, and R. A. McGill, "Matrix-assisted laser deposition of a sorbent oligomer using an infrared laser," *Journal of Applied Physics*, vol. 95, no. 4, pp. 2175–2177, 2004.

[16] B. Toftmann, M. R. Papantonakis, R. C. Y. Auyeung, W. Kim, S. M. O'Malley, D. M. Bubb, J. S. Horwitz, J. Schou, P. M. Johansen, and R. F. Haglund, "UV and RIR matrix assisted pulsed laser deposition of organic MEH-PPV films," *Thin Solid Films*, vol. 453-454, pp. 177–181, 2004.

[17] D. Bubb, J. Corgan, S. Yi, M. Khan, L. Hughes, U. Gurudas, M. Papantonakis, and R. McGill, "An experimental investigation of inhomogeneities in resonant infrared matrix-assisted pulsed-laser deposited thin polymer films," *Applied Physics A: Materials Science & Processing*, vol. 100, no. 2, pp. 523–531, 2010.

[18] R. D. Torres, S. L. Johnson, R. F. Haglund, J. Hwang, P. L. Burn, and P. H. Holloway, "Mechanisms of resonant infrared matrix-assisted pulsed laser evaporation," *Critical Reviews in Solid State and Materials Sciences*, vol. 36, no. 1, pp. 16–45, 2011.

[19] S. L. Johnson, H. K. Park, and R. F. Haglund Jr, "Properties of conductive polymer films deposited by infrared laser ablation," *Applied Surface Science*, vol. 253, no. 15, pp. 6430–6434, 2007.

[20] R. Pate, R. McCormick, L. Chen, W. Zhou, and A. Stiff-Roberts, "RIR-MAPLE deposition of conjugated polymers for application to optoelectronic devices," *Applied Physics A: Materials Science & Processing*, vol. 105, pp. 555–563, 2011.

[21] R. Pate, K. R. Lantz, A. Dhawan, T. Vo-Dinh, and A. D. Stiff-Roberts, "Resonant infrared matrix-assisted pulsed laser evaporation of inorganic nanoparticles and organic/inorganic hybrid nanocomposites," *AIP Conference Proceedings*, vol. 1278, no. 1, pp. 812–823, 2010.

[22] R. Pate, K. R. Lantz, and A. D. Stiff-Roberts, "Resonant infrared matrix-assisted pulsed laser evaporation of CdSe colloidal quantum dot/poly[2-methoxy-5-(2'-ethylhexyloxy)-1,4-(1-cyano vinylene)phenylene] hybrid nanocomposite thin films," *Thin Solid Films*, vol. 517, no. 24, pp. 6798–6802, 2009.

[23] R. Pate and A. D. Stiff-Roberts, "The impact of laser-target absorption depth on the surface and internal morphology of matrix-assisted pulsed laser evaporated conjugated polymer thin films," *Chemical Physics Letters*, vol. 477, no. 4-6, pp. 406–410, 2009.

[24] A. D. Stiff-Roberts, R. Pate, R. McCormick, and K. R. Lantz, "RIR-MAPLE deposition of conjugated polymers and hybrid nanocomposites for application to optoelectronic devices," *AIP Conference Proceedings*, vol. 1464, no. 1, pp. 347–357, 2012.

[25] R. Cristescu, D. Mihaiescu, G. Socol, I. Stamatin, I. N. Mihailescu, and D. B. Chrisey, "Deposition of biopolymer thin films by matrix assisted pulsed laser evaporation," *Applied Physics A: Materials Science & Processing*, vol. 79, no. 4, pp. 1023–1026, 2004.

[26] A. Caricato, G. Leggieri, M. Martino, A. Vantaggiato, D. Valerini, A. Cret, M. Lomascolo, M. Manera, R. Rella, and M. Anni, "Dependence of the surface roughness of MAPLE-deposited films on the solvent parameters," *Applied Physics A: Materials Science & Processing*, vol. 101, no. 4, pp. 759–764, 2010.

[27] C. L. Chochos and S. A. Choulis, "How the structural deviations on the backbone of conjugated polymers influence their optoelectronic properties and photovoltaic performance," *Progress in Polymer Science*, vol. 36, no. 10, pp. 1326–1414, 2011.

[28] R. Kline, M. McGehee, E. Kadnikova, J. Liu, and J. Frchet, "Controlling the field-effect mobility of regioregular polythiophene by changing the molecular weight," *Advanced Materials*, vol. 15, no. 18, pp. 1519–1522, 2003.

[29] A. Zen, J. Pflaum, S. Hirschmann, W. Zhuang, F. Jaiser, U. Asawapirom, J. Rabe, U. Scherf, and D. Neher, "Effect of molecular weight and annealing of poly(3-hexylthiophene)s on the performance of organic field-effect transistors," *Advanced Functional Materials*, vol. 14, no. 8, pp. 757–764, 2004.

[30] P. Schilinsky, U. Asawapirom, U. Scherf, M. Biele, and C. J. Brabec, "Influence of the molecular weight of poly(3-hexylthiophene) on the performance of bulk heterojunction solar cells," *Chemistry of Materials*, vol. 17, no. 8, pp. 2175–2180, 2005.

[31] K. Hosoi, T. Mori, T. Mizutani, T. Yamamoto, and N. Kitamura, "Effects of molecular weight on polyfluorene-based polymeric light emitting diodes," *Thin Solid Films*, vol. 438-439, no. 0, pp. 201–205, 2003.

[32] A. L. Mercado, C. E. Allmond, J. G. Hoekstra, and J. M. Fitz-Gerald, "Pulsed laser deposition vs. matrix assisted pulsed laser evaporation for growth of biodegradable polymer thin films," *Applied Physics A: Materials Science & Processing*, vol. 81, no. 3, pp. 591–599, 2005.

[33] J. M. Fitz-Gerald, G. Jennings, R. Johnson, and C. L. Fraser, "Matrix assisted pulsed laser deposition of light emitting polymer thin films," *Applied Physics A: Materials Science & Processing*, vol. 80, no. 5, pp. 1109–1112, 2005.

[34] A. T. Sellinger, A. H. Martin, and J. M. Fitz-Gerald, "Effect of substrate temperature on poly(methyl methacrylate) nanocomposite thin films deposited by matrix assisted pulsed laser evaporation," *Thin Solid Films*, vol. 516, no. 18, pp. 6033–6040, 2008.

[35] P. J. Wyatt, "Light scattering and the absolute characterization of macromolecules," *Analytica Chimica Acta*, vol. 272, no. 1, pp. 1–40, 1993.

[36] M. S. Abdou and S. Holdcroft, "Solid-state photochemistry of π-conjugated poly(3-alkylthiophenes)," *Canadian Journal of Chemistry*, vol. 73, no. 11, pp. 1893–1901, 1995.

[37] P. A. Mirau, *A practical guide to understanding the NMR of polymers*. Hoboken, N.J.: Wiley-Interscience, 2005.

[38] T.-A. Chen, X. Wu, and R. D. Rieke, "Regiocontrolled synthesis of poly(3-alkylthiophenes) mediated by rieke zinc: Their characterization and solid-state properties," *Journal of the American Chemical Society*, vol. 117, no. 1, pp. 233–244, 1995.

[39] M. H. Rahman, H.-L. Chen, S.-A. Chen, and P. P. J. Chu, "^{1}H NMR spectroscopic study of the solution structure of a conjugated polymer," *Journal of the Chinese Chemical Society*, vol. 57, pp. 490–495, 2010.

[40] M. K. Ram, N. Sarkar, P. Bertoncello, A. Sarkar, R. Narizzano, and C. Nicolini, "Fabrication and characterization of poly[(2-methoxy-5-(2'-ethylhexyloxy)phenylene vinylene] (MEH-PPV) langmuir-schaefer films and their application as photoelectrochemical cells," *Synthetic Metals*, vol. 122, no. 2, pp. 369–378, 2001.

[41] C. J. Collison, L. J. Rothberg, V. Treemaneekarn, and Y. Li, "Conformational effects on the photophysics of conjugated polymers: a two species model for MEH-PPV spectroscopy and dynamics," *Macromolecules*, vol. 34, no. 7, pp. 2346–2352, 2001.

[42] D. Verma, A. Ranga Rao, and V. Dutta, "Surfactant-free CdTe nanoparticles mixed MEH-PPV hybrid solar cell deposited by spin coating technique," *Solar Energy Materials and Solar Cells*, vol. 93, no. 9, pp. 1482–1487, 2009.

[43] M. Jø rgensen, K. Norrman, and F. C. Krebs, "Stability/degradation of polymer solar cells," *Solar Energy Materials and Solar Cells*, vol. 92, no. 7, pp. 686–714, 2008.

[44] X. Li, J. Gao, L. Xue, and Y. Han, "Porous polymer films with gradient-refractive-index structure for broadband and omnidirectional antireflection coatings," *Advanced Functional Materials*, vol. 20, no. 2, pp. 259–265, 2010.

[45] P. Becher, *Emulsions: Theory and Practice*, 3rd ed. American Chemical Society; Oxford University Press, 2001.

[46] R. C. Tenent, T. M. Barnes, J. D. Bergeson, A. J. Ferguson, B. To, L. M. Gedvilas, M. J. Heben, and J. L. Blackburn, "Ultrasmooth, large-area, high-uniformity, conductive transparent single-walled-carbon-nanotube films for photovoltaics produced by ultrasonic spraying," *Advanced Materials*, vol. 21, no. 31, pp. 3210–3216, 2009.

[47] F. C. Spano, "Modeling disorder in polymer aggregates: The optical spectroscopy of regioregular poly(3-hexylthiophene) thin films," *The Journal of Chemical Physics*, vol. 122, no. 23, pp. 234 701–15, 2005.

[48] T. J. Prosa, M. J. Winokur, J. Moulton, P. Smith, and A. J. Heeger, "X-ray structural studies of poly(3-alkylthiophenes): an example of an inverse comb," *Macromolecules*, vol. 25, no. 17, pp. 4364–4372, 1992.

[49] H. Sirringhaus, P. J. Brown, R. H. Friend, M. M. Nielsen, K. Bechgaard, B. M. W. Langeveld-Voss, A. J. H. Spiering, R. A. J. Janssen, E. W. Meijer,

P. Herwig, and D. M. de Leeuw, "Two-dimensional charge transport in self-organized, high-mobility conjugated polymers," *Nature*, vol. 401, no. 6754, pp. 685–688, 1999.

[50] M. C. Gurau, D. M. Delongchamp, B. M. Vogel, E. K. Lin, D. A. Fischer, S. Sambasivan, and L. J. Richter, "Measuring molecular order in poly(3-alkylthiophene) thin films with polarizing spectroscopies," *Langmuir*, vol. 23, no. 2, pp. 834–842, 2007.

[51] D. Kozub, "Structural characterization of the active layer in organic solar cells," PhD Thesis, 2011.

[52] A. G. Touryanski, V. M. Senkov, S. S. Gizha, L. V. Arapkina, V. A. Chapnin, K. V. Chizh, V. P. Kalinushkin, M. S. Storozhevykh, O. V. Uvarov, and V. A. Yuryev, "Investigation of quantum-dimensional structure parameters by x-ray optical, scanning tunneling and transmission electron microscopy," in *Proc. 21th Int. Symp. "Nanostructures: Physics and Technology"*. Academic University Publishing, Conference Proceedings, pp. 166–167.

[53] M. Wojdyr, "Fityk: a general-purpose peak fitting program," *Journal of Applied Crystallography*, vol. 43, no. 5-1, pp. 1126–1128, 2010.

[54] A. L. Patterson, "The Scherrer formula for x-ray particle size determination," *Physical Review*, vol. 56, no. 10, pp. 978–982, 1939.

[55] L. H. Jimison, "Understanding microstructure and charge transport in semicrystalline polythiophenes," PhD Dissertation, 2011.

[56] D. H. Kim, Y. D. Park, Y. Jang, H. Yang, Y. H. Kim, J. I. Han, D. G. Moon, S. Park, T. Chang, C. Chang, M. Joo, C. Y. Ryu, and K. Cho, "Enhancement of field-effect mobility due to surface-mediated molecular ordering in regioregular polythiophene thin film transistors," *Advanced Functional Materials*, vol. 15, no. 1, pp. 77–82, 2005.

[57] B. L. Anderson and R. L. Anderson, *Fundamentals of semiconductor devices*. Boston: McGraw-Hill Higher Education, 2005.

[58] F. C. Spano and C. Silva, "H- and J-aggregate behavior in polymeric semiconductors," *Annual Review of Physical Chemistry*, vol. 65, no. 1, 2014.

[59] S. T. Turner, P. Pingel, R. Steyrleuthner, E. J. W. Crossland, S. Ludwigs, and D. Neher, "Quantitative analysis of bulk heterojunction films using linear absorption spectroscopy and solar cell performance," *Advanced Functional Materials*, vol. 21, no. 24, pp. 4640–4652, 2011.

[60] D. T. Duong, M. F. Toney, and A. Salleo, "Role of confinement and aggregation in charge transport in semicrystalline polythiophene thin films," *Physical Review B*, vol. 86, no. 20, p. 205205, 2012.

[61] J. Clark, J.-F. Chang, F. C. Spano, R. H. Friend, and C. Silva, "Determining exciton bandwidth and film microstructure in polythiophene films using linear absorption spectroscopy," *Applied Physics Letters*, vol. 94, no. 16, pp. 163 306–3, 2009.

[62] F. C. Spano, "Absorption in regio-regular poly(3-hexyl)thiophene thin films: Fermi resonances, interband coupling and disorder," *Chemical Physics*, vol. 325, no. 1, pp. 22–35, 2006.

[63] J. Rivnay, S. C. B. Mannsfeld, C. E. Miller, A. Salleo, and M. F. Toney, "Quantitative determination of organic semiconductor microstructure from the molecular to device scale," *Chemical Reviews*, vol. 112, no. 10, pp. 5488–5519, 2012.

[64] L. Martinu and D. Poitras, "Plasma deposition of optical films and coatings: A review," *Journal of Vacuum Science & Technology A: Vacuum, Surfaces, and Films*, vol. 18, no. 6, pp. 2619–2645, 2000.

[65] G. P. Crawford, *Flexible Flat Panel Displays*. Chichester, UK: John Wiley & Sons, Ltd, 2005.

[66] U. Schulz, U. B. Schallenberg, and N. Kaiser, "Antireflection coating design for plastic optics," *Appl. Opt.*, vol. 41, no. 16, pp. 3107–3110, 2002.

[67] W. Groh and A. Zimmermann, "What is the lowest refractive index of an organic polymer?" *Macromolecules*, vol. 24, no. 25, pp. 6660–6663, 1991.

[68] L. Zimmermann, M. Weibel, W. Caseri, U. W. Suter, and P. Walther, "Polymer nanocomposites with ultralow refractive index," *Polymers for Advanced Technologies*, vol. 4, no. 1, pp. 1–7, 1993.

[69] S. Singaravalu, D. C. Mayo, H. K. Park, K. E. Schriver, and R. F. Haglund, "Anti-reflective polymer-nanocomposite anti coatings fabricated by RIR-MAPLE," *Proc. SPIE 8607, Laser Applications in Microelectronic and Optoelectronic Manufacturing (LAMOM) XVIII*, p. 860718, 2013.

[70] B.-J. Bae, S.-H. Hong, E.-J. Hong, H. Lee, and G.-y. Jung, "Fabrication of moth-eye structure on glass by ultraviolet imprinting process with polymer template," *Japanese Journal of Applied Physics*, vol. 48, no. 1, p. 010207, 2009.

[71] R. D. McCormick, E. D. Cline, A. S. Chadha, W. Zhou, and A. D. Stiff-Roberts, "Tuning the refractive index of blended polymer films by RIR-MAPLE deposition," *Proc. SPIE 8258, Organic Photonic Materials and Devices XIV*, p. 825806, 2012.

[72] P. J. Costanzo and F. L. Beyer, "Thermally driven assembly of nanoparticles in polymer matrices," *Macromolecules*, vol. 40, no. 11, pp. 3996–4001, 2007.

[73] S. N. Magonov, V. Elings, and M. H. Whangbo, "Phase imaging and stiffness in tapping-mode atomic force microscopy," *Surface Science*, vol. 375, no. 23, pp. L385–L391, 1997.

[74] M. Khardani, M. Bouacha, and B. Bessas, "Bruggeman effective medium approach for modelling optical properties of porous silicon: comparison with experiment," *physica status solidi (c)*, vol. 4, no. 6, pp. 1986–1990, 2007.

[75] S. N. Kasarova, N. G. Sultanova, C. D. Ivanov, and I. D. Nikolov, "Analysis of the dispersion of optical plastic materials," *Optical Materials*, vol. 29, no. 11, pp. 1481–1490, 2007.

[76] A. Miller, *Handbook of Optics : Optical Properties of Materials, Nonlinear Optics, Quantum Optics, Volume 4 (3rd Edition)*. New York, NY, USA: McGraw-Hill Professional Publishing, 2009, book section 8, p. 8.14.

[77] R. H. Partridge, "Vacuum-ultraviolet absorption spectrum of polystyrene," *The Journal of Chemical Physics*, vol. 47, no. 10, pp. 4223–4227, 1967.

[78] M. Xiaoyan, Q. L. Jun, R. S. Brock, M. J. Kenneth, Y. Ping, and H. Xin-Hua, "Determination of complex refractive index of polystyrene microspheres from 370 to 1610 nm," *Physics in Medicine and Biology*, vol. 48, no. 24, p. 4165, 2003.

[79] R. F. Souza, M. A. R. C. Alencar, E. C. da Silva, M. R. Meneghetti, and J. M. Hickmann, "Nonlinear optical properties of Au nanoparticles colloidal system: Local and nonlocal responses," *Applied Physics Letters*, vol. 92, no. 20, pp. 201 902–3, 2008.

[80] S. Köber, M. Salvador, and K. Meerholz, "Organic photorefractive materials and applications," *Advanced Materials*, vol. 23, no. 41, pp. 4725–4763, 2011.

[81] M. D. W. Grogan, S. C. Heck, K. M. Hood, S. A. Maier, and T. A. Birks, "Structure of plasmonic aerogel and the breakdown of the effective medium approximation," *Opt. Lett.*, vol. 36, no. 3, pp. 358–360, 2011.

[82] D. D. Smith, L. Sibille, E. Ignont, R. J. Cronise, and D. A. Noever, "Noble metal immersion spectroscopy of silica alcogels and aerogels," *Journal of Porous Materials*, vol. 7, no. 4, pp. 499–508, 2000.

[83] G. Patermarakis and N. Nicolopoulos, "Catalysis over porous anodic alumina film catalysts with different pore surface concentrations," *Journal of Catalysis*, vol. 187, no. 2, pp. 311–320, 1999.

[84] I. A. Paun, V. Ion, A. Moldovan, and M. Dinescu, "MAPLE deposited polymeric blends coatings for controlled drug delivery," *AIP Conference Proceedings*, vol. 1464, no. 1, pp. 547–559, 2012.

[85] B. J. Schwartz, "Conjugated polymer as molecular materials: How chain conformation and film morphology influence energy transfer and interchain interactions," *Annual Review of Physical Chemistry*, vol. 54, no. 1, pp. 141–172, 2003.

[86] R. Sø ndergaard, M. Hsel, D. Angmo, T. T. Larsen-Olsen, and F. C. Krebs, "Roll-to-roll fabrication of polymer solar cells," *Materials Today*, vol. 15, no. 12, pp. 36–49, 2012.

[87] A. P. Caricato, M. Cesaria, G. Gigli, A. Loiudice, A. Luches, M. Martino, V. Resta, A. Rizzo, and A. Taurino, "Poly-(3-hexylthiophene)/[6,6]-phenyl-C_{61}-butyric-acid-methyl-ester bilayer deposition by matrix-assisted pulsed laser evaporation for organic photovoltaic applications," *Applied Physics Letters*, vol. 100, no. 7, pp. 073 306–4, 2012.

[88] J. Nelson, "Polymer:fullerene bulk heterojunction solar cells," *Materials Today*, vol. 14, no. 10, pp. 462–470, 2011.

[89] P. G. Nicholson and F. A. Castro, "Organic photovoltaics: principles and techniques for nanometre scale characterization," *Nanotechnology*, vol. 21, no. 49, p. 492001, 2010.

[90] W.-R. Wu, U. S. Jeng, C.-J. Su, K.-H. Wei, M.-S. Su, M.-Y. Chiu, C.-Y. Chen, W.-B. Su, C.-H. Su, and A.-C. Su, "Competition between fullerene aggregation and poly(3-hexylthiophene) crystallization upon annealing of bulk heterojunction solar cells," *ACS Nano*, vol. 5, no. 8, pp. 6233–6243, 2011.

[91] M. T. Dang, L. Hirsch, and G. Wantz, "P3HT:PCBM, best seller in polymer photovoltaic research," *Advanced Materials*, vol. 23, no. 31, pp. 3597–3602, 2011.

[92] S. Subramanian, G. Clark, K. Ly, and T. Chrastecky, "Energy-filtered transmission electron microscopy (EFTEM) of semiconductor devices," *Electronic Device Failure Analysis*, vol. 13, no. 1, pp. 20–28, 2011.

[93] J. Brandrup, E. H. Immergut, and E. A. Grulke, *Polymer handbook*, 4th ed. New York: Wiley, 1999.

[94] G. W. Heffner and D. S. Pearson, "Molecular characterization of poly(3-hexylthiophene)," *Macromolecules*, vol. 24, no. 23, pp. 6295–6299, 1991.

[95] Keithley, "Making I-V and C-V measurements on solar/photovoltaic cells using the model 4200-SCS semiconductor characterization system," *Keithley Application Note Series #2876*, 2012.

[96] C. M. Hansen, *Hansen solubility parameters : a user's handbook*, 2nd ed. Boca Raton: CRC Press, 2007.

[97] D. W. v. Krevelen and K. t. Nijenhuis, *Properties of polymers : their correlation with chemical structure : their numerical estimation and prediction from additive group contributions*, 4th ed. Amsterdam: Elsevier, 2009.

[98] R. D. McCormick, J. Lenhardt, and A. D. Stiff-Roberts, "Effects of emulsion-based resonant infrared matrix assisted pulsed laser evaporation (RIR-MAPLE) on the molecular weight of polymers," *Polymers*, vol. 4, no. 1, pp. 341–354, 2012.

[99] R. D. McCormick, E. D. Cline, A. S. Chadha, W. Zhou, and A. D. Stiff-Roberts, "Tuning the refractive index of homopolymer blends by controlling nanoscale domain size via RIR-MAPLE deposition," *Macromolecular Chemistry and Physics*, vol. 214, no. 23, pp. 2643–2650, 2013.

[100] R. D. McCormick, "Experimental investigation of linear bubble dynamics in a viscoelastic xanthan gel," Master's Thesis, 2002.

Biography

Ryan Daniel McCormick was born in Omaha, NE in 1976. His career thus far has been a fascinating (to him) ride through many varied fields. He attended the Georgia Institute of Technology where he received a Bachelor of Science degree in Physics in March 1999 after working on semiconductor physics under Dr. Phillip First. He then matriculated at Boston University where he received the Chairs Fellowship award to work under Dr. Ronald Roy in underwater acoustics and earned a Master of Mechanical Engineering degree in January 2002. He then tried his hand at electric space propulsion at Busek Co. by working on micronewton colloid thrusters intended for an experimental NASA project of a formation of satellites attempting to detect gravitational waves. In 2005, he moved to North Carolina where he worked for an early stage start-up business called InnerPulse while his wife attended graduate school. At InnerPulse, he aided a team of doctors and engineers, who were working on a new form-factor cardiac defibrillator, by designing and building implant and extraction devices for the intended outpatient procedure, while also getting a taste for transferring new technologies to a commercial business. He then came full circle by again working on semiconductor physics under Dr. Adrienne Stiff-Roberts at Duke University in 2009, this time in the organic realm. Ryan has four peer-reviewed publications [20, 98–100] (of which three are first author [98–100]), two conference proceedings papers [24, 71], and numerous conference presentations.